Clinical Translation of Nanomaterials for Early Detection of Genetic Abnormalities in Fetus and Retinopathy in Neonates and Adults

A Dissertation Presented to the Faculty of the Graduate School at the University of Missouri, Columbia

In Partial fulfillment of the Requirements for the Degree of Doctor of Philosophy

By

SHREYA GHOSHDASTIDAR

Advisor: Dr. Raghuraman Kannan

Department of Biological Engineering

December, 2017

The undersigned, appointed by the Dean of the Graduate School, have examined the dissertation entitled

Clinical Translation of Nanomaterials for Early Detection of Genetic Abnormalities in Fetus and Retinopathy in Neonates and Adults

Presented by Shreya Ghoshdastidar

A candidate for the Degree of Doctor of Philosophy

And hereby certify that in their opinion it is worthy of acceptance

Dr. Raghuraman Kannan,

Department of Bioengineering

Dr. Liqun Gu,

Department of Bioengineering

Dr. Sheila Grant,

Department of Bioengineering

Dr. Anandhi Upendran,

Department of Medical Pharmacology and Physiology

MU-Institute for Clinical and Translational Science

DEDICATION

This work is dedicated to my parents who have supported me through thick and thin and always encouraged me to follow my dreams.

I specially dedicate this work to my grandparents who have been an immense source of inspiration in my life

This work is also dedicated this work to all the teachers in my life including my parents who have imparted knowledge in various ways which I will cherish throughout my life.

ACKNOWLEDGMENTS

First and foremost, I would like to thank my advisor Dr. Raghuraman Kannan for giving me the opportunity to pursue my PhD degree under his guidance. Through his wisdom and experience, I was able to navigate the world of academia and come across the various interesting areas and problems in the field of Nanomaterial diagnostics and therapy. He gave me the freedom to explore and come up with new ideas and pursue them. His insights into the experimental and scientific studies was very helpful in steering the projects in the right direction. He corrected any scientific errors that I would make and gave very constructive critiques about conducting experiments and presenting data. I am grateful to him for being so patient with me during the entire term of my PhD. I have learnt a lot from him and hope to uphold these values in my career.

I am very thankful to my committee members Dr. Andrew Liqun Gu, Dr. Sheila Grant and Dr. Anandhi Upendran for their valuable suggestions and advice during my PhD. Dr. Anandhi's advice was very helpful to plan the experiments for optimization of experiments and for analyzing the clinical samples. She was always ready to help and give suggestions any time I was stuck with any experiment.

The clinical study based projects would not have been possible without the collaboration of the Physicians Dr. Danny Schust, Dr. Dean Hainsworth and Dr. John Pardolas. I would like to thank Dr. Schust for his help with clinical samples and his input and insight regarding conducting the experiments. The regular meetings with Dr. Schust and Dr. Hainsworth were very helpful. Special thanks to all the collaborators and organizations (Ms. Jennifer Schnabel, Dr. Dianne McConnell and PTC Laboratories) that helped us get results and data for our clinical studies.

I would be remiss if I did not mention the immense support of all my Lab members without whose help I would not have been able to come this far. Dr. Ajit Zambre and Dr. Nripen Chanda have been instrumental in training me initially when I first joined this lab. Dr. Zambre has always answered all my questions and doubts with a lot of patience. His help and time and attention to details is highly appreciated. Dr. Dhananjay Suresh and Dr. Abilash Gangula have been very valuable collaborators for my projects. Their extremely methodical way of working, their diverse background and knowledge has been very helpful. Thank you so much for your suggestions and your time. I would like to thank my colleagues Sairam Yadavilli, Brian Jenkins, Dr. Soumavo Mukherjee, Sandhya Saranathan and Nathan Applegren for their valuable discussions and help. I would also like to thank all the undergraduate and high school students Jagjot Kainth, Kacey Ellwein, Ashwath Elangovan, and Premkumar Keerthivaas for helping me out with my projects. Working in the lab was very enjoyable because of the lab members. Thank you all for the all the interesting discussions we had as a group. Thank you to Kristina Conrad and Beth Mayhew for their help in all the administrative affairs and for helping us with ordering all our lab supplies and chemicals without which the experiments would not have been completed.

I am grateful to University of Missouri, Columbia for giving me the opportunity to pursue my graduate studies in this esteemed University. I would like to thank Dr. Shubhra Gangopadhyay and Dr. Shramik Sengupta for giving me the opportunity to come to University of Missouri. I am very grateful to Dr. Amitabha Ghosh and Dr. Shantanu Bhattacharya for introducing me and providing me with the initial impetus to come to University of Missouri. Their mentorship is much appreciated.

To all my friends and roommates in Columbia, thank you for making Columbia home away from home and for always having my back. Sachidevi Puttaswamy and Sagar Gupta, thank you so much for all your help and support throughout all these years and for being such great friends and mentors.

Last but not the least I would like to thank my family for being so supportive in all my decisions and tribulations. Their constant encouragement and optimism has helped me steer through the challenging times and work hard towards achieving my goals. A very special thanks to my mother for teaching me to be strong, optimistic and kind, no matter the circumstances and for being such a great example for me.

Finally, thank you to YouTube and social network sites for all the distractions that were in hindsight helpful in keeping me on track!

TABLE OF CONTENTS

List of Figures

Appendix

List of Abbreviations

1. Au@Fe : Gold coated Iron oxide nanoparticles
2. Fe NC: Iron oxide Nanocubes
3. HD Radius: Hydrodynamic Radius
4. PCR: Polymeric Chain Reaction
5. IHC: Immunohistochemistry
6. Ab Antibody
7. HCG Human Chorionic Gonadotropin
8. HLAG Human Leukocyte Antigen-G
9. CK7 Cytokeratin 7
10. DR Diabetic Retinopathy
11. 8-OHdG 8 hydroxy 2 deoxy guanosine
12. AuNP Gold Nanoparticle
13. ELISA Enzyme Linked Immunosorbent assay
14. LFIA Lateral Flow Immunoassay
15. AuNC Fluorescent gold nanoclusters
16. TEM Transmission Electron Microscopy
17. ROP Retinopathy of Prematurity
18. AGE Advanced Glycation End products
19. ROS Reactive oxygen species
20. PCR Polymerase Chain Reaction

21. NGS Next Generation Sequecing

22. Mtx Methotrexate

23. HSA Human Serum Albumin

24. NMR Nuclear Magnetic Resonance

25. MRI Magnetic Resonance Imaging

26. SERS Surface Enhanced Raman Scattering

CHAPTER 1
MAGNETIC NANOMATERIALS FOR PRENATAL DIAGNOSIS

1.1 Introduction

1.1.1 Prenatal Diagnosis:

Prenatal Diagnosis is an important procedure that provides pivotal information on the genetic health and other abnormalities of fetus. The prenatal diagnostic procedures help clinicians and parents to strategize health management and treatment options after birth (Bolnick et al, 2014). Prenatal diagnosis helps the parents by giving them adequate time to mentally and emotionally cope with the health condition of the baby and also allows them to plan and manage the remaining weeks of pregnancy. Currently, prenatal diagnosis is mostly limited to high risk pregnancies. High risk pregnancies entail potential risk factors like maternal age (greater than 35 or under 17), medical conditions that exist before pregnancy (High blood pressure, Diabetes, Genetic diseases) or medical conditions that develop during pregnancy (Preeclampsia, Gestational Diabetes) (Shajpal et al, 2017). Amniocentesis and Chorionic Villus Sampling (CVS) are two invasive prenatal diagnostic procedures currently used in clinics. Amniocentesis is usually performed in second trimester and involves collection of amniotic fluid from the mother's sac via a syringe, while CVS is performed at end of first trimester to end of second trimester (week 12- 17) and involves removal of tissue sample from the placenta (Figure 1 b)(Mantzaris and Cram, 2015). Albeit having a high sensitivity and accuracy, both these procedures pose considerable risk to the fetus and is conducted at stages of pregnancy where the parents may have limited options. Hence, to fully harness the potential of prenatal diagnosis to our advantage, it is crucial to develop a non-invasive technique, where fetal cells can be obtained

from the mother without posing a risk to fetus. An understanding of prenatal development will provide us insights on fetal cell collection with no risks.

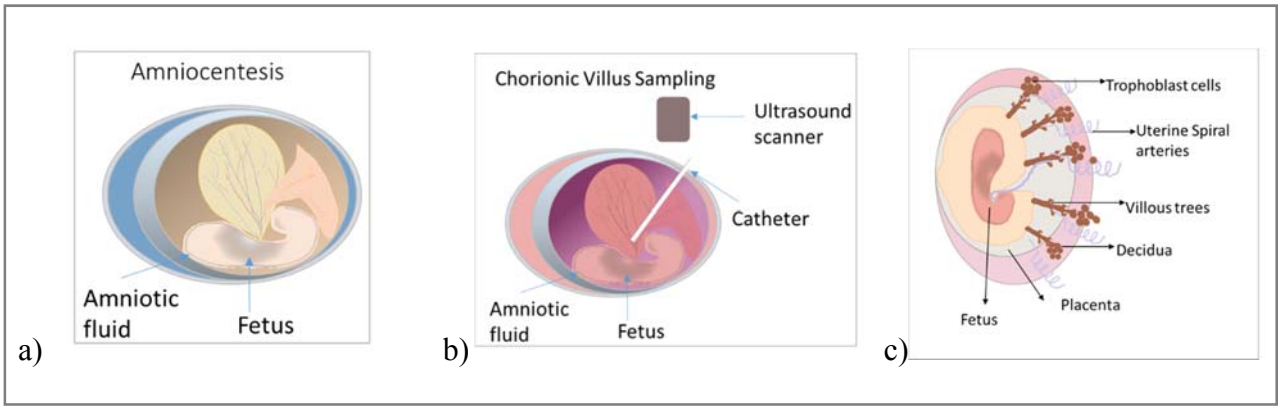

Figure 1: Schematic of a) Amniocentesis and b) Chorionic Villus Sampling c) Placenta and Trophoblast cells interface

1.1.2 Prenatal Development

The development of the fetus starts with the formation of an ovum when a sperm fertilizes with a zygote in the fallopian tube of the uterus. The ovum rapidly divides and grows to a 16-cell morula in the fallopian tube and then to a 32-cell blastocyst which enters the endometrial cavity and eventually implants into the endometrial wall of the mother. The outer cells of the blastocyst differentiate into *trophoblast cells* which form the outer layer of the cell while the inner cell mass develops into an embryo (Red-Horse et al., 2004). The trophoblast cells invade the decidualized endometrium and further divide into two layers called syncytiotrophoblast cells (outer layer) and cytotrophoblast cells (inner layer). Once the embryo is completely implanted in the endometrial wall, the syncytiotrophoblast cells come in contact with maternal blood and initiate the formation of the placenta, which provides the essential nutrients and oxygen to the embryo from the maternal blood circulation. From week 4 of prenatal development, the placenta becomes the primary source of nutritional exchange (Figure 1c). The placenta is connected to the embryo through the umbilical

cord. The maternal portion of the placenta forms the deepest layer of the endometrium. The embryonic portion of the placenta is formed by the syncytiotrophoblast cells and cytotrophoblast cells which proliferate to form the chorionic membrane. The chorionic membrane forms finger like structures that penetrate into the endometrium wall that are called the chorionic villi. The cytotrophoblast cells perforate the chorionic villi and into the endometrium to reorganize the maternal blood vessels and augment the blood supply around the villi. The placentation is complete by weeks 14-16 (Hui, 2012). This is the period when the trophoblast cells are most proliferative and penetrative. Once, the placenta develops into a fully developed organ, it regulates the nutritional, respirational and endocrine functions of the embryo. The excreted products and waste blood from the fetus travel through the umbilical arteries and the maternal nutrients and oxygen travel through the umbilical vein. In the following weeks, the fetus develops the central nervous system and the organogenesis of the embryo is completed.

The prenatal development process highlights that the primary areas of contact between the embryo and the maternal circulation is i) through the invasion of the trophoblast cells in the endometrium wall in the uterus and ii) the transfer (exchange) of nutrients and cells via blood through the placenta and umbilical arteries. Trophoblast cells are shed into the uterine region of the mother during the implantation process and can be recovered either from cervical or vaginal area of the mother (Fritz et al., 2015). The placenta transfers the excretion and other products through the umbilical arteries to the maternal circulation. Hence, traces of cell free fetal DNA can be found in the maternal blood circulation. Trophoblast cells and cell free fetal DNA are sources that can provide critical information on fetus and are currently being explored for developing non-invasive prenatal diagnosis. Trophoblast cells have certain advantages over cell free fetal DNA in that the concentration of cells in uterine region is higher than the amount of cell free fetal DNA in blood.

According to some reports there are approximately 1 trophoblast cells in 2000 mother's cells(Bolnick et al., 2014) while the concentration of cell free fetal DNA is about 1 in 100,000 (Bolnick et al., 2014). In addition, the intact cell can be analyzed by a wide range of techniques including Immunohistochemistry (IHC), Fluorescent in situ Hybridization (FISH), Fluorescence Microscopy, PCR and Genotyping and DNA sequencing. The cost associated with analyzing a whole cell can be adjusted according to the analysis method which makes whole cell analysis a more flexible and cost-effective method of analysis.

1.1.3 Trophoblast cells for Prenatal Testing

Trophoblast cells play a significant role in the fetal implantation into the endometrium wall and hence can be found into the uterine region of the mother (Tarrade et al., 2001). Trophoblast cells have attracted attention from scientists in the past decade because of their invasive nature and their presence in the uterine tissue. Some scientists have reported that trophoblast cells extracted during the early pregnancy harbor important genetic information about the fetus (Mantzaris et al, 2015) It was hypothesized that since extra villous trophoblast cells the uterine tissue, some of the trophoblast cells will shed in to the uterine region of the mother. These trophoblast cells can be sampled from the uterine region (cervix) of the mother and if selectively extracted would provide details about genetic information on fetus. The uterine region comprises of primarily mother's epithelial cells and mucus. The trophoblast cells are sparsely populated in the areas. In order to collect trophoblast cells, they need to be enriched from the mother's cells by using unique surface markers expressed by trophoblast cells.

The Trophoblast cells shed into the uterine region can be collected through the cervical or vaginal region. The trophoblast cells are in a pool of mother's epithelial cells and are sparsely populated. Hence it is crucial to enrich the trophoblast cells from the mother's cells and extract genetic

information from them. There are several reports in literature about the use of trophoblast cells obtained from the cervix for non-invasive prenatal testing that include detection of trisomies 18 and 21, Rh status of fetal status and hemoglobinopathies (Fritz et al, 2015) (Bolnick et al, 2014). Several procedures have been used for isolation of trophoblast cells from the cervical canal and one of them is utilization of monoclonal antibodies that are specific to surface markers overexpressed on trophoblast cells. (A. N. Imudia et al., 2009) (Bolnick et al., 2014; Douglas & King, 1989; Li & Schust, 2015).

1.1.4 Cell Surface markers and monoclonal antibodies for Trophoblast cell isolation:

The most commonly studied surface markers of extra villous cytotrophoblast cells are βHCG (beta human chorionic gonadotropin), HLA-G (Human Leukocyte antigen-G), CK7 (Cytokeratin 7) and HPL (Human Placental lactogen) (Li & Schust, 2015). βHCG and HPL are proteins that are excreted by trophoblast cells to signal the corpus luteum to not dissolve the endometrial wall so that the fetus can implant into the endometrial wall. Extra villous cytotrophoblast cells express less βHCG as compared to syncytiotrophoblast cells. HLA-G is major histocompatibility (MHC) antigen that reacts with maternal Natural Killer cells and inhibits them there by helping the fetal cells to escape the maternal immune surveillance system. (Xiaoming Zhu, Han, Yin, Wang, & Yao, 2011). HLA MHC complex has other isoforms called HLA-A, HLA-B, HLA-C which are not known to be expressed in trophoblast cells. HLA-G molecule may be transmembrane or soluble isoform. The monoclonal antibodies against HLA-G are developed based on the denatured or conformational isoform of HLA-G. The MEM-G9 antibody is made against the conformational dependent and transmembrane isoform of the HLA-G. It does not cross react with HLA-A, HLA-B and HLA-C transfectants. The 4H84 antibody is made against the denatured and soluble isoform of HLA-G. It cross reacts with the HLA-A transfectant (Apps, Gardner, & Moffett, 2008).

Cytokeratin-7 is a protein encoded by keratin gene which is responsible for the transitional nature of the cells. HLAG is a surface receptor protein and is specifically expressed in trophoblast cells, which can be utilized to isolate the trophoblast cells from the epithelial cells (Zhu et al, 2011) (Jain et al., 2016). βHCG and CK7 are primarily used for counterstaining to confirm the isolation of trophoblast cells (Bolnick et al., 2014; Anthony N. Imudia, Kumar, Diamond, DeCherney, & Armant, 2010).

1.1.5 Enrichment of Trophoblast cells for Prenatal Diagnosis: Challenges

The prenatal diagnosis using trophoblast cells is sought with a few challenges, the primary ones being the site of collection, trophoblast cell enrichment and gestational age of the fetus at the time of collection. The current sampling method is focused on collecting cells from cervical canal of the mother using a cytological brush which is like a Pap smear test (Mantzaris, 2015). The cervical canal has a higher mucus content and is also more susceptible to bleeding from cytological brush causing discomfort during sampling. The cells and mucus move into the vaginal area from the cervix which can be collected using a cotton swab. The cervicovaginal mucus is essentially diluted cervical mucus which make collection and separation of cells easier. Vaginal sample collection seldom contain blood and is a relatively easy procedure causing less discomfort and pain in patients. Copan FLOQ™ swabs, made of nylon are optimized to keep the sample closer to the surface for fast and complete elution. They have a higher recovery rate than cotton swabs (http://www.copanusa.com/products/collection-transport/floqswabs-flocked-swabs//i-love-floqswabs). Most of the maternal sample comprises of mucus and the mother's epithelial cells. The trophoblast cells are sparsely populated (1 in 2000) in vaginal and cervical samples (Bolnick et al, 2015). The major challenge in extracting the trophoblast cells is to enrich them by separating them from the maternal contaminants.

Enrichment of trophoblast cells adopted by several groups broadly fall into two categories (1) size based separation and (2) surface receptor based separation. The most commonly used size based separation techniques are gradient centrifugation and fluorescent activated cell sorting (FACS)((Kavanagh, Kersaudy-Kerhoas, Dhariwal, & Desmulliez, 2010). These techniques suffer from certain limitations like clogging, slow separation, low purity, cell loss and damage (Kavanagh et al, 2010). In surface receptor based techniques, cells that expressing specific cell surface antigens (Kavanagh et al, 2010) are targeted using monoclonal antibodies. The trophoblasts cells can be marked by either labelling the antibodies against the cell surface maeker like HLA-G or CK-7 with fluorophores or isolated using nanoparticles (Douglas et al, 88) (Li et al, 2015) (Stenqvist et al,2008).Nanoparticles have high surface to volume ratio leading to higher binding capacity and higher capture efficiency (Wen et al, 2014). In order to obtain genetic information from the DNA or chromosome of the trophoblast cells, it is crucial to isolate and extract intact trophoblast cells. Magnetic nanoparticles have unique magnetic properties, wherein they develop magnetic moment when placed under an external magnetic field and can be used to magnetically separate the cells tagged with the nanoparticles. (Pankhurst, Connolly, Jones, & Dobson, 2003)

1.1.6 Hypothesis and Solution

Our hypothesis is trophoblast cells are present in vaginal region along with maternal epithelial cells and can be selectively enriched from the pool of mother's epithelial cells using magnetic nanoparticles surface conjugated with monoclonal antibodies specific to HLAG. Magnetic nanoparticles have unique properties wherein they develop a magnetic moment when placed under an external magnetic field (Gupta et al, 2005). Magnetic particles tagged with antibodies against specific target can be isolated using external magnetic force.(Xu & Sun, 2009) Monoclonal antibodies are preferred to target specific isotopes of the antigen.(Nelson et al., 2000) Monoclonal antibodies against HLA-G conjugated with magnetic nanoparticles can be used to isolate trophoblast cells

from the vaginal swab. Trophoblast cells invade the decidualized endometrium into maternal uterine region during the first 4 weeks to initiate the formation of placenta. By week 12 the formation of the placenta and the chorionic villi is complete (Hui, 2012). The trophoblast cells are most active and invasive during the first 12 weeks of the pregnancy. Hence these cells can be collected from the uterine region during the first trimester of pregnancy(Ji et al., 2013).Trophoblast cells can be primarily found in the cervical or vaginal region of the mother (Imudia et al, 2010). The cervical region is amenable to bleeding and thicker mucus. The cervicovaginal fluid is diluted cervical mucus (Heng et al., 2015). The vaginal area is less amenable to bleeding and samples can be collected through a Coppan Floq nylon swab. To this effect, we made a magnetic nanoparticle based enrichment platform to isolate trophoblast cells from a vaginal swab sample collected from pregnant women who are in the first trimester of pregnancy.

a) 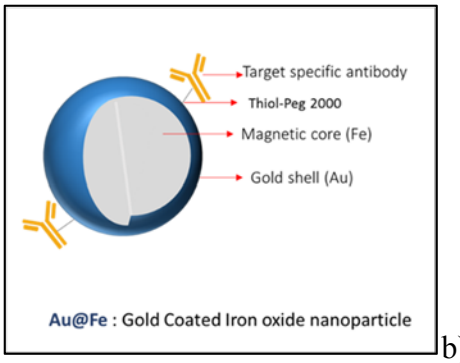

b) 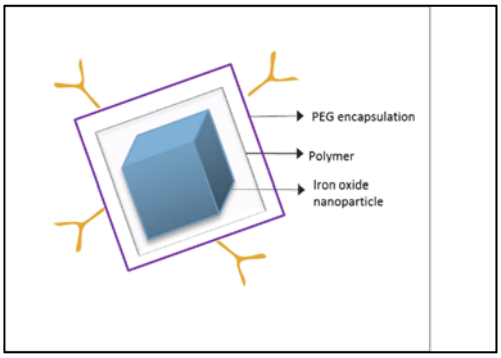

Figure 2: a) Au@Fe nanoparticle b) FeNC

1.1.7 Magnetic Nanoparticles for Trophoblast Isolation and Enrichment:

In the past few decades, nanoparticles have been explored extensively in the medical industry for applications in diagnostic, therapeutic and theranostic fields. Nanoparticles have core diameters

ranging from 10nm- 40 nm which is comparable to the nuclear pore size and are much smaller than a cell (10-100μm) (Frey, Peng, Cheng, & Sun, 2009). Magnetic nanoparticles of a very small size form a single magnetic domain. When they are tagged with a target agent, they can interact specifically with the biomoclules of interest, which makes them easy to manipulate and target (Frey et al, 2009) In most magnetic particles, the external magnetic field (H) and magnetization of particle (B) are related as following:

B=μH, where μ is the magnetic permeability of the particles. In super paramagnetic particles at T_B, the hysteresis loop is very narrow, which implies that a there is very less retention of magnetism once the external magnetic field is removed (Gupta A, 2005). The high saturation magnetization and a low saturation field of the nanoparticles along with no remnant magnetization make it ideal for its application in the biological systems. Super paramagnetic particles have less inter-particle interactions and hence they will not aggregate amongst themselves and can be injected as a ferrofluid or be utilized as a bio sensor for different purposes (Gupta A, 2005). We have developed a library of magnetic nanoparticles and investigated their potential in trophoblast cell extraction. The two groups of nanoparticles synthesized were spherical and cubic magnetic oxide nanoparticles (Figure 2 a, 2 b). The spherical iron oxide nanoparticles were further functionalized by coating with Gold (Figure 2 b). The nanoparticles were conjugated with different antibodies. Our repertoire of magnetic nanoparticles is listed in Table 1.

Nanoparticles	Properties
FeNC- 4H84	Iron oxide nanocubes conjugated with anti-HLAG antibody (4H84)
FeNC-MEMG9	Iron oxide nanocubes conjugated with anti-HLAG antibody (MEM-G9)
FeNC-4H84-MEM G9	Iron oxide nanocubes conjugated with anti-HLAG antibody(4H84 and MEM-G9)
Au@Fe-4H84	Gold coated ironoxide nanospheres conjugated with anti-HLAG antibody(4H84)

Au@Fe-MEM G9	Gold coated Iron oxide nanospheres conjugated with anti-HLAG antibody(MEM-G9)
Au@Fe-4H84-MEM G9	Gold coated Iron oxide nanospheres conjugated with anti-HLAG antibody(4H84 and MEM-G9)

1.1.8 Iron oxide Nanocubes (Fe-NC)

Current technologies used in isolating cells involve the use of large magnetic beads. Limitations of these beads include large size (>100 nm) and tendency to aggregate. Specifically, magnetic beads are ferromagnetic in nature and have inherent magnetic properties and can result in aggregation. These properties lead to low specificity and magnetic capture ability. To overcome this limitation, we designed 20 nm magnetic nanocubes with greater magnetic moment and paramagnetic properties compared to the magnetic beads. Therefore, these nanoparticles do not contain residual magnetization in absence of an externally applied magnetic field for capturing them. As they are devoid of inherent magnetization, these particles do not agglomerate and achieve high solvent stability. Additionally, the cubic shape has larger surface to volume ratio, and higher force of attraction per given angle as compared to spherical beads. Iron oxide nanocubes have been reported to have high magnetic moment which leads to faster separation kinetics (Zhen et al., 2011).

1.1.9 Gold Coated Iron Oxide Nanoparticles

Multifunctional nanoparticles exhibit diverse optical, catalytic, magnetic and physical properties. Metal coated iron oxide nanoparticles which have the advantage of getting less aggregated and can introduce different functional groups on the surface. Gold conjugated Iron oxide nanoparticles (Au@Fe) have unique surface chemistry that enables the nanoparticles to be functionalized easily and excellent optical properties due to the gold coating (Pariti et al, 2014). The iron oxide core provides the Au@Fe nanoparticles with superparamagnetic properties (Pariti et al, 2014). Gold

coated iron oxide nanoparticles offer several advantages. They offer size controllability and can be easily manipulated by an external magnetic field due to their magnetic properties hence making them very good tools for target selectivity for diagnostics and targeted drug delivery for therapeutics. Due to the high surface to volume ratio of the nanoparticles, they have increased affinity towards biomolecules and are highly efficient tools for isolating target molecules from a pool of nonspecific cells. These properties of the Au@Fe nanoparticles have been utilized in the project for selective isolation of trophoblast cells from swab samples collected from the mother's uterine region.

1.2 Materials and Methods

1.2.1 Materials

Iron (III) acetylacetonate, Ironn(III) chloride, oleic acid,N-(3-Dimethylaminopropyl)-N′-ethylcarbodiimide hydrochloride (EDC), N-Hydroxysulfosuccinimide sodium salt (sulfo-NHS), 2-(N-morpholino)ethanesulfonic acid (MES), bovine serum albumin, MS-SAFE Protease and Phosphatase Inhibitor, triton X-100, tween-20 and phosphate buffer saline were purchased from Sigma-Aldrich. Hexane, toulene and chloroform were purchased from Acros organics. Sodium hydroxide (NaOH), acetone, sucrose, sodium borate buffer, Hoechst dye, Cell mask deep red membrane dye, Pierce ECL Western Blotting Substrate, Pierce BCA Protein Assay Kit and TMB were purchased from Thermo-Fisher Scientific. B-Actin, both anti-mouse and anti-rabbit secondary HRP-linked IgG antibody were purchased from Cell Signaling. Anti-HLAG antibody (4H84) was purchased from BD Biosciences. Anti-HLAG antibody (MEM G9), Anti-βHCG antibody was purchased from abCAM. Carboxymethyl-polyethyleneglycol-thiol was custom synthesized from Nanocs and Laysan Bio. 10x TBS, 10x

Tris/Glycine/SDS buffer, 4-15% 10-well 50 µl ready Mini-Protean TGX, Precision Plus Protein Dual color standard ladder and supported nitrocellulose Membrane (0.2 µm) were purchased from Biorad. Recombinant Human EGF (carrier-free) and Alexa Fluor 647 *anti*-Cytokeratin PAN antibody were purchased from BioLegend. Amicon 0.5 ml 100Kd Regenerated cellulose Ultracel centrifugal filter units were purchased from Merck Millipore Ltd.

1.2.2 Instrumentation

Core nanoparticle size measurements were performed using Joel TEM. Hydrodynamic size and zeta potential was measured using a Malvern Zetasaizer Nano-ZS. Centrifugation was performed on a 5424 Eppendorf and refrigerated RC 6+ Sorvall centrifuge. pH was measured using a Seven Compact Mettler Toledo pH meter equipped with an InLab Micro electrode. Fluorescence imaging, fluorescence assays and UV-vis absorption assays were performed on a Cytation 5 Cell imaging multi-mode reader. Gel electrophoresis was performed on a Biorad Mini-Protean Tetra system and blots were transferred using a Genscript e-blot transfer system. Western blot imaging and acquisition was performed using Image Lab ver 5.2.1 software on a ChemiDoc XRS system from Biorad. Band densitometry analysis was performed on Image Studio ver 5.2. Solvent extraction was performed on a Büchi Rotovapor R-124 attached to a water bath and watercoo led distillation column. SQUID measurements were performed on a Quantum Design MPMS 3 Magnetometer.

1.2.3 Synthesis of Iron oxide nanocubes (FeNC)

The synthesis was carried out under an argon atmosphere using standard Schlenk line techniques. In a typical synthesis of magnetite nanocubes (79nm), iron acetylacetonate (7.06g, 20mmol) was

added to a mixture of oleic acid (1.129g, 12.689ml) and benzyl ether (104g, 99.71ml) (Zhen et al,2011). The mixture was degassed under argon at room temperature for 30 minutes. The solution was then heated to 290ºC at the rate of 20ºC/min with vigorous magnetic stirring. The reaction mixture was maintained at this temperature under argon atmosphere for 30 minutes. After cooling the solution to room temperature, a mixture of toluene (40ml) and hexane (10ml) was added to the solution. The solution was then centrifuged at 10,000g for 20 minutes to precipitate the magnetic nanocubes. The separated precipitate was washed again with hexane and toluene till a clear supernatant was obtained. The final pellet was dissolved in hexane. Iron nanocubes synthesized using polyol process resulted in formation of hydrophobic particles soluble only in organic phase. In order to convert them to hydrophilic particles for use in aqueous and physiological solutions, we replaced the organic coating with a functional amphiphilic polymer by modifying a previously published protocol(Teng & Yang, 2004).

Briefly, synthesized FeNCs (in hexane) were injected into a rapidly stirring (500 RPM) Poly (maleic anhydride-alt-1-octadecene) (1.2 g, mol wt. 30,000-50,000) solution dissolved in chloroform (100 ml) in a one neck 200 ml round bottom flask. After 2 h of stirring, solvent was removed using a rotary evaporator (100 RPM, 55 °C) attached to standard vacuum line protected by a liquid nitrogen cool trap, until a wet sludge was formed. The sludge was quickly mixed with 50 ml of 0.1 M NaOH solution and dispersed using sonication for 1 h. Solution was then stirred (500 rpm) for 15 h at room temperature to hydrolyze and open the maleic anhydride rings. The opening of these rings adds free carboxylic groups to the ends of the polymer. These groups can be used to functionalize amines on the nanoparticle surface by –COOH activation. The solution was washed 2 times with 0.1 M NaOH solution at 20,000 g (15 °C) for 1 h, followed by 2 times with 3-layer sucrose density gradient centrifugation (30%,

20% and 10% sucrose). Pellet was resuspended and concentrated in 4 ml 10 mM MES buffer and washed once. As a next step 100 kDa centrifugal filters were equilibrated with MES buffer and used for removing excess polymer (6000g for 6 min). Solution was then again subject to 2-layer sucrose density gradient centrifugation (30% and 10% sucrose) at 15000g for 15 min, followed by washes with DI water. FeNC pellet was then redispersed in 5 ml water and stored at room temperature.

1.2.4 Synthesis of Au@Fe nanoparticles

Au@Fe NPs were synthesized using a two-step process. First, iron oxide nanospheres were synthesized by thermal decomposition of iron oleate complex. The second step comprised of reduction of gold (III) ions on iron oxide nanospheres to form Au@Fe nanoparticles. The FeNC NP were synthesized using a polyol synthesis method which involves thermal decomposition of the iron oleate complex to form iron oxide nanoparticles (Zhen et al, 2011). The iron oleate complex was prepared using a previously established method with a few modifications(Park et al., 2004). Briefly, 4.8gm NaOH was dissolved in 50ml DI water to which 80ml Ethanol and 40ml oleic acid was added slowly and the pH was adjusted to 7. 10.8gm $FeCl_3$ was dissolved in 10ml DI water and added to the oleic acid solution along with 140ml hexane. The solution was heated to 60^{o}C and maintained at the temperature for 4 hours. The upper organic layer containing the iron oleate complex was washed with 30ml DI water three times. The excess hexane was removed with rotary vacuum evaporator at 65^{o}C for one hour resulting in a dark red waxy solid iron oleate complex. Spherical iron oxide nanoparticles were synthesized by adding 7.2gm iron oleate complex to 50.69ml 1 octadecene and 1.28 ml oleic acid. The iron oleate mixture was deoxygenated under nitrogen atmosphere for 20 minutes. The solution was heated to 300^{o}C at a heating rate of 5^{o}C/min and maintained at the temperature for 30 minutes after which the heating

source was removed and the solution was allowed to cool to room temperature. The resulting dark brown solution was precipitated using 100ml acetone. The precipitated particles were washed with hexane and acetone three time at 15000g for 30 minutes. The final pellet was dissolved in 5ml Chloroform. The Au@Fe nanoparticles were synthesized by a previously established procedure with significant modifications (Robinson, Tung le, Maenosono, Walti, & Thanh, 2010). Iron oxide nanoparticles (0.9gm) were dissolved in 10ml octadecene and 1.3 gm 1, 2 hexadecanediol. The solution was heated to 100^{o}C for 1 hour and subsequently heated to 140^{o}C to which gold oleylamine complex was added. The complex was prepared by sonicating $HAuCl_4$ in 5ml octadecene and 1 ml oleylamine. The iron oxide solution with the gold complex was heated at 140^{o}C for 15 minutes followed by heating to 200^{o}C. The solution was maintained at the temperature for 20 minutes and then removed from heat to be cooled to room temperature. The nanoparticles thus formed were hydrophobic particles soluble only in organic phase. In order to convert them to hydrophilic particles for use in aqueous and physiological solutions, we replaced the organic coating with a functional amphiphilic polymer by modifying a previously published protocol(Robinson et al., 2010).

1.2.5 Antibody conjugation to Au@Fe and FeNC particles

The polymer coated iron oxide nanocubes were covalently conjugated to antibody (anti-HLAG) via standard EDC/NHS activation chemistry (Zhang et al., 2014) (Nakajima & Ikada, 1995). We followed manufacturer's protocol for the EDC and NHS activation. Briefly, 100µl(mg/ml) of PMA coated FeNCs and PEG coated Au@Fe nanoparticles were washed with MES buffer prior to being activated with 3mg EDC and 4mg NHS in 400µl MES buffer at 28^{o}C for 3.5 hours. The activated particles were centrifuged at 15,000g for 12 minutes. The supernatant was discarded and the activated FeNC and Au@Fe pellet was dissolved in 20µl Anti-HLAG (4H84) antibody (0.5mg/ml)

and 200 µl 1X PBS and incubated overnight at in a thermomixer at 24ºC and 750 rpm. The antibody conjugated particles were centrifuged at 15,000g for 12 minutes and re-suspended in 1ml 1X PBS. The particles were stored in 4ºC. Similar procedure was repeated for conjugation of Au@Fe and Fe NC nanoparticles with 10µl anti- HLAG (MEM G9) antibody (1mg/ml) and 200µl 1X PBS. For the conjugation of both anti-HLAG (4H84 and MEM G9) epitopes, the activated Au@Fe and FeNC nanoparticles were dissolved in 20µl anti-HLAG (4H84) and 10µl anti-HLAG (MEM G9) and 200µl 1X PBS and incubated overnight at 24ºC in a thermoshaker. The Au@Fe and FeNC nanoparticles were conjugated with the secondary antibodies anti-Mouse IgG and anti-Human IgG using similar process as described above. The activated Au@Fe and FeNC nanoparticles were dissolved in 20µl anti-Mouse IgG (3mg/ml) and 60µl anti-Human IgG (1mg/ml) and 200µl 1X PBS.

1.2.6 Target binding Affinity by ELISA

The conjugation of the antibody to the nanoparticle was confirmed utilizing a surrogate antigen (Globin), and anti-Globin antibody as the surrogate antibody. Briefly, 100µl of Globin solution at different concentrations (100µg/ml, 10µg/ml, 1µg/ml, 0.1µg/ml, 0.01µg/ml and 0.001µg/ml) was added to each well of a 96 well plate and incubated overnight at 4ºC. The wells were washed with wash buffer (0.5% Tween20) followed by blocking with 200µl 2% BSA solution for 30 minutes at Room temperature. The wells were washed with wash buffer prior to addition of 100µl antibody conjugated nanoparticles. Nanoparticles without antibody were used as a negative control while antibody solution was used as a positive control. In all the experiments PBS was considered as the blank. The nanoparticles were incubated for 2 hours at 37ºC followed by washing the wells once with wash buffer. 50µl of 0.32µg/ml Secondary antibody (goat anti Rabbit IgG) conjugated with Horse-radish Peroxidase (HRP) was added to the wells and incubated for 30 minutes at 37ºC

followed by washing the wells twice with wash buffer. Finally, 50µl of the substrate (TMB peroxidase) was added to the wells and the reaction was stopped by adding 0.1M HCl solution. The plates were read by a Cytation plate reader at absorbance of 450nm.

1.2.18 Cell Studies

Jeg 3 cells were obtained from ATCC. SKBr3 cells, obtained from ATCC were used as negative control. All the cells were cultured in RPMI-1640 medium (ATCC, modified with 4500mg/ml Glucose) with 1% Fetal Bovine Serum (Atlanta Biological, Sigma Aldrich) and 700ul Gentamycin. Cells were grown in a CO_2 incubator (Thermo Fisher) with 5% CO_2 and 37^oC.

1.2.8Clinical Samples

Trophoblast cells were isolated from discarded placental tissues after obtaining consent, non-pregnant women vaginal swab samples collected from healthy volunteers, vaginal swab samples and cheek swab samples from pregnant women during the first trimester of pregnancy were used for the study. The study was approved by University of Missouri, Columbia (IRB no. 2002862) review board. A total of 16 placenta of a male fetus was obtained. Trophoblast cells were extracted by enzyme digestion of the placental tissue followed by Percol density gradient centrifugation ((Li & Schust, 2015). The trophoblast cells were stored in DMEM media at 4^oC.

A total of 45 vaginal swab samples were collected from pregnant women with gestation age ranging from 5 to 12 weeks. Vaginal swab samples from both pregnant and non-pregnant women were obtained using FLOq Coppan™ swabs. The swabs were stored in DMEM medium in 4^oC.

Swab samples collected from pregnant women were stored in DMEM media and cells were extracted by centrifuging at 2000rpm for 10 minutes at RT. The centrifugation was repeated till a

noticeable cell pellet was formed. The cell pellet was then washed with serum free media three times to remove mucous and used for trophoblast enrichment studies.

1.2.19 Western Blot analysis of HLA-G expression:

Trophoblast cells harvested from human placental tissues and Jeg3 cells (10^6 cells/ml) were seeded in a 6 well plate overnight. Whole cell lysates were prepared using Triton X 100 lysis buffer with MS-Safe protease and phosphatase cocktail inhibitor (Sigma Aldrich) and protein concentration was equalized with Bicinchoninic acid assay (Sigma Aldrich). Proteins were separated by 4-15% native PAGE (Bio-Rad) and were transferred onto nitrocellulose membranes (Gen Script). The membranes were incubated with Primary antibody overnight at 4^{o}C. The primary antibodies used for this experiment are β HCG, anti HLAG (4H84) and anti HLAG (MEM G9). The antibodies were washed and then incubated with secondary anti Mouse IgG HRP or anti rabbit IgG-HRP and incubated for 2 hours at 37^{o}C. The membranes were washed and imaged on Chemidoc Biorad imaging system. Actin protein levels were used as a control for adequacy of equal protein loading. Protein expression levels were analyzed by densitometry analysis.

1.2.20 Flow Cytometry analysis of HLA-G expression

Trophoblast and Jeg3 cells (10^5 cells/ml) were incubated with primary antibodies (anti HLAG 4H84, anti HLAG MEMG9) for 1 hour at RT and washed a few times with staining buffer. The cells were then incubated with anti-Mouse IgG Alexa Fluor 488 for 1 hour at RT. The cells were washed few times with staining buffer and fixed with 4% PFA. The cells were analyzed through FACs caliber for percentage expression of HLAG and MEMG9 in Jeg3 and trophoblast cells.

1.2.21 Magnetic capture Efficiency of MNPs

The magnetic capture efficiency of the Au@Fe and FeNC was determined using a surrogate antigen (globin and antibody (anti-globin). 500ul of globin solution at different concentrations (100µg/ml, 50µg/ml and 25µg/ml) were taken in an Eppendorf tube. 200µl of Au@Fe-anti globin antibody (anti-globin Ab) was added to the solutions and incubated at room temperature (RT) for different time durations (0 hour, 3 hours, 12 hours). Au@Fe-Peg at the same concentration was used as control. Following incubation, the tubes were kept in front of a neodymium (N52) block magnet for 20 minutes. The supernatant was removed and stored. The pellet was dissolved in 500ul 1X PBS and kept in front of magnet for 20 minutes. The supernatant was removed and stored, and the final pellet was dissolved in 500µl 1X PBS. The UV-Vis absorbance spectrum of the supernatants and pellet was recorded using a UV-Vis plate reader in Cytation 3.

1.2.22 **Cell Capture Efficiency of MNPs**

Following the proof of principle studies with surrogate antibody and antigen, we proceeded to conduct magnetic capture experiments by using Au@Fe-HLAG (4H84) and FeNC-HLAG (4H84). Jeg3 cells (10^5cells/ml, 10^4 cells/ml) was stained with membrane staining red dye followed by incubation with Au@Fe-HLAG and FeNC-HLAG for 2 hours at 37^{o}C. Au@Fe-Peg and FeNC-Peg were used as controls. Following incubation with magnetic nanoparticles, the solution were kept in front of a neodymium block magnet for 20 minutes. The supernatant was removed and 1X PBS was added to the cell pellet. The magnetic washing was repeated two times. The cells were finally suspended in 200 µl serum free media and imaged under the fluorescence with Cytation 5 and were analyzed with Cytation 5 cell analysis software.

1.2.23 **Cell Capture Specificity of MNP**

The specificity of the cells was determined by capturing target cells (Jeg3 cells) from a mix of Jeg3 and SkBr3 cells. Epithelial cells extracted from vaginal swab of non-pregnant women was used as a negative control. The Jeg 3 cells were stained with red membrane dye C10446 and the epithelial cells were stained with nucleus staining dye Hoechst 3342. Jeg3 cells of varied concentration were (10,100, 1000 cells/ml) were mixed with SkBr3 or epithelial cells (100,000, 10,000 cells/ml) and incubated with antibody conjugated magnetic particles (Au@Fe-HLAG, FeNC-HLAG) for 2 hours at 37ºC**.** Following incubation, the cell solution was kept in front of a NeodymiumN 52 block magnet for 20 minutes. The magnetic nanoparticles formed a pellet near the magnet. The supernatant was removed and the pellet was dissolved in 200ul 1X PBS. Magnetic separation was repeated twice and the pellet obtained was dissolved in 1X PBS and transferred to a 96 well plate. The plate was analyzed with Microplate reader (Cytation 3). The cells were counted using cytation analysis software.

1.2.24 Cell Capture Selectivity for Trophoblast cells

For the clinical samples, the efficiency of the magnetic nanoparticles in capturing trophoblast cells was confirmed using two different methods. The first one was based on direct conjugation, where anti-HLA-G antibody was conjugated with the magnetic nanoparticles and were incubated with the cells followed by magnetic separation. The second method was the HLA-G saturation method, where the magnetic nanoparticles were conjugated with a secondary IgG antibody. The cells were incubated and saturated with anti HLA-G antibody at 37ºC for two hours followed by incubation with Au@Fe-IgG or Fe-IgG nanoparticles at 37ºC for 2 hours. The cells were then magnetically separated and washed and analyzed using Fluorescence imaging and lysed to extract DNA for sequencing and analysis studies.

Direct Incubation Method: Trophoblast cells were mixed with epithelial cells obtained from non-pregnant women vaginal swab samples. s in different ratios (1: 1000 (0.01%) and 1:100 (0.1%)). 10, 100 cells were mixed with 10^4 epithelial cells and 100, 1000 cells were mixed with 10^5 cells/ml epithelial cells. The trophoblast cells were stained with membrane staining C10446 dye (red) while the epithelial cells from non-pregnant women were stained with nucleus staining Hoechst 3342 dye (Blue). The cell mixture was incubated with nanoparticles (Au@Fe and FeNC) conjugated with the HLAG antibody for 2 hours at 37ºC followed by magnetic separation two times. The pellet was dissolved in DIW and transferred to a 96 well plate for imaging and analysis with Cytation 5 plate reader.

HLA-G Saturation Method: The cell capture experiment was repeated with HLA-G saturation method. Briefly, pre-stained trophoblast (C10446) and non-pregnant swab cells (Hoechst 3342) were mixed together in different ratios. The cell suspension was incubated with 20µl anti-HLAG (4H84) antibody (0.5 mg/ml) and 10µl anti-HLAG (MEM G9) antibody (1 mg/ml) at 37ºC for 2 hours. The cells were then incubated with 200ul Au@Fe-IgG or Fe-IgG nanoparticles at 37ºC for 2 hours. The cells were then placed in front of a magnet for 30 minutes and the supernatant was removed. The pellet was dissolved in Serum free media and the magnetic washing step was repeated 3 more times. The cells were then transferred to a 96 well plate and imaged and analyzed using Cytation 5 microplate reader

1.2.25 DNA Analysis

DNA was extracted from the isolated trophoblast cells using ethanol precipitation and resolubilization. DNA obtained was quantified by Qiagen Investigator Kit using RT PCR. Briefly, 1ng of template DNA was amplified using Promega PowerPlex Fusion kit and the

fragments are visualized using capillary electrophoresis on 3130 XL for STR analysis. Gene Mapper ID was used for data analysis (PTC Laboratories, Columbia)

1.2.26 Cell capture with swab cells from pregnant women

The cells isolated from pregnant women were used for trophoblast enrichment by both direct incubation and HLAG saturation procedures as described in detail in section 1.2.14. The isolated cells were stained with DAPI nucleus staining dye followed by counter staining with β HCG conjugated dye. The cells were imaged and analyzed using Cytation 5. Cells were also analyzed using HLA-G saturation method. Cells were extracted from the swab samples by centrifuging at 2000g for 7 minutes three times. For fluorescence imaging and trophoblast cell confirmation by βHCG staining, the cells were incubated with β HCG-Cy5 for 1 hour at 37ºC. 10µg anti-HLA-G (4H84) and 10µg anti-HLA-G (MEM-G9) was added and incubated at 37ºC for 2 hours followed by incubation with 250µl of AF-IgG or 150µl Fe-IgG at 37ºC for 2 hours. The cells were magnetically separated and washed four times. The cells were then transferred to a 96 well plate and they were imaged using Cytation 5 microscope.

1.2.27 Immunohistochemistry staining with CK 7

To confirm whether the cells extracted by magnetic nanoparticles were trophoblast cells, the cells were coated on a microscope slide by cytospin and stained with anti-CK 7 antibody and imaged under the microscope. 150µl of the Cells solution (12,000cells/ml) were spun at 700 rpm for 5 minutes onto positive charged slides and air dried for 2 hours to overnight. The slides were then fixed in formalin (10% NBF) for 10-20 minutes and rinsed in water. Slides were treated with Dako Target retrieval solution Citrate buffer and heated at 95ºC for 20 minutes in a steamer followed by cooling to RT for 20 minute sand rinsing with DIW and incubated with 1X PBS for 5 minutes.

The step was repeated twice. Blocking was done by Normal Horse Serum. The cells were incubated with anti-Cytokeratin 7 (Oy-TL 12/30) mouse monoclonal antibody (Cell Marque, 307M-95, 25µg/ml) with 1:200 dilution in Ventana antibody diluent. The slides were then incubated in MOM ImmPRESS Reagent (Anti mouse IgG polymer reagent peroxidase) for 30 minutes and then washed two times in buffer. The chromagen peroxidase substrate was then added to the cells dropwise and the sections were washed in deionized water. Counterstaining was done by adding Hemotoxylin staining solution and incubating for 1 minute followed by rinsing with water. The cell slides were then dipped in 95% alcohol, 100% alcohol and xylene 10 times and were allowed to harden overnight. The slides were imaged under the Leica Microscope and were analyzed by a Pathologist.

1.3 Results and Discussion

1.3.1 Synthesis and Characterization of FeNC and Au@Fe Nanoparticles

Iron oxide nanocubes (Fe NC) and Gold conjugated iron oxide nanospheres (Au@Fe) were synthesized by thermal decomposition of iron acetylacetonate and iron oleate complex respectively (Park et al., 2004) (Robinson et al,2010) (Clara et al,2012)(Figure 3).

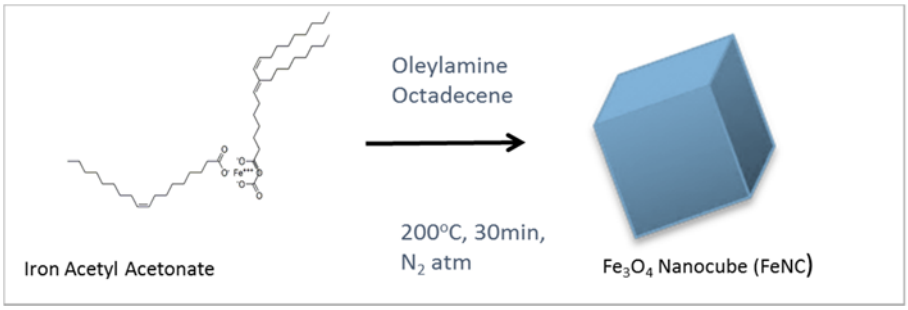

Figure 3 Schematic of synthesis of Iron oxide nanocubes (FeNC)

oIron oxide nanospheres were coated with gold layer to form a core shell structure using oleic acid and oleylamine (Robinson et al) (Figure 4).

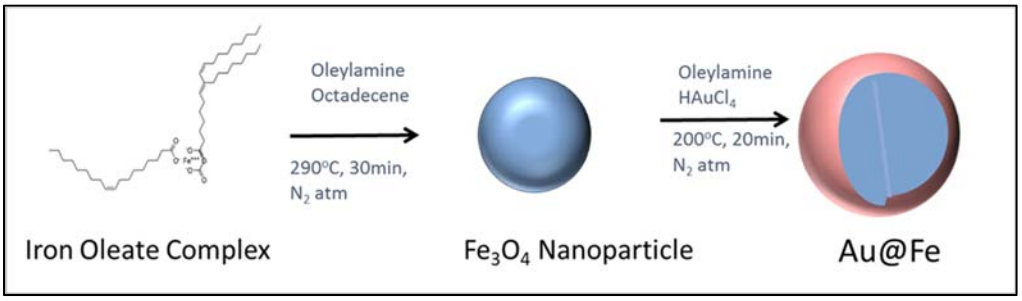

Figure 4 Schematic of synthesis of Gold coated Iron oxide nanoparticles (Au@Fe)

The resulting hydrophilic Au@Fe and FeNC particles had a hydrodynamic size of 156nm, 200nm and Zeta potential of -20 mV and -15mV respectively. TEM images of the iron oxide nanocubes (Figure 5a) and spherical nanoparticle (Figure 5b) confirm that the particles are uniform with a core size of 20nm and core diameter of 30 nm respectively UV-Vis absorbance of 540 nm).

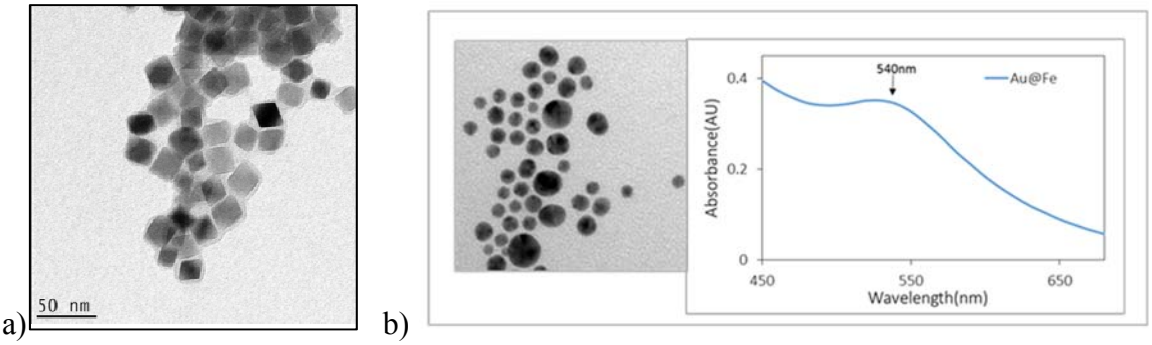

Figure 5: a) TEM Image of Fe Nanocubes b) TEM Image and UV Absorbance of Au@Fe Nanoparticle.

HR TEM images show the distinct lattice structure of the nanoparticles. Energy dispersive X-ray spectroscopy analysis of the Au@Fe nanoparticles demonstrate the presence of both Au and Fe in a single nanoparticle (Figure 6).

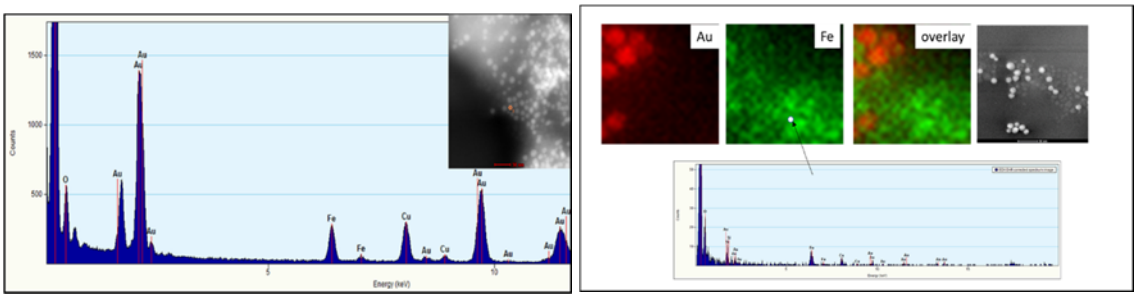

Figure 6: EDS analysis and HR TEM Images of Au@Fe Nanoparticles

The magnetic properties of the nanoparticle were determined by a SQUID Magnetometer. The close hysteresis curve demonstrates that the particles are paramagnetic in nature (Figure 7). The magnetic nanospheres have a near saturation magnetization value of 4.5 emu/g while the magnetic nanocubes have a magnetization of 45 emu/g. The magnetic nanocubes and nanospheres were functionalized using Peg OME and Thiol-Peg-SH respectively to introduce COOH functional groups to the nanoparticles.

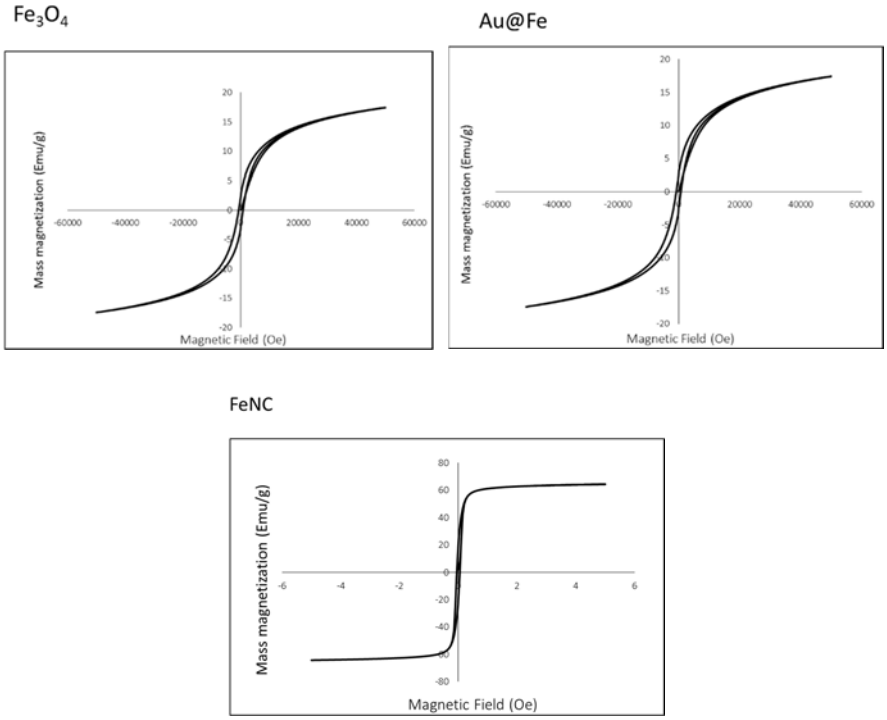

Figure 7: Hysteresis loop of Fe_3O_4 nanospheres, Au@Fe nanoparticles and Fe Nanocubes (FeNC).

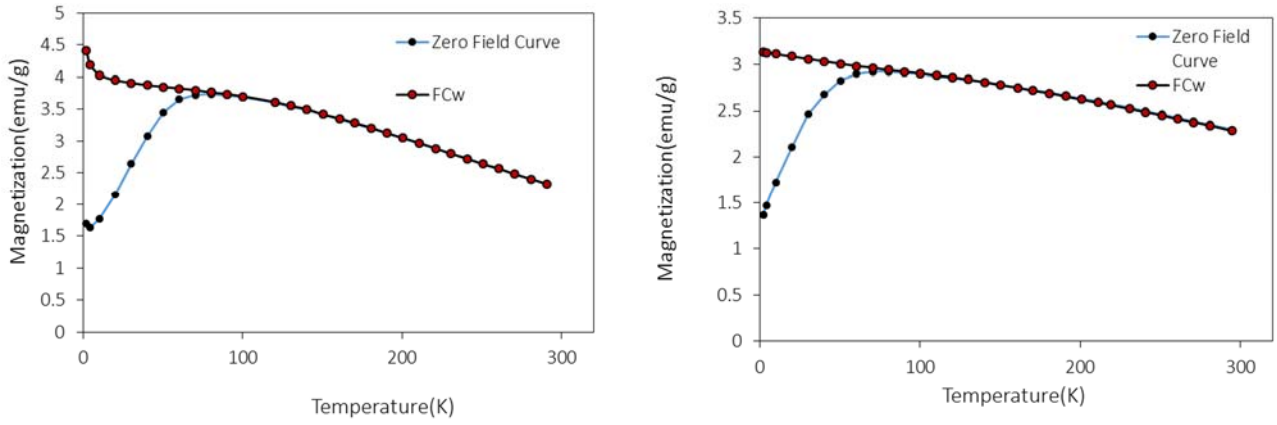

Figure 8: ZFC curves of Fe_3O_4 and Au@Fe Nanoparticles .

1.3.2 Synthesis and Characterization of Au@Fe-Ab and FeNC-Ab nanoparticles:

Anti-HLAG antibody or Anti mouse IgG was covalently conjugated to the nanoparticles. The antibody conjugation was confirmed by comparing the size and zeta potential of the antibody conjugated Au@Fe (Table 2) and FeNC nanoparticles (Table 3) with their precursors. The UV-Vis absorbance of the Au@Fe broadened upon conjugation with antibody(Figure 9). Bradford assay and Micro drop assay was used to determine the antibody conjugation efficiency. Both the methods confirmed conjugation efficiency of 70%.

AuFe

Name of Sample	UV abs	HD Size(nm)	Zeta Potential (mV)
AuFe	550	141	-53
AuFe Peg	550	167.5	30.91
AuFe-Antibody	550	380	-32.8

Table 2: UV absorbance peak, Hydrodynamic size and Zeta Potential of Au@Fe nanoparticles

FeNC

Name of Sample	HD Size(nm)	Zeta Potential (mV)
Fe	148	-63
Fe Peg	142	-5.8
AuFe-Antibody	175	-6.5

Table 3: Hydrodynamic size and Zeta Potential of Fe nanocubes

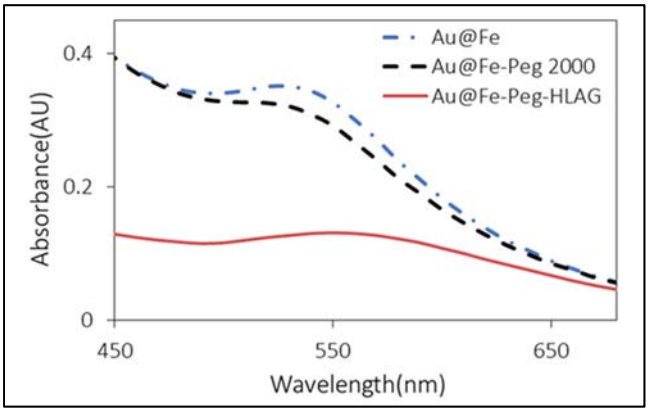

Figure 9: UV-Vis absorbance graph of Au@Fe, Au@Fe-Peg and Au@Fe-Antibody

The ability of antibody conjugated magnetic nanoparticles to capture target antigen was validated using a surrogate antigen and antibody. We chose hemoglobin as our target antigen and anti-globin antibody was the target binding efficiency between the nanoparticle-antibody conjugate and antigen was validated by traditional ELISA procedures. Globin solution at different concentrations was coated on a 96 well plate and then incubated with nanoparticles conjugated with anti-Globin Antibody. Anti-globin antibody was used as a positive control, while Au@Fe-PEG was used a negative control. Physical mixture of Au@Fe-PEG and anti-globin antibody was used as another positive control. The binding efficiency of Au@Fe-Gb was found to be tenfold higher than Au@Fe-PEG and about 1.5 times more than globin antibody itself(Figure 10 a). The binding efficiency of Au@Fe-Ab was almost 1.25 times higher than Au@Fe-PEG and Ab physical mixture at higher concentrations of Globin. From the ELISA graphs, it was established that the detection limit of Globin using Au@Fe-Gb is around 0.100 ng/ml (Figure 10 b). However, the detection efficiency increased with increasing globin concentration 100µg/ml with Au@Fe-Gb.

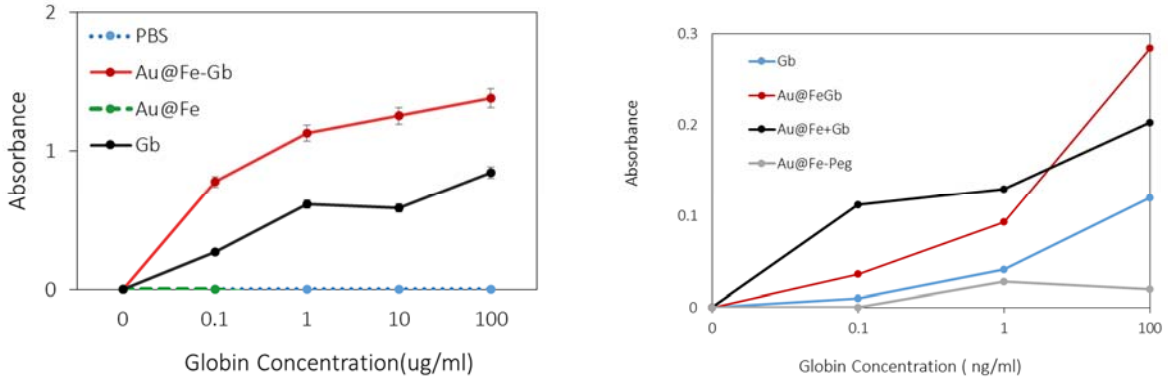

Figure 10: a) Binding affinity of Au@Fe-Gb and Globin at different concentrationsof Globin (µg/ml) compared to control. b) Comparison of binding affinities of Au@Fe-Gb with Au@Fe and GbPhysical mixture at different concentrations (ng/ml)

1.3.3 Target Binding by ELISA

The magnetic capture efficiency of the Au@Fe and Fe nanoparticles was determined using a surrogate antigen and antibody. Au@Fe-anti-globin Ab was incubated with different concentrations of Globin solution followed by magnetic separation (Figure 11) and the time of incubation was optimized by incubating at three different time points. Globin has absorbance peak at 410nm. The UV-Vis absorbance of the pellet and supernatant obtained after magnetic separation was recorded at 410 nm to estimate the amount globin that was bound to the nanoparticle.

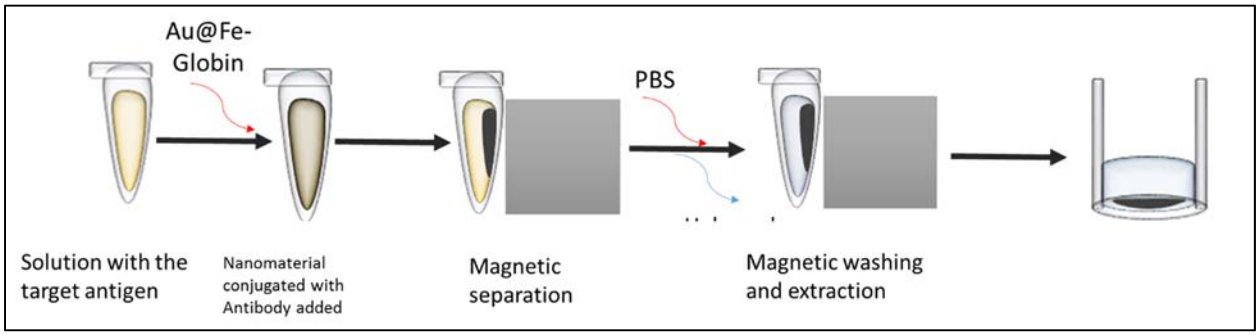

Figure 11: Schematic of the magnetic capture process of Globin using magnetic nanoparticles

Different concentrations of globin (100µg/ml, 50µg/ml and 25µg/ml) were incubated with Au@Fe-anti globin Ab at RT for 3 hours and 12 hours. Au@Fe-Peg was used as control. The absorbance peak corresponding to globin at 410 Were recorded and correlated to capture efficiency. No globin peaks were observed for Au@Fe solution. The amount of globin extracted by the nanoparticles (Au@Fe) was quantified by estimating the amount of globin present in the supernatant (Figure 12). The optimized time for globin capture was calculated to be 3 hours (Figure 13 b). Based on the extracted amount of globin in the pellet the efficiency of Au@Fe-anti globin Ab was estimated as 40-50% for globin solution at a concentration of 25ug/ml and 50ug/ml (Figure 13 a).

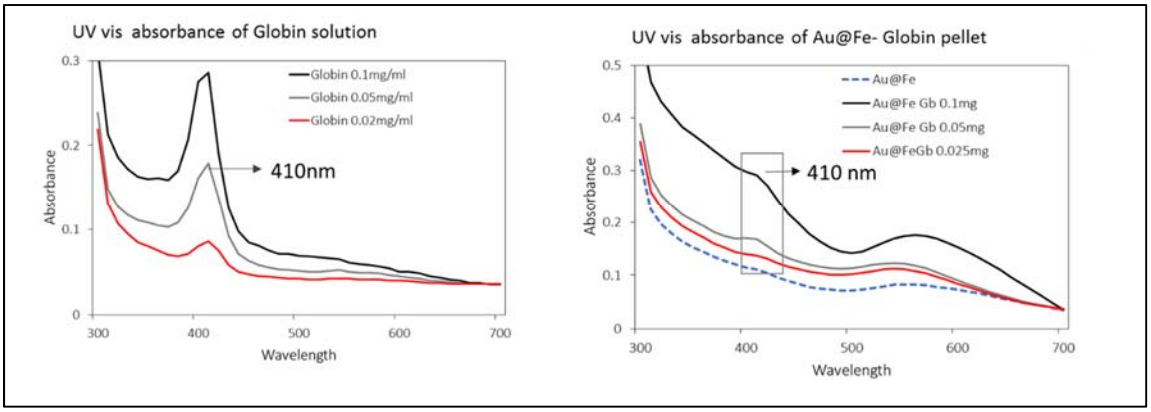

Figure 12: a) UV-Vis absorbance of Globin solutions at different concentrations b) UV-vis absorbance of Magnetically separated pellet of Au@Fe-anti globin Ab and Au@Fe-Peg

Figure 13: a) Globin capture efficiency of Au@Fe-anti Globin Ab at varying Globin concentrations b) Globin capture efficiency of Au@Fe-anti Globin Ab from 50µg/ml solution at different time points

a)

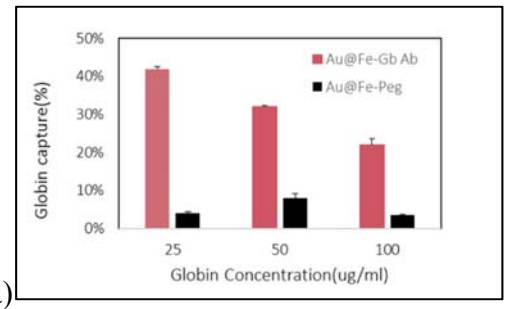

b)

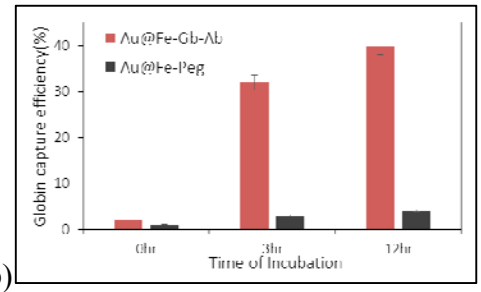

1.3.4 Antibody selection for trophoblast isolation

HLA-G expression of the Jeg 3 and trophoblast cells extracted from the placental tissue was confirmed using western blot and Flow cytometry analysis. There are different antibodies against HLA-G based on the isoform (denatured and conformational) of HLA-G. The two commonly used HLA-G antibody epitopes that are reported in literature were 4H84 and MEM-G9 (Apps et al., 2008) . 4H84 is made against the denatured isoform while the MEM-G9 is against the

transmembrane isoform. Western blot and Flow cytometry experiments were conducted with both MEM-G9 and 4H84 epitopes as well as βHCG antibody. MEM-G9 expression in both Jeg3 and trophoblast cells was found to be 3 folds higher than 4H84 expression (Figure 14). Comparable results were reflected from flow cytometry experiments. βHCG expression was found to be higher in Jeg3 as compared to trophoblast cells (Figure 15). Both the isoforms of anti-HLAG antibody (4H84 and MEM G9) individually and as a combination were used to target the trophoblast cells by conjugating the antibodies with magnetic nanoparticles (Au@Fe and Fe NC). Anti-βHCG antibody was used for counterstaining in Fluorescence imaging applications.

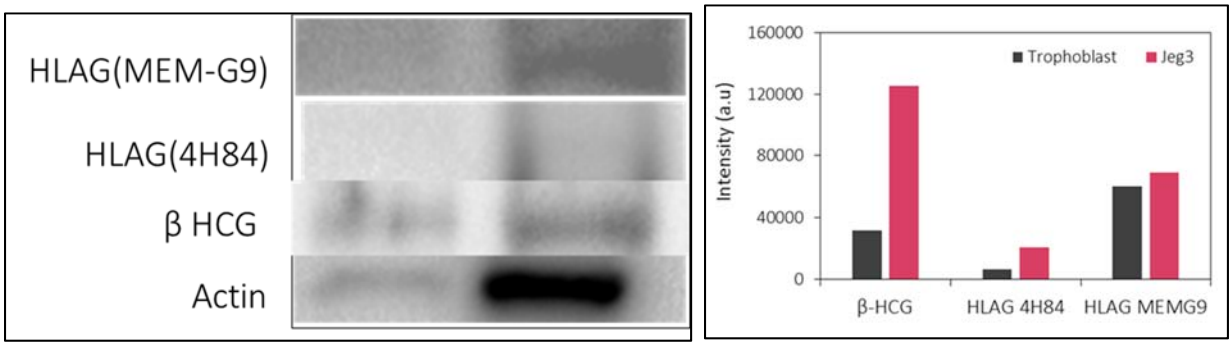

Figure 14: Western Blot images of expression of HLA-G (4H84), HLA-G (MEM-G9), β HCG and analysis of images

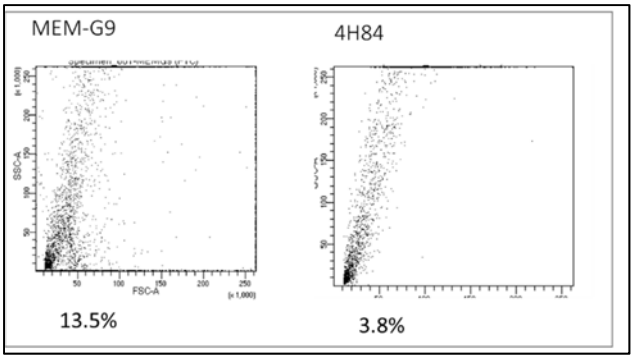

Figure 15: Flow cytometry analysis of 4H84 and MEM G9 expression of trophoblast cells

1.3.5 Magnetic Cell Capture Efficiency of Nanoparticles

To determine the capture efficiency of Au@Fe-Ab and FeNC-Ab nanoparticles, Jeg3 cells (10^5cells/ml) were stained with a nuclear staining Hoechst 3342 dye and incubated with anti-HLAG antibody at 37^{o}C for two hours. Magnetic nanoparticles (Au@Fe and FeNC) without antibody were used as control. Prior to cell capture efficiency, the amount of antibody to be conjugated to the nanoparticles for maximum capture efficiency of the JEG-3 cells was optimized by using magnetic nanoparticles prepared with different concentrations of HLA-G antibody. (Figure 16). From the optimization experiments it was determined that 20νμg (0.5mg/ml HLAG) of the antibody is required for optimal (~75%) capture efficiency. The capturing efficiency of both MNPs were determined by fluorescence imaging (Figure 17). The magnetic nanospheres captured the target cells with an efficiency of 75% whereas the magnetic nanocubes captured the target cells with a target efficiency of 70% (Figure 18).

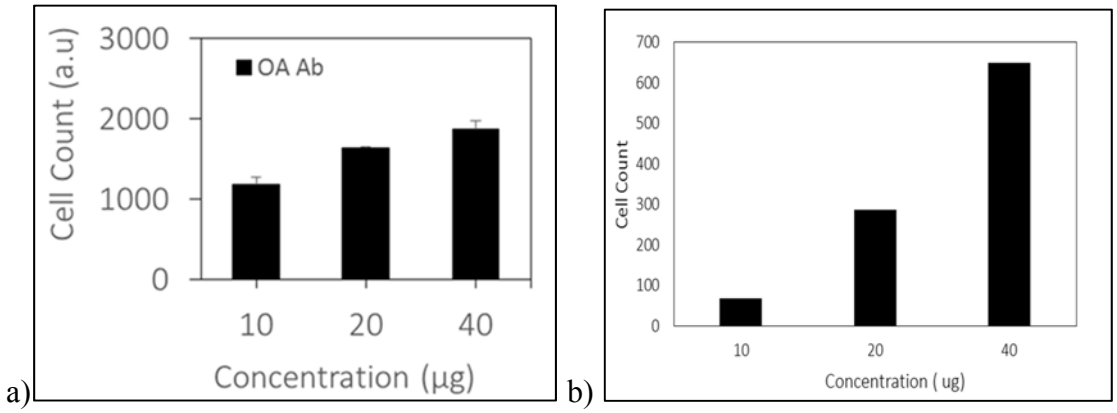

Figure 16: Optimization of antibody conjugation for a) Au@Fe Nanoparticles and b) Fe Nanocubes

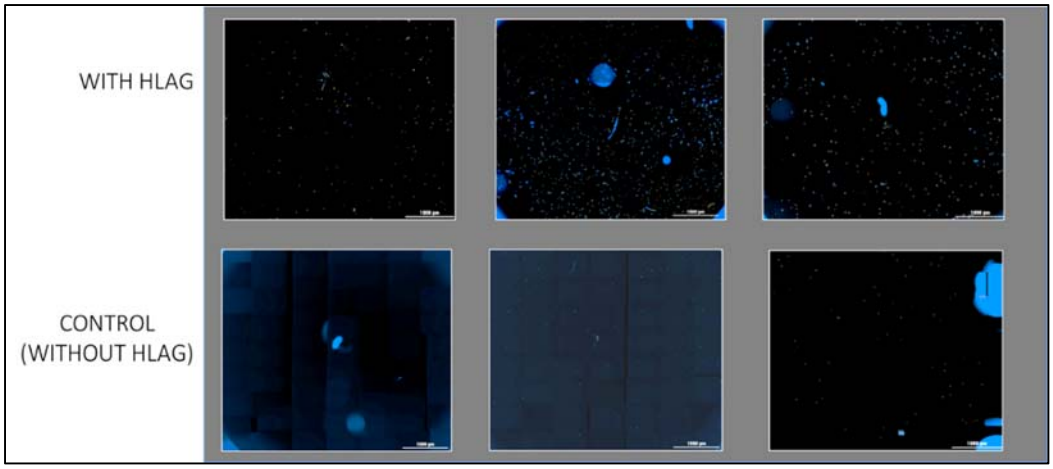

Figure 17: Fluorescent Images of Jeg3 cells captured with magnetic nanoparticles with and without antibody

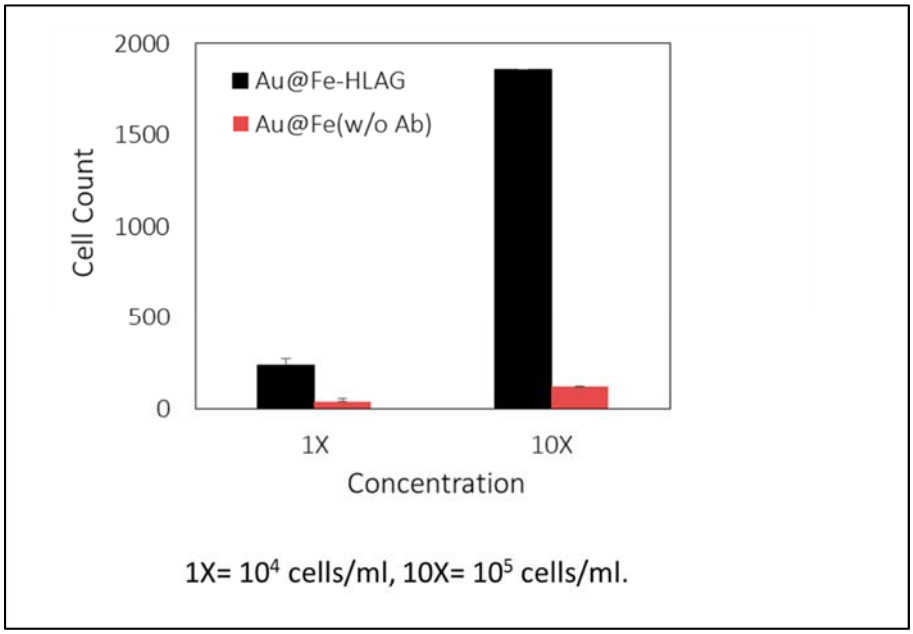

Figure 18: Number of cells captured from a pool of 10^4 and 10^5 Jeg3 cells by magnetic nanoparticles

1.3.6 Cell Capture Specificity with JEG 3

The selectivity of the Au@Fe-Ab and FeNC-Ab nanoparticles was determined using a mixture of JEG-3 cells that overexpress HLA-G with SKBR-3 cells that have minimal or no HLAG expression. Typically, these two cells were mixed at a ratio of 1:1and incubated with Au@Fe-

4H84 and FeNC-4H84 antibody for 2 hours followed by magnetic washing and imaging under fluorescence microscope. The Jeg3 cells were stained with membrane staining C10446 dye while the SkBr3 cells were stained with nuclear staining Hoechst 3342 dye. The specificity of MNPS to isolated JEG-3 cells was determined by fluorescence imaging. MNPs were capable of isolating 65% of Jeg3 cells was 65% compared to 2.5%, of SKBR-3 confirming the preferential capture of MNPs JEG-3 over SKBr-3 cells (Figure 19 b).

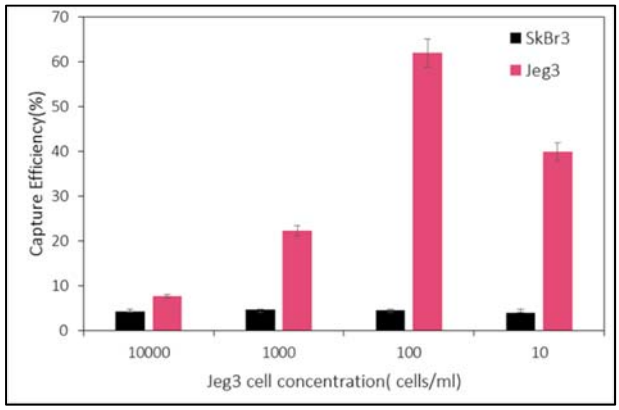

Figure 19: Cell capture efficiency of the magnetic nanoparticles in pool of 10^4 cells/ml SKBr3 and Jeg3 cells of varying concentrations

The specificity of MNPS were tested with Jeg3 cells spiked in a pool of epithelial cells obtained from the swab sample of non-pregnant women. Jeg 3 cells of varying concentrations were spiked in a constant pool of in epithelial cells (10^4 cells) and were incubated with anti-HLAG-4H84-MEM G9 conjugated Au@Fe nanoparticles (Figure 20). The capture efficiency of the nanoparticles was around 70% for 10 cells spiked in 10,000 nonspecific cells. The capture efficiency decreased with increasing number of Jeg 3 cells suggesting that at higher concentrations of Jeg 3 the cell capture efficiency of the nanoparticles reached a saturation point.

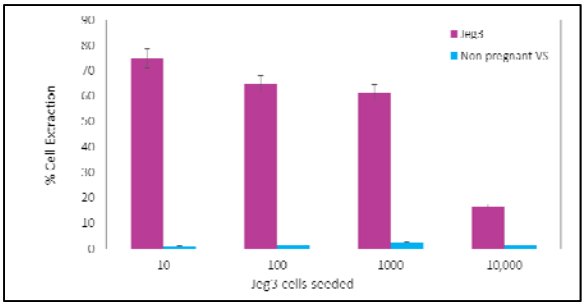

Figure 20: Cell capture efficiency of the magnetic nanoparticles in pool of 10^4 cells/ml VS and Jeg3 cells of varying concentrations

β HCG-Cy5 staining and fluorescent imaging was performed on the cells pre-stained with Hoechst 3342 after separation with Au@Fe and FeNc nanoparticles. The fluorescent images confirmed the capturing efficiency and specificity of Au@Fe nanoparticles to isolate JEG-3 cells (Figure 21).

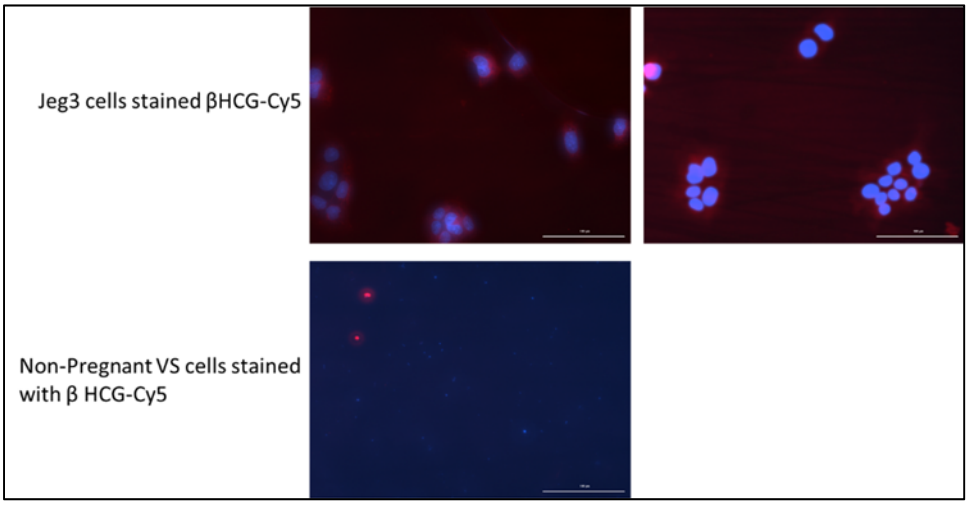

Figure 21: Fluorescent imaging of the β HCG staining of Jeg3 and Non pregnant VS cells

1.3.7 Magnetic Cell Capture of trophoblast cells

Following the promising results with Jeg3 cells we investigated the efficacy of the magnetic particles in capturing trophoblast cells from a pool of epithelial cells. We used a mixture of trophoblast cells isolated from discarded placenta and epithelial cells isolated from non-pregnant

women vaginal swab samples. We spiked trophoblast cells at different concentrations (1:1, 1:10.1:100 and 1:1000)with epithelial cells obtained from a swab sample of non-pregnant women. The trophoblast cells were stained with C10446 dye (Red) and the non-pregnant vaginal swab samples were stained with Hoechst 3342 (Blue) dye The cells were incubated with Fe-HLAG and Au@Fe-HLAG separately at 37ºC for two hours followed by magnetic isolation and washing. We conducted magnetic separation experiment with Au@Fe-MEM G9-4H84 and FeNC-MEM G9-4H84 conjugates. The extraction efficiency for the trophoblast cells was determined by fluorescence imaging. The imaging results showed that the efficiency as around 70% for 1:1 and 1:10 ratios for both Au@Fe- MEM G9-4H84 and FeNC- MEM G9-4H84 conjugates. The individual and overlayed fluorescent images are shown in (Figure 22). For lower ratios (1:100, 1:1000) the extraction efficiency increased to 85%. (Figure 23). The cell capture efficiency of the Au@Fe- MEM G9-4H84 and FeNC- MEM G9-4H84 conjugates were compared with the cell capture efficiency of Au@Fe-4H84 and FeNC-4H84 conjugates. Au@Fe-4H84-MEM G9 conjugate demonstrated a capture efficiency of 85% while Au@Fe-4H84 conjugate demonstrated a capture efficiency of 60% (Figure 24). FeNC-4H84-MEM G9 conjugate demonstrated a capture efficiency of 75% while FeNC-4H84 conjugate demonstrated a capture efficiency of 45% (Figure 24). From the above experiments, Au@Fe-4H84-MEM G9 and Fe NC-4H84-MEM G9 were selected as the candidate nanoparticles for further trophoblast cell isolation and capture experiments and for clinical studies with swab samples from pregnant women.

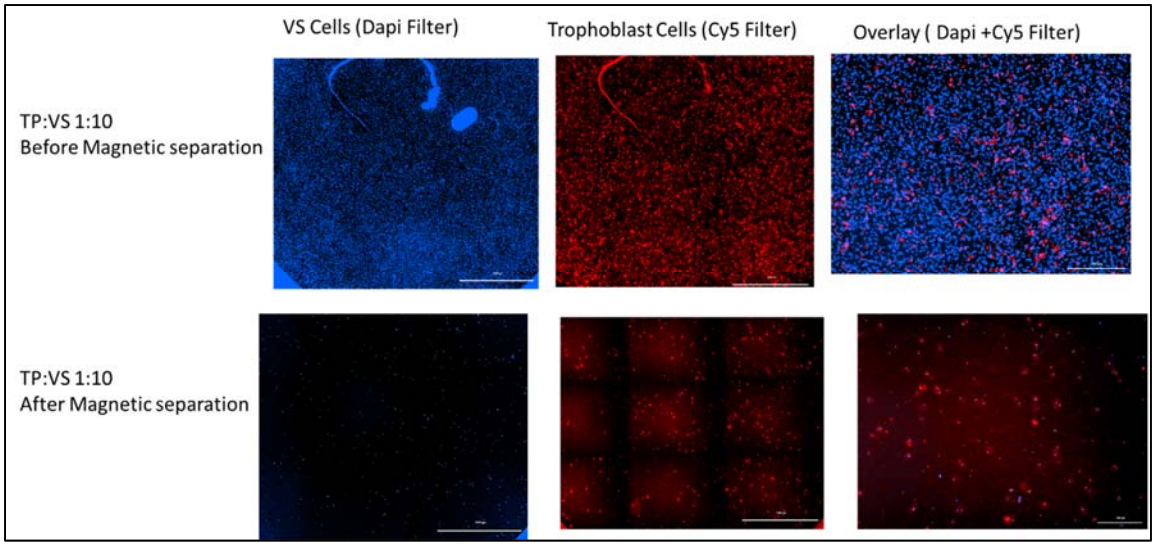

Figure 22: Fluorescent Images of trophoblast cells spiked in VS cells in 1:10 ratio before and after magnetic separation

a)

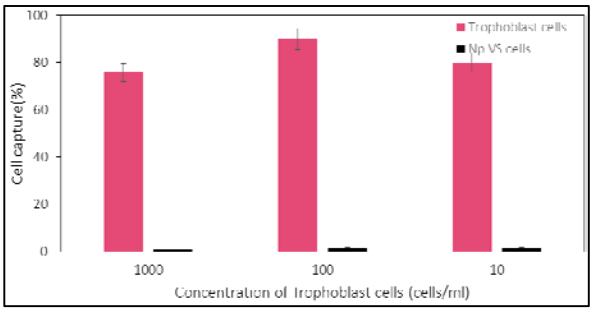

b)

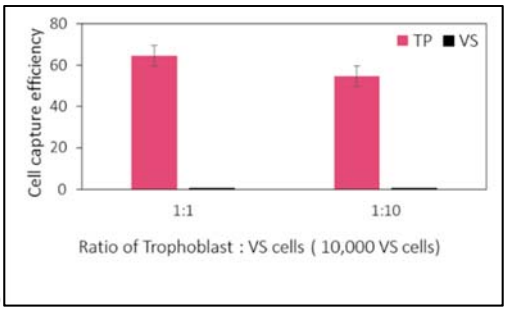

Figure 23: Cell capture efficiency of the magnetic nanoparticles in capturing trophoblast cells of varying concentration from a pool of epithelial cells (Non Pregnant vaginal swab cells) b) Cell capture efficiency of magnetic nanoparticles from TP and VS cells in 1:1 (10^4TP: 10^4VS) and 1:10 (10^3TP: 10^4VS) ratio

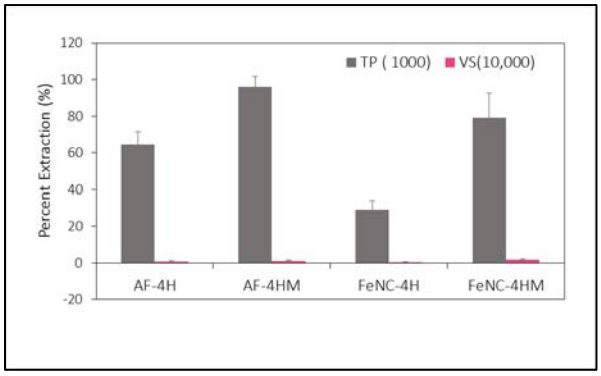

Figure 24: Cell capture efficiency of the Au@Fe and FeNC magnetic nanoparticles conjugated with 4H84 and 4H84-MEM G9 from a pool of TP cells and NP VS

1.3.8 DNA Analysis

To confirm the capture of trophoblast cells from the pool of epithelial cells, the DNA from the magnetically isolated cells were extracted and amplified using RT PCR with X and Y chromosome specific primers and electropherogram was recorded. DNA was obtained for sequencing from the cells before and after magnetic separation. Since the trophoblast cells are from a male placenta the trophoblast cells are expected to show both X and Y allele while the epithelial cells isolated from non-pregnant women should show only X alleles. In a sample with trophoblast and mother's cells mixed in a ratio of 1:10, the Y allele will be significantly less. However, in cells obtained following magnetic separation, the Y allele peak should be at least two fold higher compared to the original swab sample. The peak ratios of the X and Y allele show that there has been 50-65% enrichment in the trophoblast cells fluorescence imaging studies. The electropherogram recorded for the samples isolated by MNPS are shown in (Figure 25).

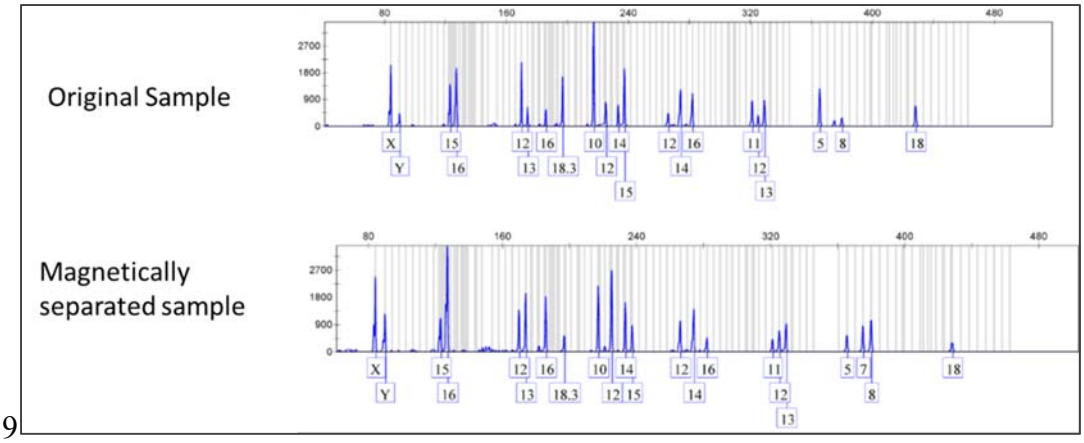

9

Figure 25 a): Electropherogram Images of Trophoblast cells spiked in VS in 1:10 ratio before and after magnetic separation.

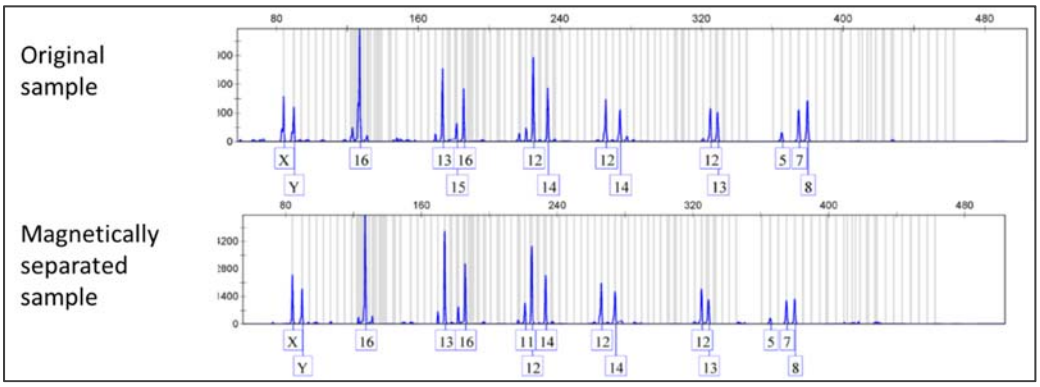

Figure 25 b): Electropherogram Images of Trophoblast cells spiked in VS in 1:1 ratio before and after magnetic separation.

The DNA analysis of the isolated trophoblast cells demonstrated a cell capture efficiency of 50% for trophoblast cells spiked in VS cells in 1:1 (Figure 25 a) and 1:10 (Figure 25 b) ratios. We performed the DNA analysis experiments for 10 trophoblast cell and 10 Non pregnant VS cell samples. The cell capture efficiency demonstrated with fluorescent analysis was not translated DNA analysis results. From previous DNA analysis experiments, it was established that an enrichment of 1:8 (80%) is preferred for clinical purpose.

We conducted the magnetic separation studies with trophoblast cells spiked with epithelial cells by HLAG saturation experiment to explore whether higher capture efficiencies were obtained.

Trophoblast cells were mixed in varying ratios with VS cells and were incubated (saturated) with anti HLAG antibodies (4H84 and MEM-G9) for 2 hours. Following incubation, Au@Fe-IgG or Fe-IgG nanoparticles were added and incubated for 2 hours. The cells were then imaged under fluorescence microscope and analyzed with Cytation 5 software. Fe NC-IgG conjugate demonstrated a cell capture efficiency of 75% while AF-IgG demonstrated a cell capture efficiency of 60% (Figure 26 a). The trophoblast to VS cell capture ratio was calculated for Au@Fe-IgG and FeNC-IgG conjugates and compared with that of Au@Fe-4H84-MEM G9 and Fe-4H84 -MEM G9 conjugates (Figure 26 b). The trophpblast to VS cell capture ratio was 10:1 for Fe NC-IgG conjugate, while the ratio was 8:1 for Au@Fe-IgG conjugates which was two times higher than that of Au@Fe-4H84-MEM G9 and Fe NC-4H84-MEM G9 conjugates.

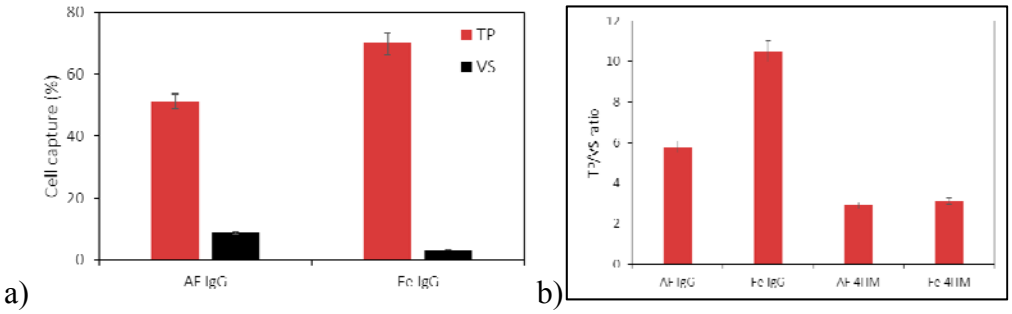

Figure 26: a) Cell capture efficiency of magnetic nanoparticles with HLAG saturation method b) The trophoblast/VS capture ratio of Au@Fe and Fe nanoparticles with HLAG saturation and direct conjugation method.

The isolated cells were treated with DNAse and lysed to extract DNA for DNA quantification and subsequent DNA amplification with PCR for X and Y chromosomes. The ratio of the X and Y peak for isolated cells was 75% of the original mixture suggesting that there has been a 75% enrichment in the isolated cells (Figure 28). The use of saturation procedures increased the enrichment to 90%. (Figure 27).

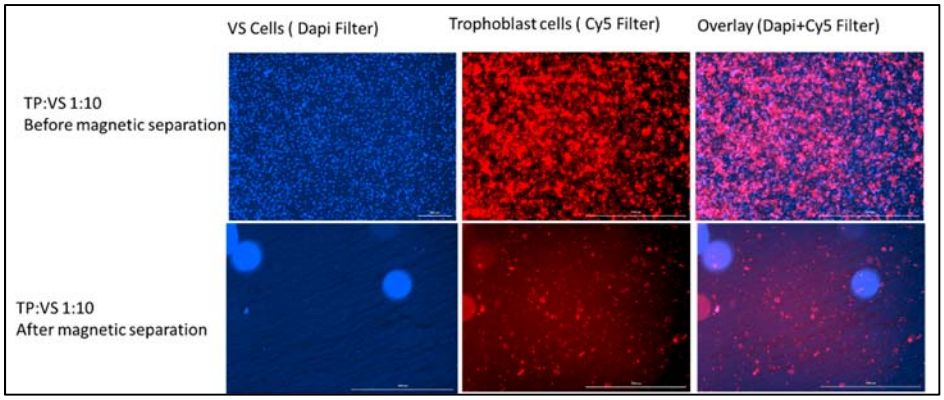

Figure 27: Fluorescent images of the trophoblast and VS cells mixed in 1:10 ratio before and after separation

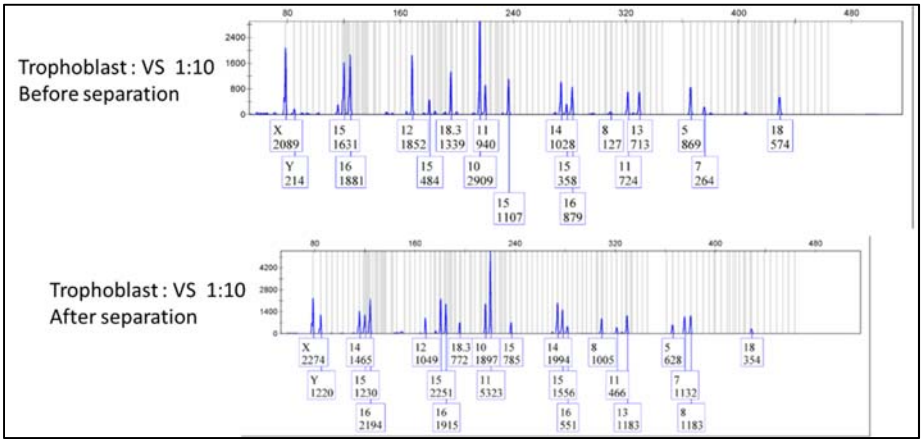

Figure 28: Electropherogram Images of Trophoblast cells spiked in VS in 1:10 ratio before and after magnetic separation with HLAG saturation method

1.3.9 Isolation of Trophoblast cells in pregnant women samples

Encouraged by the positive results from the simulation studies, experiments were conducted on vaginal swab samples collected from pregnant women (5-12 weeks). A total of 45 Swab samples were collected from the Missouri OB/GYN Associates (MOBA) at the University of Missouri. The presence of trophoblast cells in the vaginal swab sample was confirmed by IHC analysis with

CK 7. CK 7 is a specific trophoblast cell marker and is commercially available for IHC staining. The cells slides were analyzed under the microscope by a pathologist. We conducted IHC experiments with CK7 antibody on three swab samples prior to magnetic separation to confirm the presence of the trophoblast cells in the swab samples (Figure 29). We confirmed that there were 1 trophoblast cell for every 1000-1500 epithelial cells in the swab sample.

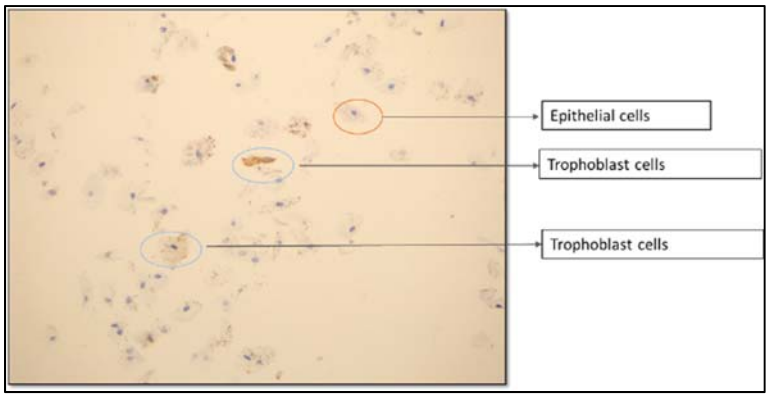

Figure 29 IHC stain images of cells from swab sample from pregnant women before magnetic separation

The swab samples were then separated using Au@Fe-4H84-MEM G9 and FeNC-4H84-MEM G9 using and washed. Immunohistochemistry was performed on the isolated cells using anti-CK-7 antibody. A lot of cellular debris was observed. The cellular debris may be due to the isolation of cells using FeNC particles that had higher magnetic moment compared to Au@Fe (Figure 30). We repeated the isolation with less powerful magnet and noticed less celluar debris

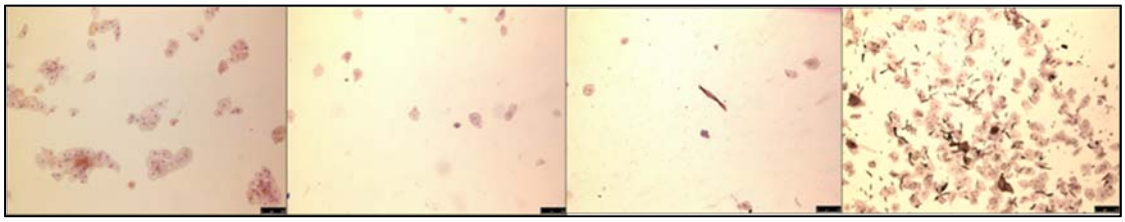

Figure 30 IHC stain images of cells from swab sample from pregnant women after magnetic separation

Trophoblast isolation efficiency was explored using the AuFe-4H84-MEM G9 (direct isolation method) and HLAG saturation method. The isolated cells were stained with nucleus staining Hoechst 3342 dye (Blue) and were then counterstained with β HCG-Cy5 (Red). The counter stained cells were imaged and analyzed using Cytation 5. The first 8 samples were analyzed using direct isolation method while the rest of the 10 samples were analyzed using the HLAG saturation method (Figure 31 a). The average cell number was around 1100 cells in a sample of $3*10^6$ cells/ml (Figure 31 b) which was comparable to the trophoblast cell count isolated from cervical samples (Fritz et al, 2015) (Bolnick et al, 2014). We observed from our initial fluorescence studies that the trophoblast cell count of the vaginal swab samples obtained from pregnant women with 5-12 weeks of gestation age was comparable to cervical swab samples collected from pregnant women (Bolnick et al, 2014).

a) 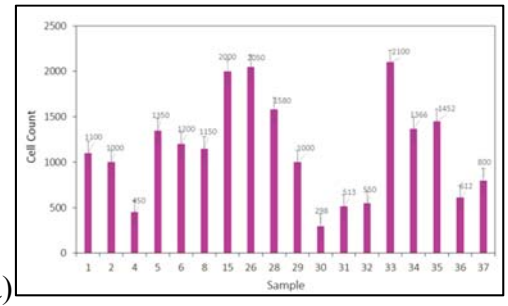

b) 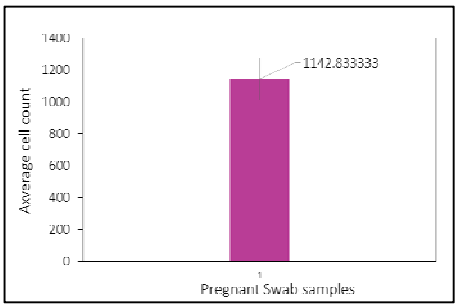

Figure 31 a) Trophoblast cell count of individual samples b) Average cell count of all the samples.

DNA analysis: DNA was extracted from the isolated trophoblast cells to demonstrate that even after magnetic separation, the trophoblast cells remained intact and genetic information could be extracted from them. 12 swab samples were collected and trophoblast cells were isolated using Direct conjugation method with FeNC-IgG nanoparticles. DNA was extracted from the isolated cells using ethanol precipitation and quantified using Qiagen Investigator kit. According to the trophoblast cell count obtained from IHC experiments and from literature reports (Bolnick et al,

2014) (Fritz et al, 2015). The average total cell count from the swab varied from $1*10^6$ cells/ml – $3*10^6$ cells/ml. It has been reported in literature that each cell contributes approximately 6.5 picograms of DNA (Georgiou & Papapostolou, 2006). Extrapolating from the above calculations, we can extrapolate that the amount of trophoblast DNA extracted from the vaginal swab samples will vary from 1 ng to 4 ng depending on the number of total cells in the sample. It was observed from the DNA quantification experiments, that individual DNA amount varied in each sample (Figure 32 a), however the average DNA count was around 3.5ng (Figure 32 b) which was comparable to our theoretically calculated value. To confirm whether the DNA extracted was from trophoblast cells, short tandem repeat (STR) sequencing was performed on the amplified DNA extracted from the trophoblast cells. Out of the 8 samples, three samples were lost to bacterial contamination. The remaining samples were analyzed with genetic analyzer. A male profile was obtained from two samples possibly suggesting that the DNA extracted is that from a male fetus (Figure 33). A female profile was obtained from the two other samples, possibly suggesting that the DNA extracted was from a female fetus

a) 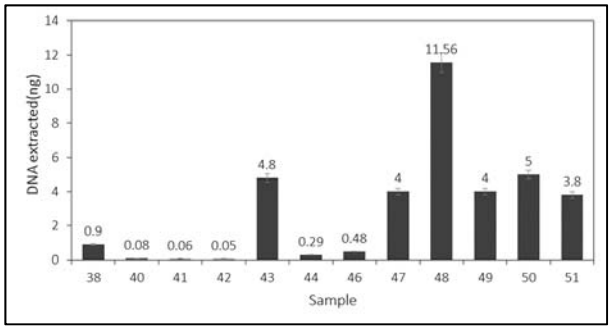

b) 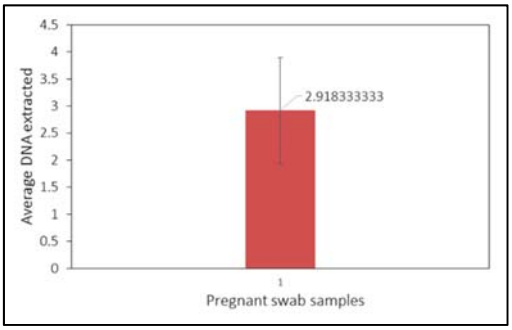

Figure 32 a) DNA quantification of individual samples b) Average DNA quantification for all the samples.

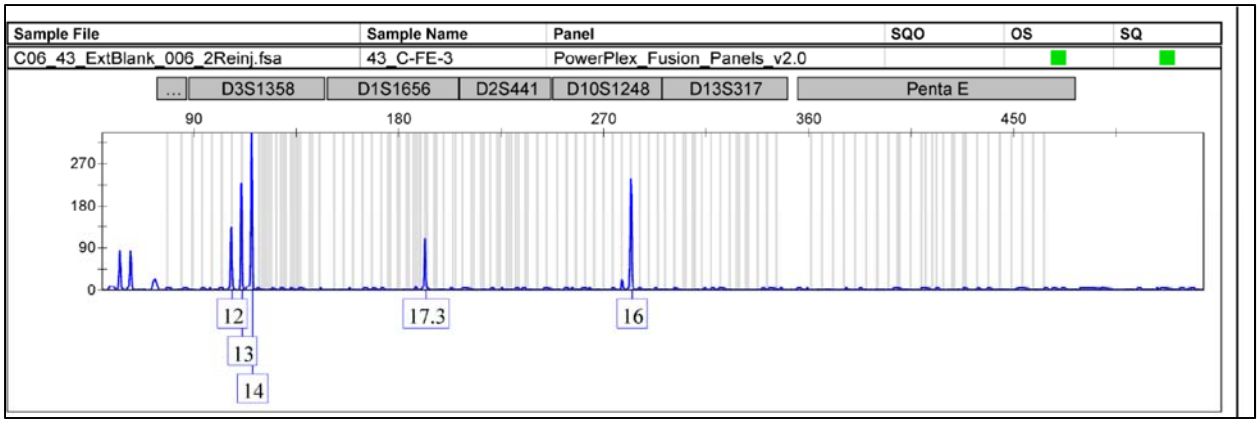

Figure 33 Electropherogram image of the extracted DNA shows a male profile suggesting the DNA could be from a male fetus

1.4 Conclusion:

We hypothesized that trophoblast cells can be selectively isolated from the vaginal swab of the pregnant woman in the first trimester of pregnancy using magnetic nanoparticles surface conjugated with monoclonal antibodies specific to surface receptors present on the trophoblast cells. We synthesized Au@Fe and Fe NC nanoparticles and then conjugated them with anti-HLAG antibodies as well as IgG. Two different epitopes of HLA-G antibody were used for the experiments (4H84 and MEM G9). For maximum selection efficiency, we conjugated both the epitopes, MEM G9 and 4H84 to the Au@Fe and Fe NC. The target binding affinity and capturing efficiency of the MNPs were confirmed using surrogate antigen and anti- Globin antibody (anti-Globin Ab) as the target antibody. The experiments proved that Au@Fe-anti Globin Ab and Fe NC-anti Globin Ab can capture target antigen with a detection range of 0.1-100ug/ml. We then conducted target binding studies with human choricarcinoma (Jeg3) and breast cancer (SKBr3) cells to determine the sensitivity and selectivity of the magnetic nanoparticles. The Au@Fe-4H84 and Fe Nc-4H84 nanoparticles demonstrated a capture efficiency of 75%. We then conducted clinical studies to test whether magnetic nanoparticles can selectively isolate trophoblast cells from a pool of epithelial cells. Trophoblast cells were

extracted from placental tissues of male fetus and spiked in epithelial cells obtained from the vaginal swab obtained from non-pregnant women. Two different extraction methods were used, direct incubation and HLA-G saturation. The isolated cells were imaged under fluorescence and DNA was extracted to amplify them using PCR and were analyzed using STR sequencing. The capture efficiency of direct conjugation method was around 65-70% according to fluorescence images. DNA analysis also demonstrated a 50-65% enrichment of the trophoblast cells. Capture efficiency of HLA-G saturation method was around 75-80% according to fluorescent images, DNA analysis demonstrated a 75% enrichment of the trophoblast cells. We then conducted clinical studies on samples on swab samples collected from pregnant women in the first trimester of pregnancy. Cells were isolated using direct conjugation and HLA-G saturation methods. The cells were stained with βHCG-Cy5 and analyzed under fluorescent microscope. Immunocytochemistry with CD10 and CK7 antibodies was conducted on the extracted trophoblast cells. According to IHC analysis there were approximately 1 trophoblast cell in every 2000 epithelial cells (Bolnick et al, 2014). The cells were enriched after magnetic separation. DNA was extracted from the isolated cells and the amplified and quantified using PCR. The amount of DNA extracted corroborated with the theoretical analysis. Some samples were contaminated by bacteria and DNA was degraded due to environmental factors.

A male profile was obtained from the extracted DNA from some of the samples suggesting that the DNA could be from the male fetus. Thus, in conclusion, we have demonstrated that magnetic nanoparticles can extract trophoblast cells from a sample (less than 12 weeks GA) with around 75% efficiency.

We developed a library of magnetic nanoparticles and proved that they could be utilized to capture target cells from a pool of non-specific cells in clinical settings with 75% to 80% efficiency. Further Optimization is required to increase the capture efficiency and to reduce entrapment of the nanoparticles in excess mucus.

References

Apps, R., Gardner, L., & Moffett, A. (2008). A critical look at HLA-G. *Trends in Immunology,29*(7), 313-321. doi:10.1016/j.it.2008.02.012

Bolnick, J. M., Kilburn, B. A., Bajpayee, S., Reddy, N., Jeelani, R., Crone, B., . . . Armant, D. R. (2014). Trophoblast retrieval and isolation from the cervix (TRIC) for noninvasive prenatal screening at 5 to 20 weeks of gestation. *Fertility and Sterility, 102*(1), 135-142.e136. doi:10.1016/j.fertnstert.2014.04.008

Douglas, G. C., & King, B. F. (1989). Isolation of pure villous cytotrophoblast from term human placenta using immunomagnetic microspheres. *J Immunol Methods, 119*(2), 259-268.

Frey, N. A., Peng, S., Cheng, K., & Sun, S. (2009). Magnetic nanoparticles: synthesis, functionalization, and applications in bioimaging and magnetic energy storage. *Chemical Society Reviews, 38*(9), 2532. doi:10.1039/b815548h

Fritz, R., Kohan-Ghadr, H. R., Sacher, A., Bolnick, A. D., Kilburn, B. A., Bolnick, J. M., . . . Armant, D. R. (2015). Trophoblast retrieval and isolation from the cervix (TRIC) is unaffected by early gestational age or maternal obesity. *Prenatal Diagnosis, 35*(12), 1218-1222. doi:10.1002/pd.4681

Georgiou, C. D., & Papapostolou, I. (2006). Assay for the quantification of intact/fragmented genomic DNA. *Analytical Biochemistry, 358*(2), 247-256. doi:10.1016/j.ab.2006.07.035

Heng, Y. J., Liong, S., Permezel, M., Rice, G. E., Di Quinzio, M. K. W., & Georgiou, H. M. (2015). Human cervicovaginal fluid biomarkers to predict term and preterm labor. *Frontiers in Physiology, 6*. doi:10.3389/fphys.2015.00151

Hui, P. (2012). *Gestational trophoblastic disease : diagnostic and molecular genetic pathology*. New York: Humana Press.

Imudia, A. N., Kumar, S., Diamond, M. P., DeCherney, A. H., & Armant, D. R. (2010). Transcervical retrieval of fetal cells in the practice of modern medicine: a review of the current literature and future direction. *Fertility and Sterility, 93*(6), 1725-1730. doi:10.1016/j.fertnstert.2009.11.022

Imudia, A. N., Suzuki, Y., Kilburn, B. A., Yelian, F. D., Diamond, M. P., Romero, R., & Armant, D. R. (2009). Retrieval of trophoblast cells from the cervical canal for prediction of abnormal pregnancy: a pilot study. *Hum Reprod, 24*(9), 2086-2092. doi:10.1093/humrep/dep206

Jain, C. V., Kadam, L., van Dijk, M., Kohan-Ghadr, H. R., Kilburn, B. A., Hartman, C., . . . Drewlo, S. (2016). Fetal genome profiling at 5 weeks of gestation after noninvasive isolation of trophoblast cells from the endocervical canal. *Science Translational Medicine, 8*(363), 363re364-363re364. doi:10.1126/scitranslmed.aah4661

Ji, L., Brkic, J., Liu, M., Fu, G., Peng, C., & Wang, Y. L. (2013). Placental trophoblast cell differentiation: physiological regulation and pathological relevance to preeclampsia. *Mol Aspects Med, 34*(5), 981-1023. doi:10.1016/j.mam.2012.12.008

Kavanagh, D. M., Kersaudy-Kerhoas, M., Dhariwal, R. S., & Desmulliez, M. P. (2010). Current and emerging techniques of fetal cell separation from maternal blood. *J Chromatogr B Analyt Technol Biomed Life Sci, 878*(22), 1905-1911. doi:10.1016/j.jchromb.2010.05.007

Li, L., & Schust, D. J. (2015). Isolation, purification and in vitro differentiation of cytotrophoblast cells from human term placenta. *Reproductive Biology and Endocrinology, 13*(1). doi:10.1186/s12958-015-0070-8

Nakajima, N., & Ikada, Y. (1995). Mechanism of amide formation by carbodiimide for bioconjugation in aqueous media. *Bioconjug Chem, 6*(1), 123-130.

Nelson, P. N., Reynolds, G. M., Waldron, E. E., Ward, E., Giannopoulos, K., & Murray, P. G. (2000). Monoclonal antibodies. *Mol Pathol, 53*(3), 111-117.

Pankhurst, Q. A., Connolly, J., Jones, S. K., & Dobson, J. (2003). Applications of magnetic nanoparticles in biomedicine. *Journal of Physics D: Applied Physics, 36*(13), R167.

Park, J., An, K., Hwang, Y., Park, J. G., Noh, H. J., Kim, J. Y., . . . Hyeon, T. (2004). Ultra-large-scale syntheses of monodisperse nanocrystals. *Nat Mater, 3*(12), 891-895. doi:10.1038/nmat1251

Red-Horse, K., Zhou, Y., Genbacev, O., Prakobphol, A., Foulk, R., McMaster, M., & Fisher, S. J. (2004). Trophoblast differentiation during embryo implantation and formation of the maternal-fetal interface. *Journal of Clinical Investigation, 114*(6), 744-754. doi:10.1172/jci200422991

Robinson, I., Tung le, D., Maenosono, S., Walti, C., & Thanh, N. T. (2010). Synthesis of core-shell gold coated magnetic nanoparticles and their interaction with thiolated DNA. *Nanoscale, 2*(12), 2624-2630. doi:10.1039/c0nr00621a

Tarrade, A., Lai Kuen, R., Malassine, A., Tricottet, V., Blain, P., Vidaud, M., & Evain-Brion, D. (2001). Characterization of human villous and extravillous trophoblasts isolated from first trimester placenta. *Lab Invest, 81*(9), 1199-1211.

Teng, X., & Yang, H. (2004). Effects of surfactants and synthetic conditions on the sizes and self-assembly of monodisperse iron oxide nanoparticlesElectronic supplementary information (ESI) available: XRD data of iron oxide nanoparticles, Fig. S1 and S2. See

http://www.rsc.org/suppdata/jm/b3/b311610g. *Journal of Materials Chemistry, 14*(4), 774. doi:10.1039/b311610g

Xu, C., & Sun, S. (2009). Superparamagnetic nanoparticles as targeted probes for diagnostic and therapeutic applications. *Dalton Transactions*(29), 5583. doi:10.1039/b900272n

Zhang, S., Gong, M., Zhang, D., Yang, H., Gao, F., & Zou, L. (2014). Thiol-PEG-carboxyl-stabilized Fe 2 O 3 /Au nanoparticles targeted to CD105: Synthesis, characterization and application in MR imaging of tumor angiogenesis. *European Journal of Radiology, 83*(7), 1190-1198. doi:10.1016/j.ejrad.2014.03.034

Zhen, G., Muir, B. W., Moffat, B. A., Harbour, P., Murray, K. S., Moubaraki, B., . . . Hartley, P. G. (2011). Comparative Study of the Magnetic Behavior of Spherical and Cubic Superparamagnetic Iron Oxide Nanoparticles. *The Journal of Physical Chemistry C, 115*(2), 327-334. doi:10.1021/jp104953z

Zhu, X., Han, T., Yin, G., Wang, X., & Yao, Y. (2011). Expression of Human Leukocyte Antigen-G during Normal Placentation and in Preeclamptic Pregnancies. *Hypertension in Pregnancy, 31*(2), 252-260. doi:10.3109/10641955.2011.638955

CHAPTER 2

NANOPARTICLE BASED ASSAY FOR SCREENING RETINOPATHY OF PREMATURITY (ROP)

2.1 Introduction

2.1.1 Retinopathy of Prematurity (ROP)

Retinopathy of Prematurity (ROP) is a retinal vascular disease which causes disrupted retinal blood vessel growth in premature infants born before 32 weeks of gestation or weighing under 1500gm (Ates et al., 2009). ROP inhibits the retinal neuronal and vascular development in the preterm infant that results in aberrant vascularization of the retina. ROP is one of the leading causes of blindness among infants and children(Chen & Smith, 2007). According to the National Eye Institute, out of the 3.9 million babies born every year, around 14,000-16,000 are expected to develop ROP of varying severity. It is estimated that approximately 10% of the infants with ROP will develop stage 3 or higher ROP which often leads to retinal detachment or blindness (Hellstoerm et al, 2013).

2.1.2 Clinical Diagnosis and Challenges

The current diagnostic procedure for ROP involves a physical fundus exam of premature infants who are at higher risk of developing ROP. In this procedure, the dilated eye of the infant is examined by an ophthalmologist using an ophthalmoscope to detect the vascular damages in the retina of the infant. The major risk factors of the ROP are the gestational age at birth (less than 32 weeks) and very low birth weight (less than 1500 gm).

The results are grouped in three categories: Normal retina, immature retinal vasculature and ROP. ROP is characterized by location of proliferation (Zone) and the severity of vascular damage (Stage) and the presence of circuitous (tortuous) blood vessels in retina. Zones are classified as Zone 1, Zone 2 and Zone 3 with zone 1 being a circular disc including the center of vision of the infant. Zone 2 is concentrically outside of zone 1 where it extends to Ora serrata. Zone III is the remaining temporal crescent of the retina(Asano et al,2014) (Figure 34).

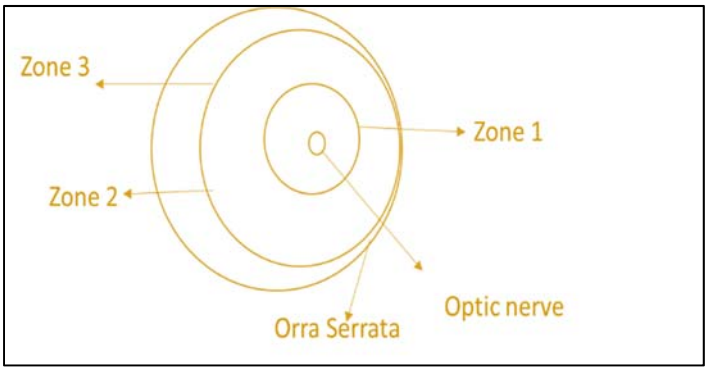

Figure 34 The different zones of an embryonic retina to determine the ROP status

ROP is graded as different stages; stage 1 is determined by a demarcation line formed by blood vessel at the avascular junction of retina. If the blood vessels proliferate further they gain depth and height and form ridge like structure, it is categorized as stage 2 ROP. In stage 3, the blood vessels grow further vertically into the vitreous plane and forms a mat or cord of blood vessels (Asano et al, 2014). The mat like structure may cause scar formation due to contractile element which creates tension along the retinal and vitreous surfaces leading to semi retinal detachment (Stage 4) or complete retinal detachment (Stage 5) (Figure 34). Stage 5 ROP may lead to complete blindness. The fundus photographs of different stages of ROP is shown in Figure (35).

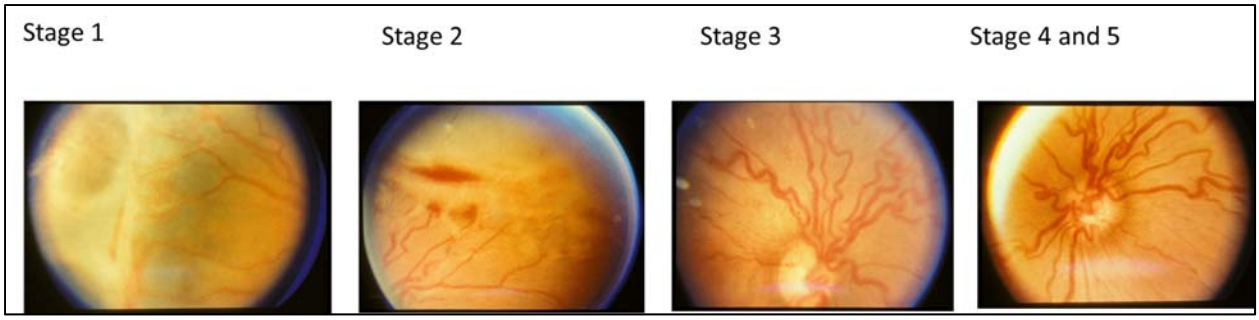

Figure 35: Fundus Photograph of various stages of ROP

Timely screening of premature born infants who are at a higher risk of developing ROP is a valuable tool in controlling the incidence of ROP. However, so far, the diagnosis and screening technique for ROP is the same which involves a physical eye examination by the ophthalmologist by dilating the eye of the infant. The first examination is performed by 31-week postmenstrual age or by 4 weeks chronologic age, with additional examinations performed repeatedly thereafter to detect late stage ROP requiring treatment. The physical examination process also involves subjecting the infant to a bright source of light for the ophthalmologist to be able to examine the various zones. This analysis method is very subjective, and the results are prone to changing based on the doctor examining the eye. In addition, the procedure is very discomforting for the infant and parents to be used as a screening technique. Therefore, it is thus very crucial to identify a biomarker that can be associated with the onset of ROP. The biomarker can be used to develop a non-invasive screening tool to screen infants who are at a higher risk of developing ROP without causing them any discomfort.

2.1.3 Pathogenesis of ROP

ROP is characterized by two phases of development. During the first phase, which takes place till 30-32 weeks of post menstrual age, the vessel growth in the retina is disrupted. Infants who are born at this phase have an incompletely vascularized retina. These preterm babies are

generally exposed to elevated oxygen levels in the incubator resulting in hyperoxia condition which downregulates the Vascular Endothelial Growth Factor (VEGF) and there is recession of growth vessels. The second phase of ROP is characterized by uncontrolled growth of the blood vessels or angiogenesis induced by hypoxia. When the infants are out of the incubator, they experience a relative hypoxia which stimulates growth factors like VEGF and erythropoietin that lead to uncontrolled blood vessel (vascular) growth in the vitreous leading to neovascularization (Chen, Stahl, Hellstrom, & Smith, 2011) (Figure 36) .

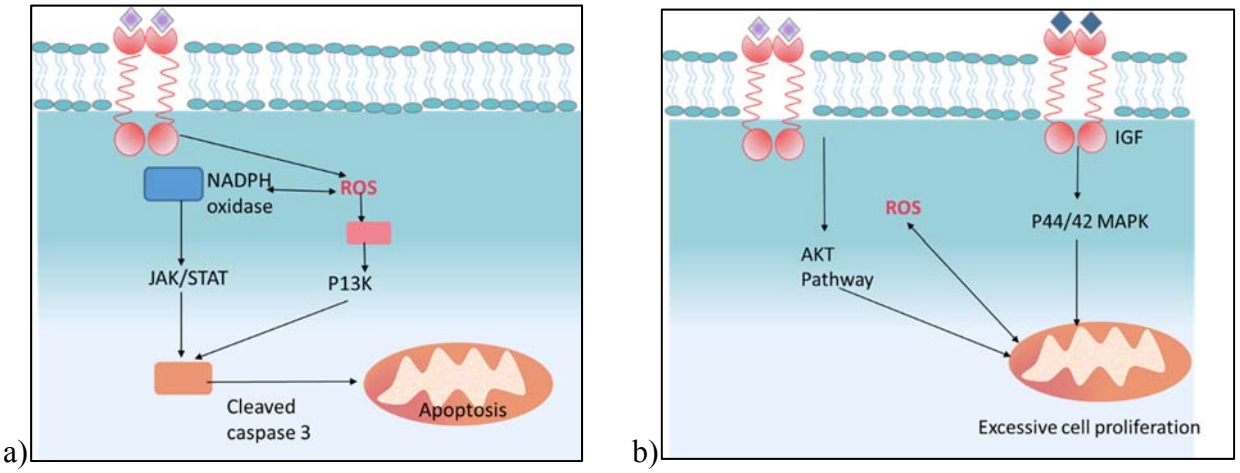

Figure 36: a) Molecular pathways in Phase 1 ROP b) Pathways in Phase 2 ROP

Both disrupted blood vessel growth and uncontrolled angiogenesis lead to an increased production of ROS which causes oxidative stress in the cells. Oxidative damage disrupts biomolecules like proteins and DNA (Ates et al, 2009). ROS causes the DNA strand breaks and base modifications. The most common base modification is the oxidation of the guanine base in the DNA forming 8-hydroxy 2-deoxyguanosine (8-OHdG) (Ates et al, 2009).

2.1.4 Hypothesis and Solution

8-OHdG is formed by oxidation of guanine base in DNA as a result of enzymatic cleavage. The amount of urinary 8-OHdG reflects the amount of oxidative damage occurring in the body (Hinokio et al, 2004). We hypothesized that 8-OHDG can be considered as a useful biomarker for determining the level of oxidative stress caused due to retinal damage. These oxidized DNA products are water soluble and are excreted through the urine without undergoing further metabolism. Our hypothesis was that 8-OHdG will be excreted in urine and can be identified easily. We hypothesized that levels of 8-OHDG in patients with ROP will be higher than in patients without ROP.

The most commonly used analytical techniques for the detection for 8-OHdG are high-performance liquid chromatography-electrochemical detection (HPLC-ED), HPLC tandem mass spectrometry, gas chromatography-mass spectrophotometry (GC-MS), Capillary Electrophoresis with electrochemical detection (CE-ECD). These techniques have good sensitivity and accuracy; however, these are lab based techniques requiring expensive instrumentation and trained personnel. Enzyme Linked Immunoassay (ELISA) is also used for the colorimetric detection of 8-OHdG. 8-OHdG is a small molecule, hence the major challenge is to immobilize it for the purposes of capture and detection. The most common method for detection of 8-OHdG is by conjugating it with a heavy protein like BSA (Bovine Serum Albumin) and conducting a competitive ELISA for the detection and analysis (Wu et al, 2004). Albeit being less complex than HPLC techniques, it is still a lab based and time consuming and hence is not suitable for bed side or in-house detection of 8-OHdG. For these purposes, there is a need for the development of a point-of-care testing device which is portable and has faster readout times. We

have developed a Lateral Flow Immunoassay (LFIA), for simple and easy detection of the marker.(Hinokio et al., 2002) (X. Zhu, Shah, Stoff, Liu, & Li, 2014).

2.1.5 Gold Nanoparticles for LFIA

Gold nanoparticles exhibit unique optical and surface properties which have been widely utilized in biological applications like determination of tumor biomarkers, toxins etc. (Wu et al, 2015). The advantages of gold nanoparticles are that they are highly biocompatible, easily modified for surface functionalization and have low toxicity (Wu et al, 2015). Another important property of gold nanoparticles is the induction of Localized surface Plasmon resonance (LSPR) on incidence of light. The nanoparticles absorb and scatter light with greater intensity than their bulk material counterparts (Anker et al, 2008). This property enables the gold nanoparticles to be used as colorimetric labels for immunoassays and other biological applications (Anker et al, 2015) (Figure 38). In this project, gold nanoparticles were used as colorimetric substrates for detection of 8-OHdG in paper strip based Lateral Flow Immunoassay. The gold nanoparticles were functionalized with anti-8-OHdG antibody using electrostatic binding (Figure 37).

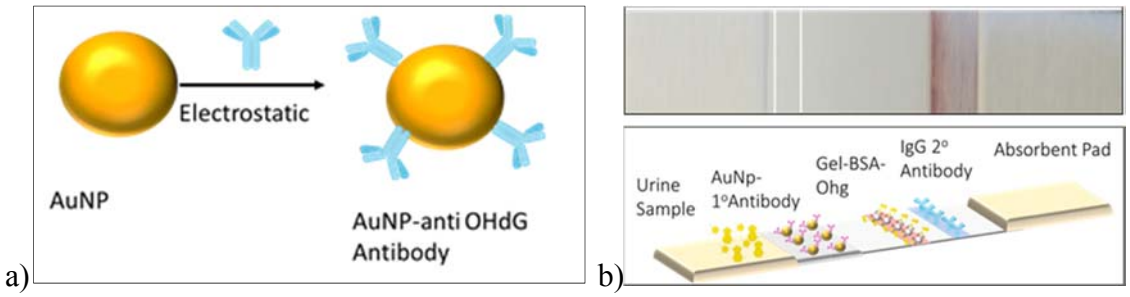

Figure 37 a) Schematic of Gold nanoparticle conjugated with anti-8-OHdG antibody b) Schematic of LFIA paper strip

2.1.6 Substrates of 8-OHdG for ELISA and LFIA

8-OHdG is a small molecule and its direct immobilization on any surface is challenging. 8-OHdG must be conjugated with a carrier protein such as BSA (Bovine serum albumin) for surface immobilization ((L. L. Wu, Chiou, Chang, & Wu, 2004; X. Zhu et al., 2014). We have conjugated BSA with 8-OHdG by a periodate oxidation method(Xuena Zhu, Hondroulis, Liu, & Li, 2013) (Figure 39). The diol groups of the ribose moiety are oxidized to dialdehyde which is then conjugated with the amino groups of the amino acid by carbodiimide bond. Competitive ELISA was performed to on a 96 well plate to assess the binding affinity of the BSA-OHG substrates to the anti-OHdG antibody (Figure 38 a). From the initial ELISA experiments it was observed that BSA-OHG was amenable to being washed away from the plate after several washing steps. A library of nanoparticles were prepared including gelatin nanoparticle conjugated with BSA-OHG, Latex beads-BSA-OHG conjugates and magnetic nanoparticle-BSA-OHG conjugates. Initial ELISA studies were conducted with each of the conjugates and it was observed that gelatin nanoparticle conjugated with the BSA-OHG was least susceptible to washing away from the plates (Figure 38 b). Gelatin nanoparticles formed by two step desolvation method with acetone precipitation and crosslinked with glutaraldehyde are very robust and versatile nanoparticles that are used for several applications (Naidu & Paulson, 2011). Gelatin nanoparticles can be covalently conjugated with antibodies for detection and analysis. (Figure 39 a) ELISA studies showed that these nanoparticles are more adherent to the surface as compared to the other conjugates Figure 39 b). We chose the Gel-BSA-OHG as the robust substrate for all the consecutive ELISA and LFIA experiments for optimization and clinical studies.

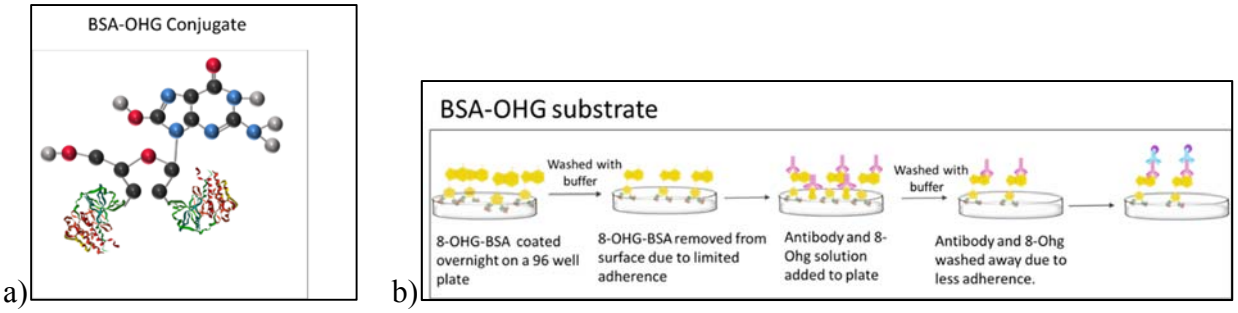

Figure 38 a) Schematic of BSA-OHG conjugate b)Competitive ELISA on a 96 well plate with BSA-OHG conjugate

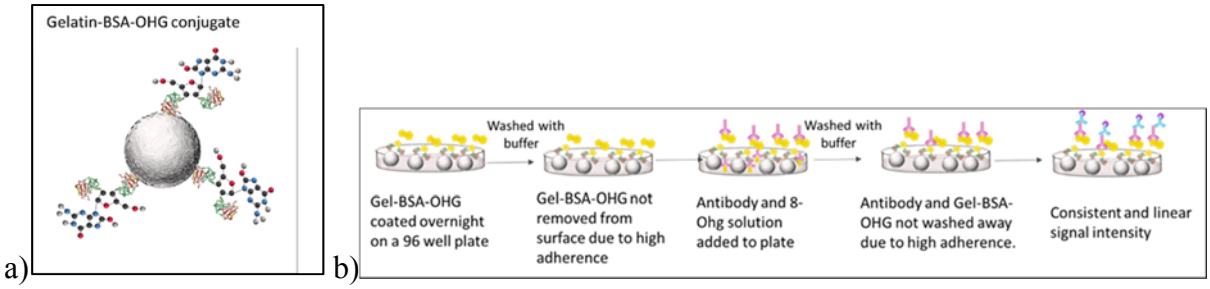

Figure 39 a) Schematic of Gel-BSA-OHGconjugate b) Competitive ELISA with Gel-BSA-OHG

We analyzed the samples using Competitive ELISA and Lateral Flow Immunoassay and foundthat both the assay results correlated well with the Fundus results. The results were correlated with the ROP status of the patients which were determined by physical examination.

2.2 Materials and Methods

2.2.1 Materials

$HAuCl_4$ (Hydrogen Tetraaurochlorate) was purchased from Acros Organics. Bovine Serum Albumin (BSA), Sodium Periodate, 1-Ethyl-3-(3-dimethylaminopropyl) carbodiimide(EDC) and Bicinchonic assay kit were purchased from Sigma Aldrich. Gelatin, Sodium citrate trihydrate, Hydroxy sulfo succinimide (Sulfo-NHS) were purchased from Thermo Fisher Scientific. OHG

and 8-OHdG were purchased from Cayman Chemicals. Anti-8-OHdG [15A3] antibody was purchased from AbCam. Anti-Mouse IgG-HRP was purchased from Jackson Laboratories. Polyethylene Glycol-NHS (PEG-NHS) and succinimidyl PEG-NHS were purchased from Nanocs. TMB substrate was purchased from BioRad. The Nitocellulose membrane, the sample pad and the conjugate pad were purchased from Millipore. Artificial Urine was purchased from QuikFix.

2.2.2 Instruments

Core nanoparticle size measurements were performed using Joel TEM. Hydrodynamic size and zeta potential was measured using a Malvern Zetasaizer Nano-ZS. Centrifugation was performed on a 5424 Eppendorf and refrigerated RC 6+ Sorvall centrifuge. pH was measured using a Seven Compact Mettler Toledo pH meter equipped with an InLab Micro electrode. Fluorescence imaging, fluorescence assays and UV-vis absorption assays were performed on a Cytation 5 Cell imaging multi-mode reader. Gel electrophoresis was performed on a Biorad Mini-Protean Tetra system and blots were transferred using a Genscript e-blot transfer system. Western blot imaging and acquisition was performed using Image Lab ver 5.2.1 software on a ChemiDoc XRS system from Biorad. Band densitometry analysis was performed on Image Studio ver 5.2. Solvent extraction was performed on a Büchi Rotovapor R-124 attached to a water bath and watercoo led distillation column. SQUID measurements were performed on a Quantum Design MPMS 3 Magnetometer. The antibodes and substrate were coated on the paper strip using a Camag Linomat 5 automated dispenser.

2.2.3 Synthesis of BSA-OHG Conjugates

BSA-OHG conjugate was synthesized based on a previous publication with some modifications (L. L. Wu et al., 2004; Xuena Zhu et al., 2013).

BSA solution was prepared dissolving 12.5mg BSA in 1 ml of 50mg/ml K_2Co_3. 8-OHG (0.5 mg) was dissolved in 100 µl of periodate and mixed in dark conditions for 1 hour in a thermomixer at RT. 200µl of BSA was added and mixing was continued for 1 hour in dark followed by addition of 200µl of $NaBH_4$ (24mg/ml). The solution mixed overnight at 4^oC and passed through 10kDa filter. Gelatin nanoparticles were synthesized using a two-step desolvation process as described in the previous section. BSA-OHG was covalently conjugated with Gelatin nanoparticles using EDS/NHS activation method. 1 ml Gelatin nanoparticles (6mg/ml) were centrifuged at 15,000g for 12 minutes. The supernatant was discarded and to the pellet 2.4 mg EDC in 3.6 mg of NHS were added in 40µl. The volume of the solution was made to 1ml and incubated in thermomixer at 24^oC for 4 hours. The activated nanoparticles were washed once to remove excess EDC and NHS. 36 µl of BSA-OHG in 1 ml 1X PBS was added to the nanoparticles and mixed overnight. The BSA-OHG conjugated nanoparticles were washed twice with 1X PBS. The final pellet was dissolved in 1X PBS.

2.2.4 Synthesis of Gold Nanoparticle Conjugates

The AuNPs were synthesized by a modified citrate reduction method (Afrasiabi et al., 2010). Briefly, 50 ml of 0.01% HAuCl4 solution was heated to a boil followed by a rapid addition of trisodium citrate solution (1 mL, 1%) under vigorous stirring. After the color changed from yellow to red, the solution was continued to boil for another 10 min, then stirred without heating till the solution reached the room temperature. The AuNPs solution was concentrated 10X using a 70KD

membrane filter. The pH of the AuNPs solution was adjusted to 8.5 ~ 9.0 with K_2CO_3 (0.1 M). The optimum concentration of antibody necessary for conjugating the AuNPs to stability is determined by a salt based aggregation test. The electrostatically stabilized AuNPs aggregate in the presence of salt till the surface is stabilized by enough protein. Briefly, 50 µl of antibody of decreasing concentrations (1, 0.5, 0.25, 0.125, 0.0625, 0.03125 mg/ml) were taken in separate tubes. They are incubated with 750 ul of 10X AuNPs for 20 mins followed by the addition of 0.5 ml of 10% NaCl to all of them.

2.2.5 Competitive ELISA

A 96 well plate was coated with 100µl of GEL-BSA-OHG at different dilutions (1:100, 1:1000, 1:10000) and incubated overnight at 4ºC. The wells were washed with 100µl ELISA wash buffer followed by blocking with 200µl Blocking buffer (2% Milk solution) for 30 minutes. The wells were then washed with ELISA wash buffer and 50ul anti 8-OHdG antibody solution (1ug/ml) with 50µl 8-OHdG solution at different concentrations (0.1 mg/ml, 0.01 mg/ml) was added to the wells and incubated for 2 hours. Excess of unbound antibody was removed by washing with ELISA wash buffer. 50µl of Anti-mouse IgG- HRP was then added to the wells and incubated for 30 minutes. The excess antibodies were washed away and 50µl of the colorimetric substrate (TMB) was added followed by 50µl of stop solution (0.1M HCl). The colorimetric intensity was analyzed by measuring their UV absorbance at 450nm.

2.2.5 Lateral Flow Immunoassay

We observed that the color of AuNP turned blackish blue and the LSPR peak underwent blue shift to all the concentrations below 0.5 mg/ml. The optimal concentration of AuNP at which no aggregation is seen was chosen for antibody conjugation. Thus, 0.5mg/ml is the optimum

concentration of the antibody. To ensure maximum loading of the antibody, the 10X AuNPs (900 µl) were incubated with 50 µl of 1mg/ml purified anti-8-OHdG Ab at 750 rpm, RT for 1 hour. The conjugate was then incubated with BSA (10%) in sodium borate (20 mM) for a final concentration of 1% for another 20 min. Then the mixture was centrifuged for 15 min at 7000 rcf. The faint pink supernatant of unbound antibodies was discarded, and the pellet was resuspended in BSA/PBS (900 µl, 1%) to further wash away any unbound antibodies. Following the same centrifugation step, the supernatant was removed, and the soft sediment of conjugates was resuspended in conjugate pad buffer (900 µl).

The conjugate pad, sample pad and absorbent pad were assembled with 1-2 mm overlap on a 6 cm x 30.1 cm laminated card with Hi-Flow Plus lateral flow membrane with a 0.19mm backing adhered to the surface of the card (HF180MC100 Millipore). Once assembled, Gel-BSA-8OHG (1mg/ml) and goat anti-mouse IgG (1mg/ml) were dispensed on the nitrocellulose membrane (2µl/cm) using a Linomat 5 dispenser as test line and control line respectively. The assembly was then dried for 1 hour at 37 °C, cut into 4mm wide strips using a strip cutter and the strips were stored in the desiccator at RT. The 4mm wide strips were immersed in 80 ml of standards or urine samples in transparent plastic vials. The development of color was seen within 10 min. To maximize the color intensity and to maintain uniformity, the photographs of the strips were taken 90 min after their dip in the standards/samples. The intensity of the color was quantified using ImageJ software.

2.2.6 Analysis of Clinical samples

The clinical study was approved by the review board in University of Missouri, Columbia (IRB No 2004129). Urine samples were collected from collected from preterm infants admitted in the Neonatal Intensive Care Unit (NICU) of the Women's and Children Hospital at University of

Missouri, Columbia. The consent for collecting the samples were taken from the parents of the babies. The urine was collected through cotton balls inserted in the diapers of the babies. Samples were collected at 24 hours and 72 hours after the birth and then once every week till the baby was discharged from the NICU. The ROP status of the babies who qualified for the ROP examination or screening was determined after a physical examination of the dilated eye of the baby by an ophthalmologist. The qualifying or inclusion criteria for ROP screening of the patients was that they are born before 32 weeks of gestation and/or weigh less than 1500 grams. 8-OHdG levels of the samples were analyzed using traditional competitive ELISA with Gel-BSA-OHG substrate and with Lateral Flow Immunoassay based paper assay with Gold nanoparticle conjugated with anti-8-OHdG antibody as the colorimetric substrate. Student t-test was conducted on the samples using Minitab.

80µl of 8-OHdG solutions of varying concentrations (0, 5, 10, 20, 40, 50 60, 70 ng/ml) were added to a quartz cuvette and the paper strip was dipped in the solutions. The color development on the test line was observed for the strips within 5 minutes and the test and control lines images were captured using a camera. The images were analyzed using ImageJ software and a standard curve was obtained by plotting the ratio of the intensity of test line/ nitrocellulose membrane against concentration (ng/ml) of 8-OHDG. Urine samples were centrifuged at 3000g. 80ul of the samples were added to a quartz cuvette. The color development at the test and control line was captured using a smartphone after 1 hour. The intensity of the test line of the urine samples was analyzed using ImageJ and the 8-OHdG values were calculated based on the standard curve of known 8-OHdG values.

2.3 Results and Discussion

2.3.1 Synthesis and Characterization of Gel-BSA-OHG conjugate

8-OHDG is a small molecule and cannot be immobilized on a substrate or well plate on its own. The most common method of immobilization is by conjugating OHG to a carrier protein like Bovine Serum Albumin (BSA). OHG was conjugated to BSA using periodate conjugation method where the diol groups of ribose moiety of OHG were oxidized to aldehyde by periodate and were conjugated to the lysine residues of the BSA. The conjugation of BSA to OHG was ascertained by UV-Vis absorption of the BSA-OHG conjugate. The UV-vis absorption spectrum of the BSA-OHG was broader compared to that of the unconjugated BSA (Figure 40 a). The amount of OHdG conjugated to BSA was estimated using UV-Vis absorption. The conjugation efficiency of the OHG to BSA was estimated to be around 33%. Gelatin nanoparticles were conjugated to BSA-OHG using EDC/NHS activation. The core and hydrodynamic size of the nanoparticles was around 250 nm (Figure 40 b). The zeta potential of the Gel-BSA-OHG nanoparticle was 18 mV.

a) 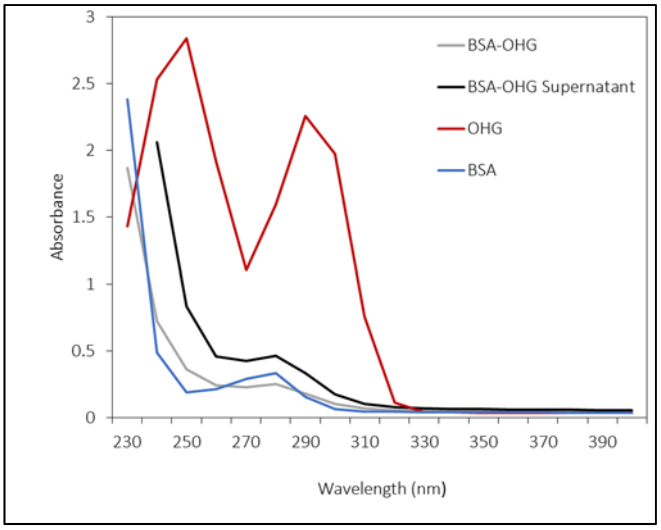

b) 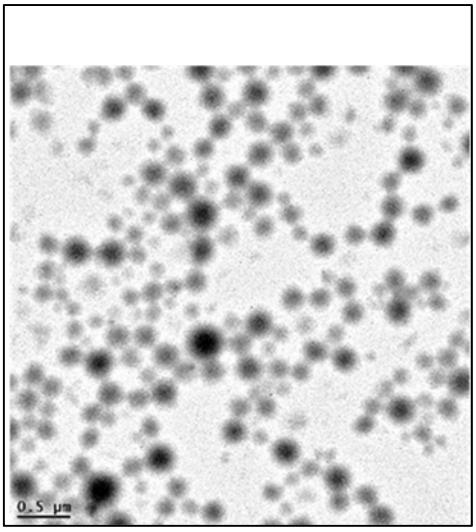

Figure 40 a) UV-vis absorbance of OHG and BSA-OHG conjugate b) TEM image of Gel-BSA-OHG nanoparticles

2.3.2 Synthesis and characterization of Gold Nanoparticle conjugates

Gold nanoparticles were synthesized by reduction of gold ions using sodium citrate as a reducing as well as stabilizing agent. UV-vis absorbance was recorded to confirm the formation of gold nanoparticles which exhibit an absorbance peak at 520 nm (Afrasiabi et al., 2010)(Figure 41 b). Size and zeta potential measurements were performed. The hydrodynamic size was found to be 20 nm, core size of 10 nm using TEM (Figure 41 a) and zeta potential is -19 mV.

a) 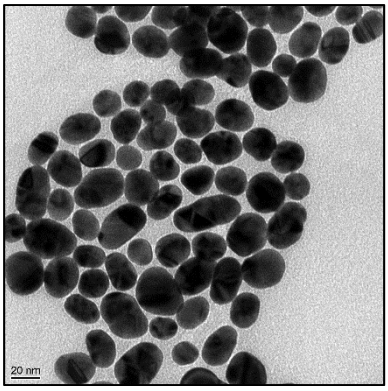

b) 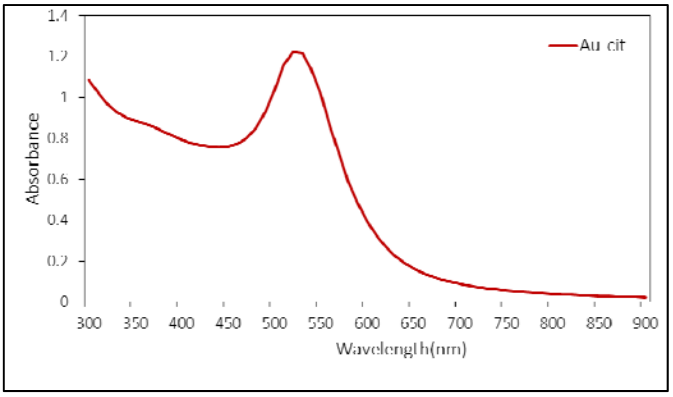

Figure 41 a) TEM image of Citrate Gold Np b) UV-vis absorbance of Citrate Gold nanoparticle

The gold nanoparticles were concentrated to 10X and the pH adjusted to 8. The anti-8 OHdG antibody was bound to the negatively charged gold nanoparticles via electrostatic binding. The conjugation was followed by blocking with BSA buffer to block the free surfaces of the gold antibody conjugate. The optimal amount of antibody to be conjugated with the gold nanoparticle by aggregation studies with NaCl. Different concentrations of antibody were added to the gold nanoparticle in 10% NaCl solution. At an optimal antibody concentration, no color change would be observed in the gold nanoparticle solution (L. Wu, Pu, Liu, Zhao, & Shu, 2015). We observed that when 8µl of anti 8-OhdG antibody (1 mg/ml) was added to AuNp, the nanoparticles did not exhibit any color change. (Figure 42), suggesting that 8µg of anti-8-OHdG antibody was the optimal amount of antibody to be added. Hence, for all future experiments, 8ul of anti-8-OHdG antibody was added to the gold nanoparticle solutions.

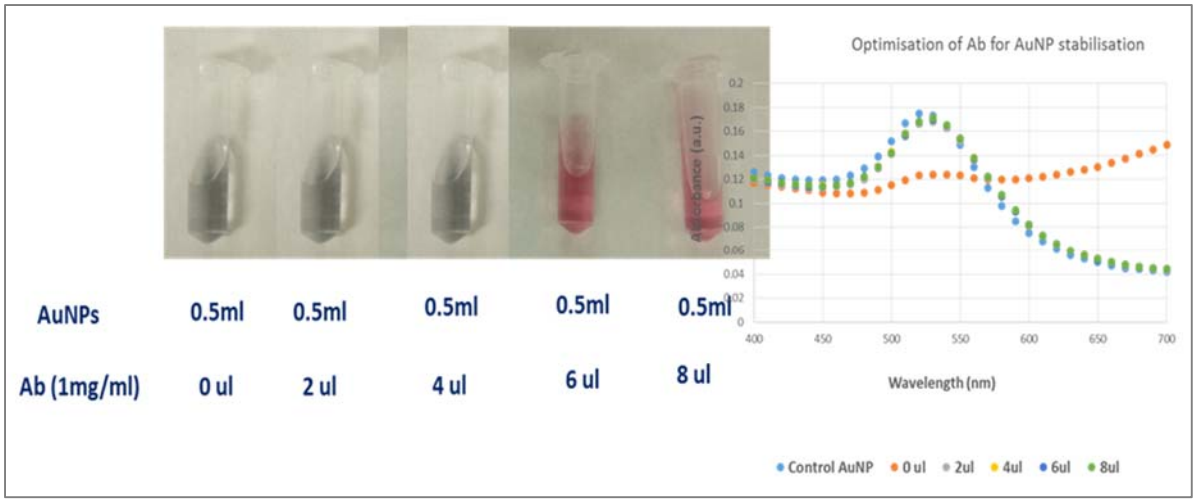

Figure 42 UV-Vis absorbance graph of antibody conjugated citrate AuNP

2.3.3. Competitive ELISA for Detection of 8-OHDG

Competitive ELISA was performed to evaluate the efficiency of Gel-BSA-OHG to detect OHDG in varying concentrations. Gel-BSA-OHG was coated on the plate with varying concentrations on a 96 well plate followed by incubation with anti OHDG antibody (1ug/ml) with varying concentrations of 8-OHdG. Addition of Secondary IgG with HRP enzyme and its subsequent reaction with the TMB substrate established the varying color intensity of the wells depending on the concentration of the Gel-BSA-OHG and OHDG (Figure 43). The signal intensity decreased with increasing 8-OHdG concentrations.

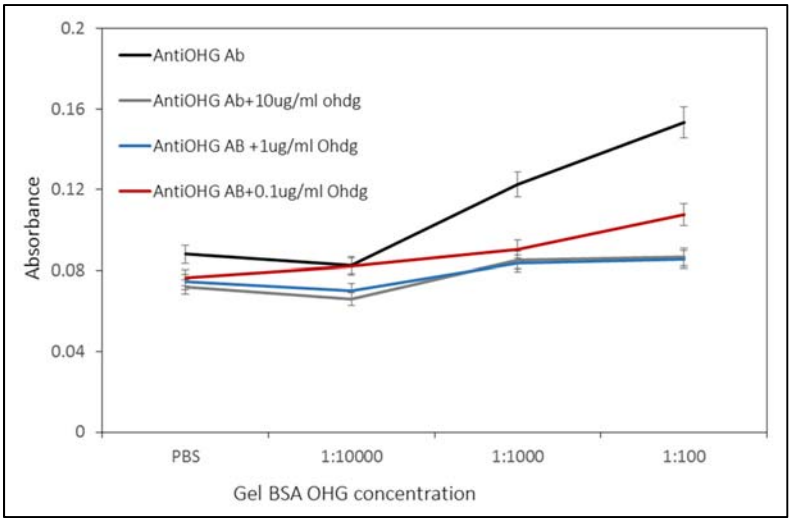

Figure 43 Competitive ELISA with anti-OHdG antibody with varying concentrations of 8-OHdG

From the ELISA results, we established that Gel-BSA-OHG can be used as a substrate for the detection of OHDG at a concentration of 1 mg/ml. We concluded that GEL-BSA-OHG at a concentration of 1 μg/ml could be used a robust substrate for the competitive ELISA (Figure 44).

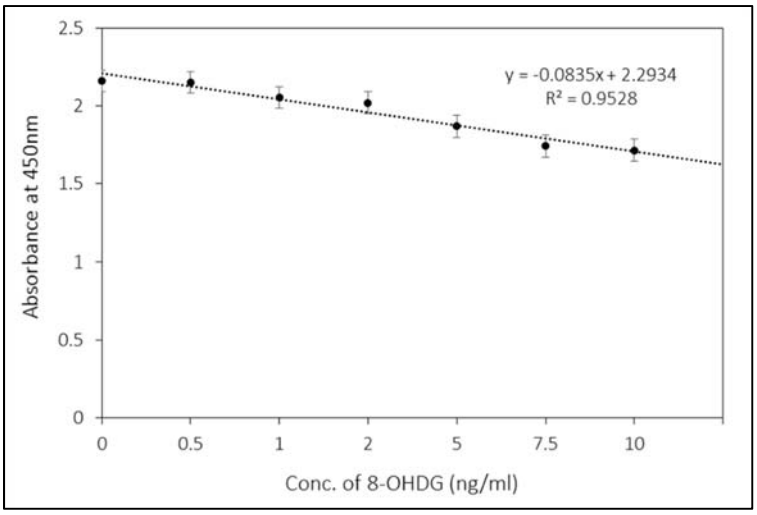

Figure 44 Standard curve of Competitive ELISA with anti-8-OHdG antibody with varying concentrations of 8-OHdG

The human urine is composed of several components like urea, sodium, potassium, creatinine and other dissolved ions. The Gel-BSA-OHG and antibody-nanoparticle conjugate should not have any interference with the other components of the urine and should be able to detect only the amount of OHDG present in the sample. Artificial urine, which has the similar composition as human urine, was purchased from Quikfix. Competitive ELISA was performed on a 96 well plate with Gel-BSA-OHG as the substrate and varying concentrations of OHDG was added to the artificial urine sample (AU). The ELISA results demonstrated that the colorimetric intensity decreased with increasing OHDG concentrations, validating the utility of the substrate for detecting 8-OHdG in a human urine sample. We observed no noticeable difference in the standard curves obtained with artificial urine (AU) (Figure 45), suggesting that the other components of urine do not interfere with the detection of 8-OHdG with Gel-BSA-OHG substrate and anti-8OHdG antibody.

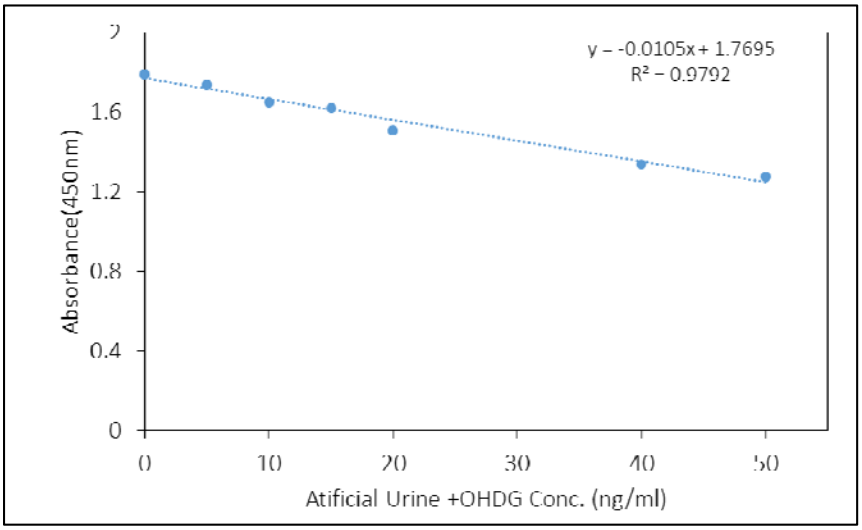

Figure 45 Interference studies with artificial urine in Competitive ELISA

2.3.4 Lateral Flow Immunoassay: Testing of 8-OHdG in paper assay

The paper strip assay was assembled on a nitrocellulose membrane. The conjugate pad was coated with Au-antiOHdG conjugate. The test pad was coated with Gel-BSA-OHG substrate and the control pad was coated with anti-mouse IgG (secondary antibody). The paper strip which was 3 mm wide and 6 cm long was used as a dip sensor. The paper strip was dipped in OHDG solution of varying concentrations and the colorimetric intensity of the test line was captured using a smartphone. The images obtained were analyzed using ImageJ software. Different smartphones and smart devices were used to capture the images like Samsung S6, Lumia and Cool pad. The intensity of the test line decreased with increasing concentration of the 8-OHdG concentrations. The intensity of the test lines was normalized with the background intensity of the nitrocellulose membrane for all the images. The color of the test line started to appear within 1 hour of the initiation of the experiment. A test was conducted to confirm that the strip does not react with other components of the human urine. The strips were dipped in artificial urine added with varying concentration of 8-OHdG and the intensity of the test line was captured through a smartphone camera and the images were analyzed through ImageJ software. The strips did not seem to interfere with any of the other components of the artificial urine and exhibited a decreasing intensity with increasing 8-OHdG concentration (Figure 46).

a) 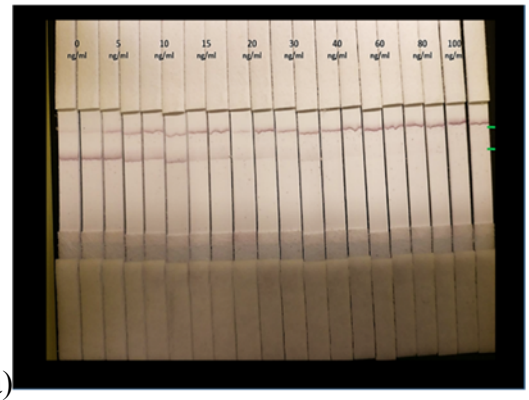

b) 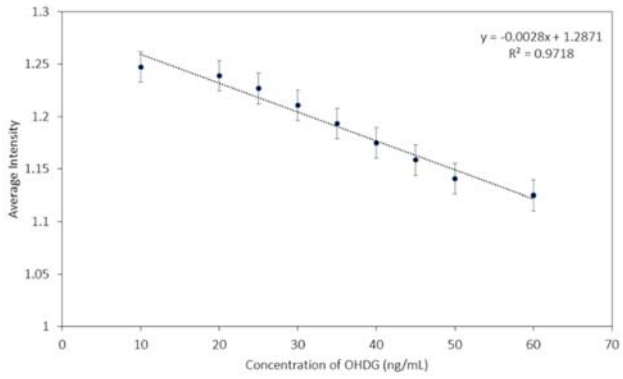

Figure 46 a) Colorimetric intensities of control line with increasing conc. Of 8-OHdG b) Standard curve of the intensities

2.3.5 Analysis of Urine samples using Competitive ELISA and LFIA

Urine samples were collected from infants admitted in NICU with the parents' consent using a cotton ball. The inclusion criteria was that the babies should be born before 32 weeks or their weight is less than 1500g. Samples were collected at different time points and were stored in -20^{o} C till they were analyzed. A total of 209 samples from 32 patients were analyzed. The 8-OHdG level in the urine samples was analyzed using 96 well Competitive ELISA as well as lateral flow based paper strip assay. Standard curves with known 8-OHdG concentrations were used as a controls . The results were correlated with the ROP status of the patients as examined by the ophthalmologist. The 8-OHdG levels in the two different methods were also correlated. A student t-test was performed to compare the differences between the values of OHDG of patients with and without ROP ($p<0.01$). The ROP status was divided in three groups: Stage 0, Stage 1 and Stage 3. The average 8-OHdG values of the patients as recorded from both ELISA and LFIA in all the three categories were calculated. The average values of the 8-OHdG of patients

with Stage 1 and Stage 3 ROP was significantly higher than those with Stage 0 or No ROP. (Figure 47).

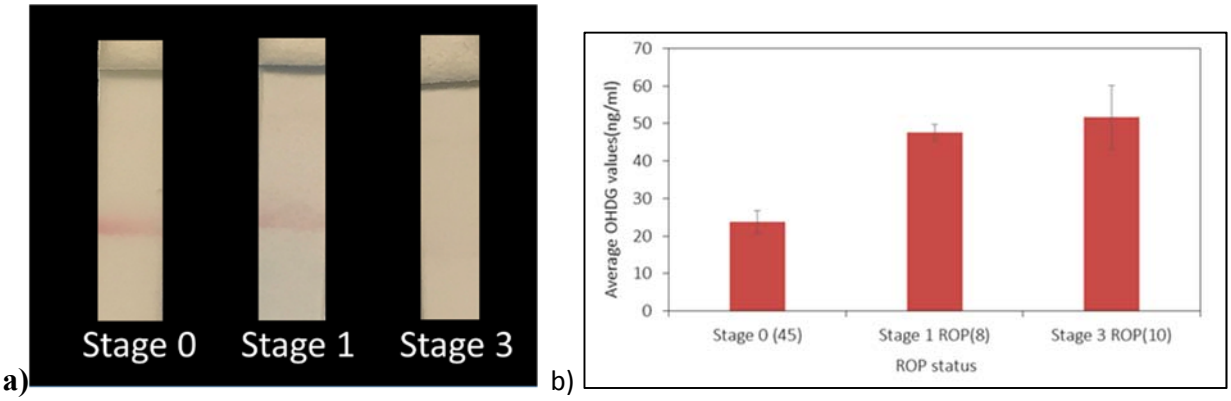

Figure 47 a) Colorimetric Intensity of test line for urine samples with Stage 0, Stage 1 and Stage 3 ROP respectively b) Average 8-OHdG values for patients with Stage 0, Stage 1 and Stage 3 ROP respectively

The amount of 8-OHdG in the urine samples was analyzed using competitive ELISA method as well as LFIA method. The 8-OHdG values were plotted for patients with ROP and patients with no ROP. The values obtained from competitive ELISA method suggested that 8-OHdG values were higher in patients with ROP as compared to patients with no ROP. However, there were a five outliers observed for stage 0 ROP values .The distribution plot of 8-OHdG values showed that the patients with Stage1 or Stage 3 ROP had 8-OHdG values ranging from 35 ng/ml to 100 ng/, while the value was less than 35 ng/ml for patients with Stage 0 ROP ml (Figure 48 a). Similar results were observed for 8-OHdG values obtained with LFIA (Figure 48 b). However, the number of outliers for Stage0 ROP was 2 for LFIA method.

a) 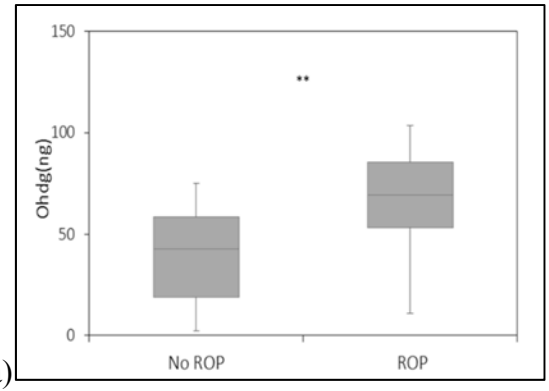

b) 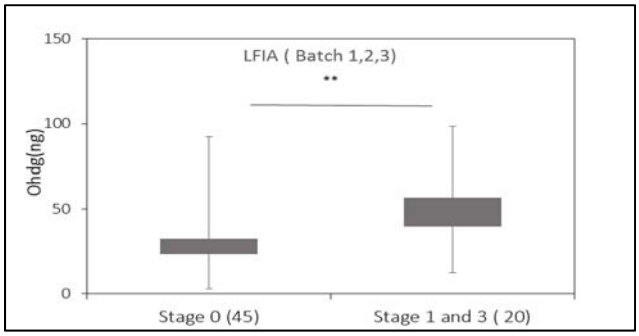

Figure 48 a) Distribution of 8-OHdG values for patients with and without ROP as analyzed by traditional ELISA
b) Distribution of 8-OHdG values for patients with and without ROP as analyzed by LFIA paper assay

8-OHdG levels of all the time dependent samples for each of the patients were plotted (Figure 49). Some patients developed ROP over the course of time and the values of the 8-OHdG for the time points correlated with the ROP status in most of the cases. It was observed that the patients who were diagnosed with ROP from the beginning presented a higher 8-OHdG levels than patients who developed ROP at a later stage. There were 5 cases where the 8-OHdG levels of the patients were high even though they were not diagnosed with ROP. Since, 8-OHdG is an oxidative stress marker, there might have been some other complications that might have caused the spike in the 8-OHdG levels. However, the average 8-OHdG levels of patients who had consistent or had developed ROP was higher than that of the patients without ROP. (Figure 50)

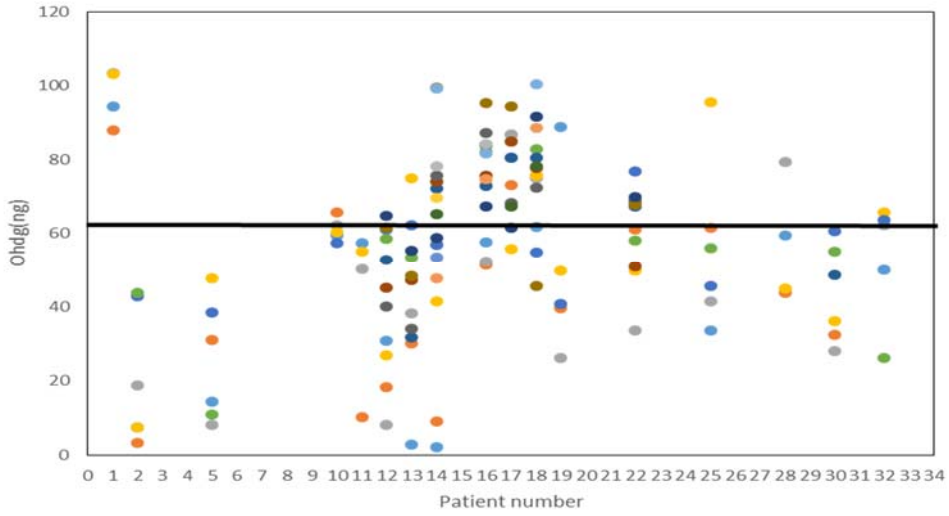

Figure 49 8-OHdG values of each sample of the patients in chronological order

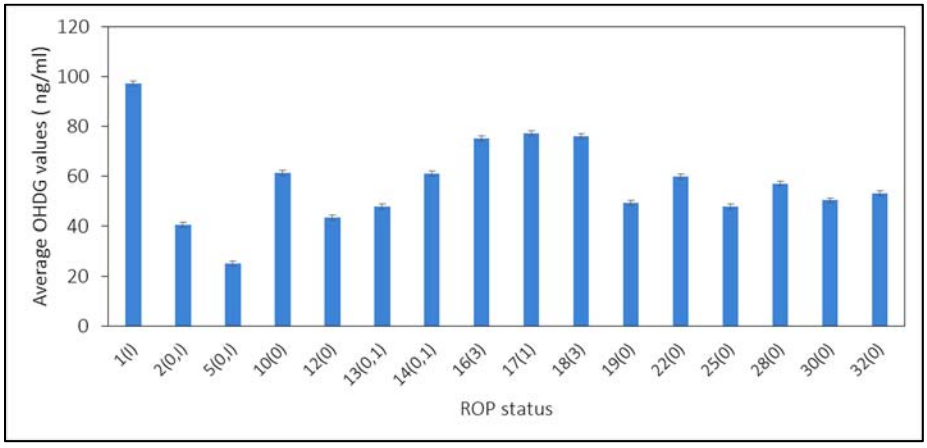

Figure 50 Average 8-OHdG values of each of the patients

2.4 Conclusion

From the ELISA results it is concluded, that levels of 8-OHdG can be correlated with onset of ROP. We did not notice a significant difference in the average values of 8-OHdG for patients with Stage 1 and Stage 3 ROP. However, there was a significant difference between the average 8-OHdG values of patients with Stage 0 (No) and Stage1 or Stage 3 ROP. This demonstrates that 8-OHdG is could serve as a valid marker to determine the onset of ROP and not necessary a tool to indicate the stage of ROP. The distribution values and average plots of the 8-OHdG values for both competitive assay and ELISA indicate that the patients with ROP have an average 8-OHdG value higher than 25-30ng/ml. Thus, for the purposes of a screening, the cutoff value for the patients would be 25ng/ml 8-OHdG. The patients who are at risk of developing ROP, i.e. patients who were born before 32 weeks or who are born with a weight less than 1500gm would be screened for ROP. Urine samples from these patients would collected at 24 hours after their birth and then at 72 hours and then once every week till they are discharged. If the 8-OHdG values of the patient remains under 30ng/ml, the patient is not at risk of developing ROP. However, if the value of 8-OHdG increases to 50ng/ml or above, the patient is at risk of developing ROP and the child would be checked for ROP by physical examination by an ophthalmologist. Since 8-OHdG is an oxidative stress marker, the levels of 8-OHdG can be affected by some other exacerbations like brochopulmonary dysplasia (BPD), hyperglycemia, number of days in incubator and number of days in the NICU. The status of BPD, hyperglycemia and number days in incubator and NICU data was collected from the clinics and the regression analysis was conducted to determine the influence of each of these factors in the values of 8-OHdG. It was observed that the status of BPD, hyperglycemia and number of days in the incubator did not have any effect on the outcome of the values of 8-OHdG. However, it was

noticed that there was a correlation between 8-OHdG values and the number of weeks spent at the NICU. The 8-OHdG values were high for patients who had been in NICU for more than 8 weeks. Hence, for screening purposes, the screening should be limited to 8 weeks in the NICU. If the patient is in the NICU for a longer time, the 8-OHdG levels would be high and might not corroborate with ROP status of the patient. Future studies with a larger sample will be required to establish 8-OHdG as a robust biomarker for the screening of ROP.

References

Afrasiabi, Z., Shukla, R., Chanda, N., Bhaskaran, S., Upendran, A., Zambre, A., . . . Kannan, R. (2010). Nanoscale Sensor Design via <I>In Situ</I> Labeling of Gold Nanoparticles onto Protein Scaffolds. *Journal of Nanoscience and Nanotechnology, 10*(2), 719-725. doi:10.1166/jnn.2010.1906

Asano, M. K., & Dray, P. B. (2014). Retinopathy of prematurity. *Dis Mon, 60*(6), 282-291. doi:10.1016/j.disamonth.2014.03.009

Ates, O., Alp, H. H., Caner, I., Yildirim, A., Tastekin, A., Kocer, I., & Baykal, O. (2009). Oxidative DNA damage in retinopathy of prematurity. *Eur J Ophthalmol, 19*(1), 80-85.

Chen, J., & Smith, L. E. H. (2007). Retinopathy of prematurity. *Angiogenesis, 10*(2), 133-140. doi:10.1007/s10456-007-9066-0

Chen, J., Stahl, A., Hellstrom, A., & Smith, L. E. (2011). Current update on retinopathy of prematurity: screening and treatment. *Current Opinion in Pediatrics, 23*(2), 173-178. doi:10.1097/MOP.0b013e3283423f35

Hinokio, Y., Suzuki, S., Hirai, M., Suzuki, C., Suzuki, M., & Toyota, T. (2002). Urinary excretion of 8-oxo-7, 8-dihydro-2'-deoxyguanosine as a predictor of the development of diabetic nephropathy. *Diabetologia, 45*(6), 877-882. doi:10.1007/s00125-002-0831-8

Naidu, B. V. K., & Paulson, A. T. (2011). A new method for the preparation of gelatin nanoparticles: Encapsulation and drug release characteristics. *Journal of Applied Polymer Science, 121*(6), 3495-3500. doi:10.1002/app.34171

Wu, L., Pu, W., Liu, Y., Zhao, H., & Shu, W. (2015). Visual detection of 8-OHdG based on the aggregation of gold nanoparticles capped with the anti-8-OHdG antibody. *Analytical Methods, 7*(19), 8360-8365. doi:10.1039/c5ay01774b

Wu, L. L., Chiou, C. C., Chang, P. Y., & Wu, J. T. (2004). Urinary 8-OHdG: a marker of oxidative stress to DNA and a risk factor for cancer, atherosclerosis and diabetics. *Clin Chim Acta, 339*(1-2), 1-9.

Zhu, X., Hondroulis, E., Liu, W., & Li, C.-z. (2013). Biosensing Approaches for Rapid Genotoxicity and Cytotoxicity Assays upon Nanomaterial Exposure. *Small, 9*(9-10), 1821-1830. doi:10.1002/smll.201201593

Zhu, X., Shah, P., Stoff, S., Liu, H., & Li, C. Z. (2014). A paper electrode integrated lateral flow immunosensor for quantitative analysis of oxidative stress induced DNA damage. *Analyst, 139*(11), 2850-2857. doi:10.1039/c4an00313f

.

CHAPTER 3

NANOPARTICLE BASED ASSAY FOR SCREENING DIABETIC RETINOPATHY

3.1 Introduction

3.1.1 Diabetic Retinopathy: Background

Diabetes Mellitus (DM) is one of the most endemic diseases around the globe. It is estimated that the number of DM cases will increase from 171 million in 2006 to 366 million by 2030 (WHO, Case reports on Diabetes, 2012). In spite of the advances in medicine, the rapid escalation of the DM cases over the past few decades can be attributed to sedentary lifestyle and increased obesity amongst adults and children. Diabetes Mellitus (DM) is a metabolic disease which impairs the body's ability to breakdown glucose, resulting in accumulation of glucose in the blood stream(Madsen-Bouterse & Kowluru, 2008).

The accumulation of glucose in the system results from either the reduction in insulin production (Type 1 diabetes) or the body's inability to breakdown insulin (Type II diabetes). The excess glucose in the circulatory system gradually starts to affect different vasculatures of the body, leading to micro and macro vascular complications (R. A. Kowluru, Kowluru, Mishra, & Kumar, 2015). Macro vascular complications include cardiovascular disease while micro vascular complications include, nephropathy, neuropathy and Diabetic Retinopathy (Eshaq, Aldalati, Alexander, & Harris, 2017).

Diabetic Retinopathy (DR) is a slow progressing disease which affects the retina leading to impaired vision or complete vision loss. DR is the primary cause of acquired blindness among

adults with Diabetes Mellitus (DM). According to the National Eye Institute the incidence of DR is projected to double from 7.7 million in 2010 to 14.6 million in 2050 in the USA. The number of DR and vision threatening DR cases is estimated to rise to 191 million and 56.3 million respectively by 2030. DR is a significant health problem causing huge economic burden to developing as well as developed counties. The main challenge faced by the medical community is that DR is asymptomatic till it has progressed to an advanced stage. Hence, early screening of DR for patients with diabetes will allow prevention of blindness or severe retinal damage.

3.1.2 Diagnosis of DR and Challenges

The current gold standards for diagnosing DR are Fundus Photography (with a Fundus camera based on indirect Ophthalmoscope) and Fluorescein Angiography. Diabetic Retinopathy is asymptomatic for several years. The first visible symptoms of DR are the appearance of micro aneurysms in the retina (small area of blood protruding from the vein) and internal hemorrhages (ruptured micro aneurysms) which can be detected by Fundus photography (Cunha-Vaz & World, 2011). Other symptoms include capillary occlusion and hard exudates (extracellular accumulation of lipoproteins), which are detectable by Fluorescein angiography.

DR can be classified as Non-Proliferative and Proliferative DR. Non-Proliferative DR (NPDR), which is a less severe manifestation of DR, can be further be classified as mild, moderate and severe (Cunha-Vaz, 2011). Mild NPDR is characterized by sparsely populated micro aneurysms, while Moderate NPDR is characterized by an increase in the number of hemorrhages, hard exudates and retinal arterioles(Pickup & Williams, 1994). Severe retinopathy follows as the number of aneurysms increase further (Figure 51). Proliferative DR involves the formation of new blood vessels arising from the disc or retinal periphery which might cause retinal detachment and blindness (Pickup & Williams, 1994).

The presentation of these symptoms imply that the retinal cells were subjected to oxidative damage due to hyperglycemia over several years. The damage is often irreversible and leads to increased health care cost for the patients. Regular screening and checkup might help manage the symptoms and lead to better treatment options. However, patients from lower economic backgrounds might find it burdensome to go through regular DR screening checkups and hence might miss the initial stages of DR leading to an increased risk of blindness or severe retinal damage. Currently, there is no portable and easy diagnostic procedure that can detect the onset of DR at an earlier stage.

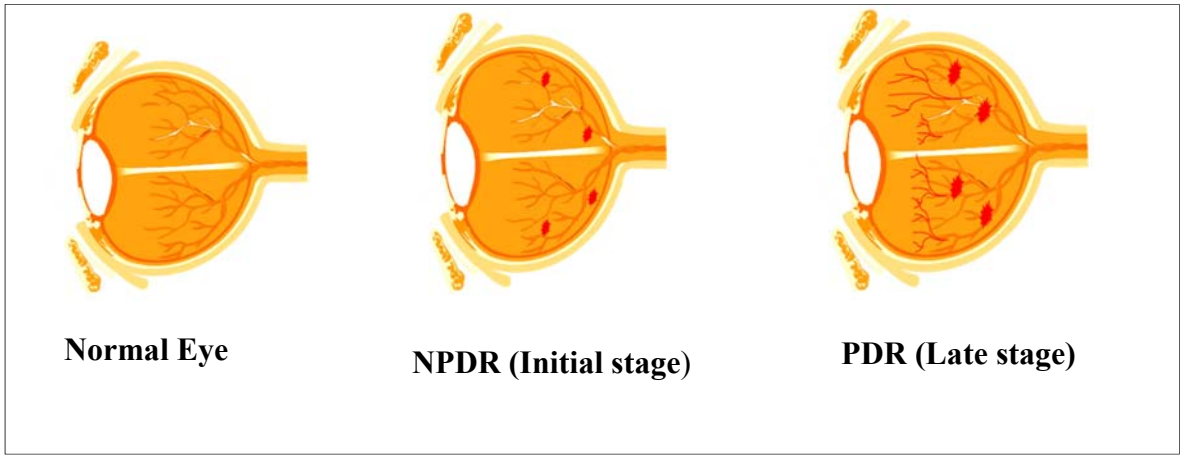

Figure 51 Schematic of the Eye in different stages of Diabetic Retinopathy

3.1.3 Clinical need

It is crucial to develop an in-home and cost effective screening technique that would indicate the early onset of the DR. This will help control the progression of the disease and also reduce the medication cost. The ideal diagnostic technique would allow the detection of DR at an earlier stage (when the retinal blood-vessel damage starts to occur), using a suitable biomarker.

3.1.4 Pathogenesis of Diabetic Retinopathy (DR)

To identify a suitable biomarker for the screening of DR, it is important to understand the pathogenesis and the molecular pathways of DR in the retina. The retina is a complex structure of several types of cells which include the vascular (pericytes and endothelial cells), neurons (photoreceptors, second-order neurons and ganglion cells), macroglia (Muller cells and astrocytes), and the microglia (Forrester, 2002) (Figure 52 a, 52 b). Excess glucose in the circulatory system disrupts the metabolism pathways in the retina and the capillary cells (Lechner, O'Leary, & Stitt, 2017). Under hyperglycemic conditions, the neural cells and the Muller cells undergo increased apoptosis which leads to neuronal cell death (R. A. Kowluru et al., 2015). The endothelial and pericyte cell loss due to diabetes is another major contributing factor in the development of DR. The onset of DR is also characterized by increased permeability of the blood retinal barrier (Eshaq et al, 2017). In addition, it has been reported that DR leads the mitochondrial dysfunction in the retina and its capillary cells along with change in mitochondria morphology and membrane potential. This leads to elevated superoxide radicals and compromised oxygen consumption (Madsen-Bouterse & Kowluru, 2008). Understanding the biochemical pathways responsible for these changes is important to identify the biomarker which can be directly correlated with the onset of DR.

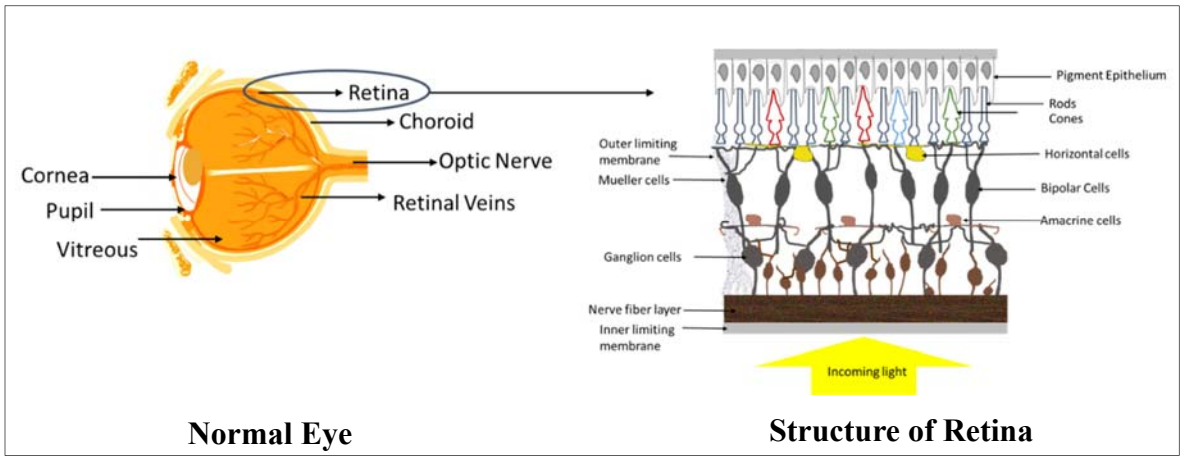

Figure 52 a) Schematic of Normal Eye b) Schematic of the different cells inside of Retina

Several metabolic pathways have been implicated in the development of DR. The most common pathways studied for diabetes are the i)polyol pathway, ii) formation of advanced glycation end products, iii) activation of protein kinase C (PKC) and the iv) Hexosamine pathway and oxidative stress. Out of all the mechanisms, the oxidative stress has been reported to be the most important reason for the damage of the retinal cells (Kowluru et al, 2015). The pathways are described in detail below:

i) The Polyol Pathway: In normal conditions, only a small amount of glucose is processed through the polyol pathway as aldose reductase has low affinity for glucose. When there is excess of glucose in the circulatory system, aldose reductase converts the unused glucose to sorbitol by using NADPH as a cofactor. The reduced levels of NADPH in turn leads to a reduction in glutathione levels and increased oxidative stress, an underlying factor in diabetic retinopathy. Sorbitol is further oxidized to fructose by sorbitol dehydrogenase during which NAD+ is reduced to NADH. Sorbitol is less permeable through the cell membrane and hence it accumulates in the cells causing osmotic damage (Mathebula, 2015).

ii)Advanced Glycation End products: The polyol pathway produces fructose which is phosphorylated to fructose -3-phosphate and 3-deoxyglucosone both of which participate in the formation of advanced glycation end products (AGEs). AGEs are a product of non-enzymatic reduction of sugars with amino acids and proteins, and Diacylglycerol (DAG). The accretion of AGEs under hyperglycemic conditions disrupts the microvascular homeostasis. AGEs interact with a receptor called RAGE which is a primary contributor in inflammation and microvascular dysfunction in diabetic retinopathy(Safi, Qvist, Kumar, Batumalaie, & Ismail, 2014).

iii)Activation of Protein Kinase C: Increased sorbitol dehydrogenase activity in the cells effects an increased NADH/NAD+ ratio leading to an increase in DAGs by inhibiting triose phosphate, which in turn activates Protein Kinase C (PKC) and increases cytokine production in cells. The activated PKC contributes to the basement membrane thickening, vascular occlusion, increased vascular permeability and activation of angiogenesis. Activation of PKC also results in vascular permeability and disruptions in the retinal blood flow and development of neovascularization (Eshaq et al, 2017) (Mathebula, 2015).

iv) Activation of Hexosamine Pathway: The Hexosamine pathway is activated under hyperglycemic conditions wherein some of the glucose in converted to glucose-6-phosphate and fructose -6-phosphate. The fructose-6-phosohate is converted to glucosamine-6-phosphate which in turn are metabolized to uridine diphosphate-N-acetyl glucosamine (UDPGlcNAc) and UDP-N-acetylgalactosamine. They act as substrates for glycosylation which leads to gene and protein function alterations and apoptosis (Eshaq et al, 2017) (Mathebula, 2015).

The end product of the polyol pathway and as a result all the other pathways is the production of reactive oxygen species (ROS) which produce oxidative stress in the cells (Figure 53).An imbalance in the ROS production leads to macro molecular protein and DNA damage in the

cells. It also affects the mitochondria and the electron transport chain which initiates a cascade of reactions leading to mitochondrial dysfunction and leads to further production of ROS and superoxides (Renu A. Kowluru & Mishra, 2015). The mitochondrion plays an important role in the production of ROS and in the pathogenesis of DR.

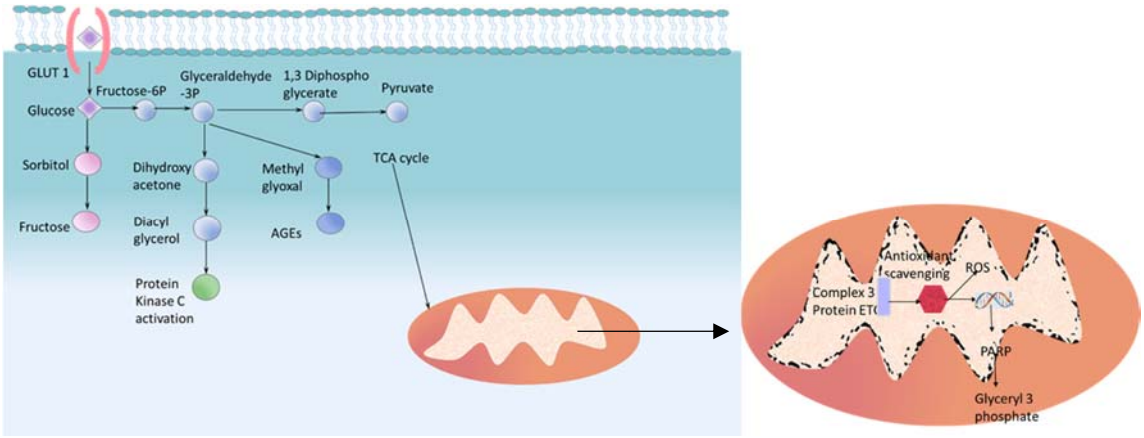

Figure 53 Molecular mechanisms inside the cell and mitochondrion under hyperglycemic and DR conditions

3.1.5 Mitochondria and production of ROS

The mitochondrial electron transport chain includes four protein complexes called complex I, II, III and IV. In normal circumstances, the glucose is metabolized through the Tricarboxylic acid (TCA) cycle, which produces electron donors, primary of which is called NADH which gives electron to complex I (Brownlee, 2005). The energy of the electrons across the membrane is used to pump protons to complexes I, II, III and IV. The transport of protons creates a voltage difference across the membrane which drives the synthesis of ATP by ATP synthase. Under hyperglycemic conditions, the voltage gradient across the membrane is increased till a threshold point is reached. Beyond this point, the electron is unable to be transferred to complex III causing the electrons to accumulate at coenzyme Q, which results in the formation of superoxide

(Brownlee, 2005). In DR, this impaired complex III activity is noticed in the retinal and capillary cells which leads to increased ROS in the cell. The increased cytosolic ROS in diabetes activate the MMPs in the retina. The activated MMPs damage the mitochondrial membrane and disrupt the functioning of the Complex III protein and subsequently the antioxidant scavenging machinery is compromised. This leads to accumulation of free radicals in the mitochondria and leads to vicious cycle of mitochondrial damage and production of superoxide or free radicals. The increased mitochondrial ROS disrupts the nuclear DNA by breaking the double strands. The DNA present in the mitochondria are circular and lack histones. These mitochondrial DNA in the retina are prone to oxidative damage. The guanine bases in the DNA are modified to form 8-OHdG (8-hydroxy 2-deoxy guanosine). Hence, there is an increase in 8-OHdG production in the mitochondria in the retinal cells of the patients with DR.

3.1.6 8-OHdG as a biomarker

Mitochondrial DNA from tissue and blood lymphocyte are prone to oxidative damage. The guanine in the DNA undergoes oxidation, wherein a hydroxyl group is added at the 8^{th} position of the guanine molecule (Figure 54). 8-OHdG is the most prominent form of free radical induced DNA lesion. After the damage occurs, the cells have the capability to recognize and remove the oxidized lesion by base excision pair mechanism. The oxidized guanine is cleaved by enzymes such as endonuclease and glycosylase, removed from the cell into the blood which is then further excreted out through the urine. Hence, the amount of 8-OHdG in the system is indicative of the extent of DNA damage taking place in the body. The oxidized nucleosides like 8-OHdG are not further metabolized in the system and are excreted through the urinary system as they are easily soluble in water(L. L. Wu et al., 2004). Thus, the amount of urinary 8-OHdG reflects the level of oxidative damage taking place in the body. Few research groups have reported that urinary 8-

OHdG/creatinine levels are higher in patients with Diabetic Nephropathy as compared to patients with no Diabetic Nephropathy or retinopathy (Hinokio et al., 2002). The studies were conducted in a cohort of 396 patients in Japan.

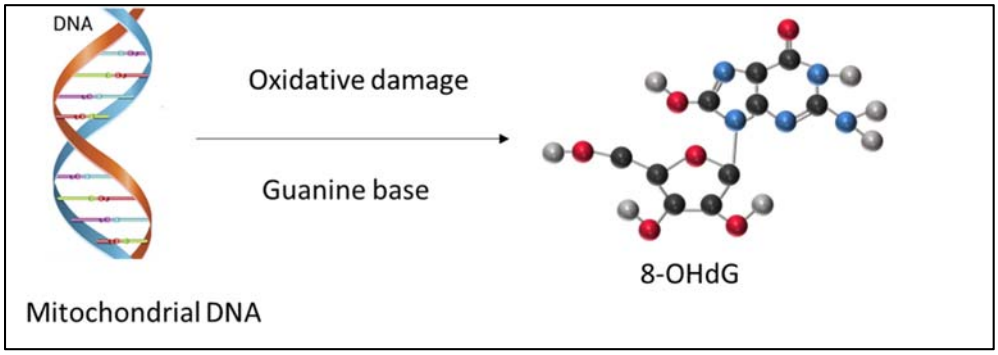

Figure 54 Oxidization of guanine base of mitochondrial DNA to form 8-OHdG

3.1.7 Detection of 8-OHdG

The most commonly used analytical techniques for the detection for 8-OHdG are high-performance liquid chromatography-electrochemical detection (HPLC-ED), HPLC tandem mass spectrometry, gas chromatography-mass spectrophotometry (GC-MS), Capillary Electrophoresis with electrochemical detection (CE-ECD)(X. Zhu et al., 2014). These techniques have good sensitivity and accuracy, however these are lab based techniques requiring expensive instrumentation and trained personnel. Enzyme Linked Immunoassay (ELISA) is also used for the colorimetric detection of 8-OHdG. 8-OHdG is a small molecule, hence the major challenge is to immobilize it for the purposes of capture and detection (L. L. Wu et al., 2004). The most common method for detection of 8-OHdG is by conjugating it with a heavy protein like BSA (Bovine Serum Albumin) and conducting a competitive ELISA for the detection and analysis. Albeit being less complex than HPLC techniques, it is still is a lab based and labor intensive technique. Hence, it is not suitable for bed side or in-house detection of 8-OHdG. For these

purposes, there is a need for the development of a point-of-care testing device which is portable and has faster readout times. A Lateral Flow Immunoassay (LFIA) is a paper based assay techniques which is based on the principle of sample movement through capillary flow on a nitrocellulose membrane (X. Zhu et al., 2014). It is also a colorimetric technique, where the amount of the analyte is visualized based on the color intensity of the sensor. The sensor has high sensitivity and can be comparable with other established lab procedures.

3.1.8 Hypothesis and Solution

Hinokio et al found a significant progression of diabetic nephropathy and diabetic retinopathy with increased levels of 8-OHdG in urine. A few studies in Japan and South Korea have demonstrated that amount of 8-OHdG can have a direct correlation with the onset of DR(Ref). From these initial studies, we extrapolated and hypothesized that the amount of urinary 8-OHdG and the 8-OHdG/Creatinine ratio will be higher in patients with DR than in patients with no DR in a cohort of Caucasian population. To this effect, we conducted a study with a two-pronged approach. First, we developed different substrates for the accurate and fast detection of 8-OHdG. Secondly, we conducted an exploratory study to examine whether urinary 8-OHdG levels can be correlated with the status of DR in a cohort of Caucasian population (n=80). We developed a library of BSA-OHG substrates by conjugating BSA-OHG to different nano and micro particles. We then developed a paper (nitrocellulose) based colorimetric dip sensor, a Lateral Flow Immunoassay (LFIA) to develop a fast and portable platform for the detection of urinary 8-OHdG. The different colorimetric substrates used was gold nanoparticles and gold nanoclusters respectively.

3.1.9 Competitive ELISA

Enzyme Linked Immunoassay (ELISA) is a gold standard for detecting molecules in biological assays (Santella, 1999). It is a highly sensitive and accurate colorimetric method for analysis of biological molecules and has been widely utilized for analyzing proteins, antigens and oligonucleotides and small molecules (L. L. Wu et al., 2004). Some studies have reported the detection of urinary 8-OHdG by competitive ELISA techniques (Hinokio et al., 2002) (Chiou et al., 2003). 8-OHdG is a small molecule, hence the major challenge is to immobilize it for the purposes of capture and detection(L. L. Wu et al., 2004). 8-OHdG is conjugated with a protein molecule like BSA for improved adherence to the substrate (Wu et al). Competitive ELISA is based on the principle of competitive binding of the antigen to the antibodies (Figure 55). The signal intensity is inversely proportional to the concentration of antigen in the sample. Despite being sensitive and accurate and less complex than HPLC and Mass Spec, ELISA is still lab based technique which both labor intensive and time consuming. In order to develop a simple in-home sensor, it is important to develop a more portable and easy to use Point-of-Care device.

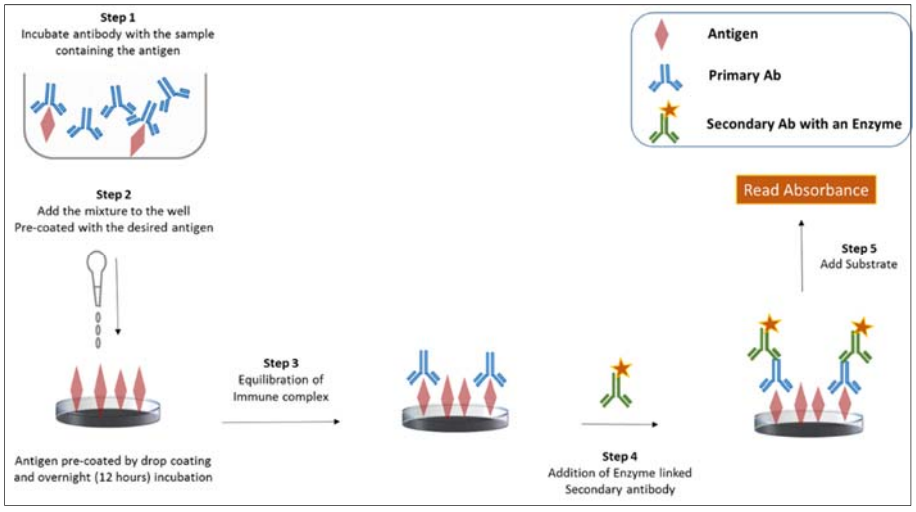

Figure 55 Schematic of the working principle of Competitive ELISA on a 96 well plate

3.1.10 Lateral Flow Immunoassay (LFIA)

An ideal point of care device should enable fast and accurate detection of 8-OHdG without the need of any complex equipment. A lateral flow immunoassay is a chromatographic assay which works on the principle of capillary flow on a nitrocellulose membrane (Zhu et al, 2014). The qualitative or quantitative status of the analyte is visualized through a colorimetric substrate. The signal readout is usually done by capturing images in a smartphone and analyzing through image analysis software. A paper strip consists of a sample pad, conjugate pad, test line, control line and the absorbent pad. The signal intensity is inversely proportional to the amount of analyte present in the sample (Figure 56).

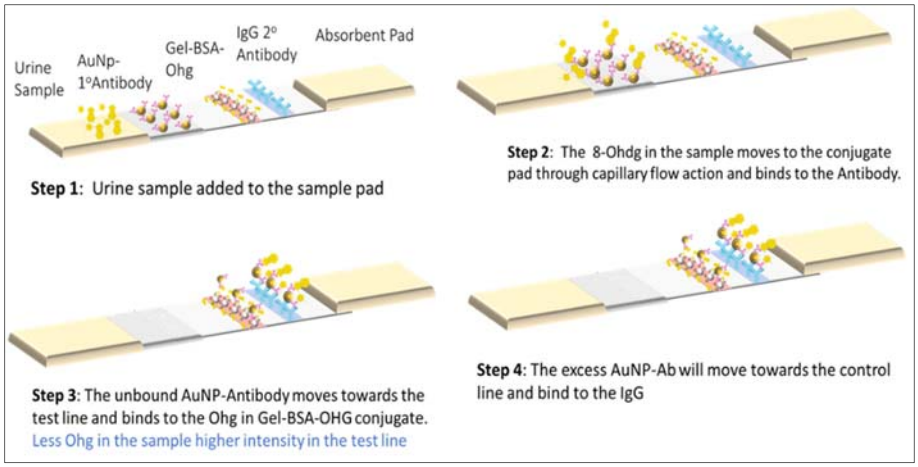

Figure 56 Schematic of the working principle of Lateral Flow Immunoassay based Paper sensor

3.1.11 Metallic Nanoparticles and Nanoclusters

Gold nanoparticles exhibit unique optical and surface properties and are widely utilized in biological applications like determination of tumor biomarkers, toxins etc. (Wu et al, 2015). The advantages of gold nanoparticles are that they are highly biocompatible, easily modified for surface functionalization. (Wu et al, 2015). Another important property of gold nanoparticles is

the induction of Localized surface Plasmon resonance (LSPR) on incidence of light. The nanoparticles absorb and scatter light with greater intensity than their bulk material counterparts (Anker et al, 2008). This property enables the gold nanoparticles to be used as colorimetric labels for immunoassays and other biological applications (Anker et al, 2015) (Figure 57). In this project, gold nanoparticles were used as colorimetric substrates for detection of 8-OHdG in paper strip based Lateral Flow Immunoassay. The gold nanoparticles were functionalized with anti-8-OHdG antibody using electrostatic binding

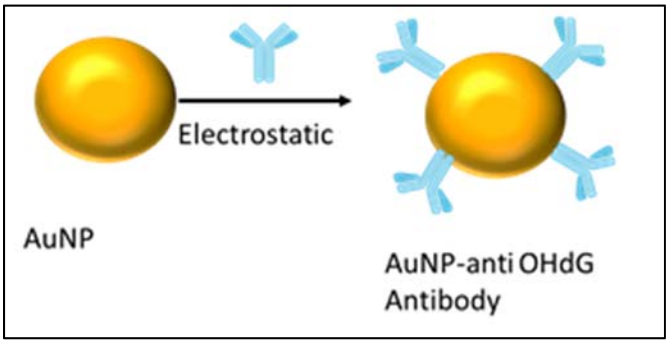

Figure 57 Schematic of conjugation of anti-8-OHdG antibody to Gold nanoparticle

Fluorescence is another common technique used for the detection of the several analytes (Shang, Dong, & Nienhaus, 2011). Generally, fluorophores are conjugated with antibodies or other nanoparticles to impart the fluorescent properties of the substrate. There have been some reports suggesting that Gold ions reduced and sequestered in a protein solution form gold nanoclusters of 20 nm size which have altered optical properties (Xie, Zheng, & Ying, 2009) (Figure 58 a). These nanoclusters exhibit a bright pink color when they are exposed to UV light (Figure 58 c). The fluorescent properties of the gold nanoclusters can be used as an ELISA substrate as well as

for the lateral flow paper sensor. We have utilized the fluorescent nanoclusters for competitive ELISA assays.

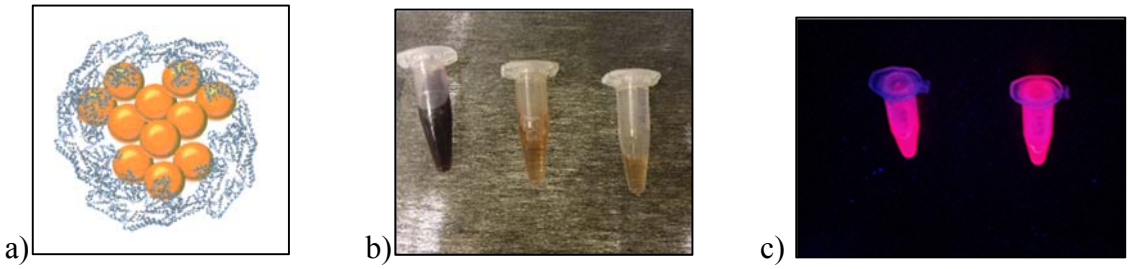

Figure 58 a) Schematic of Gold-BSA (Au-BSA) nanoclusters b) Dark red color of Au-BSA under normal light c) Bright pink color of Au-BSA nanoparticle under UV (Ultraviolet Ray)

3.1.12 BSA-OHG substrates for 8-OHdG detection

8-OHdG is a small molecule and its direct immobilization on any surface is challenging. The 8-OHdG must be conjugated with a carrier protein like BSA (Bovine serum albumin) (Ref). We have conjugated BSA with 8-OHdG by a periodate oxidation method. The diol groups of the ribose moiety are oxidized to dialdehyde which is then conjugated with the amino groups of the amino acid by carbodiimide bond (Figure 59) (Ref). From initial ELISA experiments it was observed that BSA-OHG was amenable to being washed away after several washing steps. We explored the immobilization of BSA-OHG by conjugating with other protein nanoparticles and beads.

A library of BSA-OHG conjugates were prepared by conjugating it with gelatin nanoparticles, Latex beads and magnetic nanoparticles

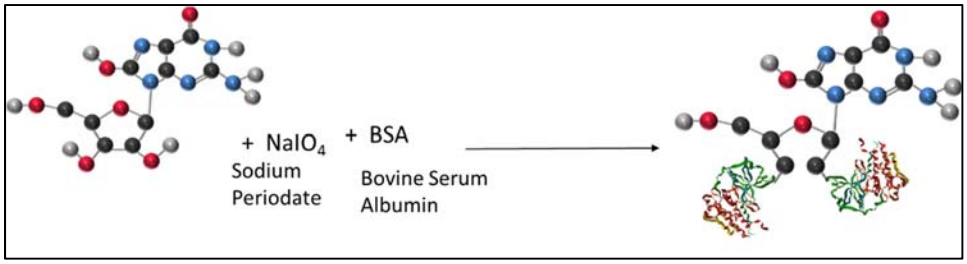

8-OHG BSA-OHG

Figure 59 Schematic of synthesis of BSA-OHG conjugate using periiodate reduction method

Gelatin is a versatile protein which is obtained from denaturation of collagen (Naidu & Paulson, 2011). Gelatin nanoparticles formed by two step de-solvation method with acetone precipitation and crosslinked with glutaraldehyde are very robust nanoparticles that are used for several applications (Coester, Langer, van Briesen, & Kreuter, 2000). The gelatin nanoparticles can be covalently conjugated with antibodies and used as substrates for ELISA and LFIA. (Figure 60) ELISA studies showed that these nanoparticles are more adherent to the surface as compared to the other conjugates. We chose the Gel-BSA-OHG as the robust substrate for all the consecutive ELISA and LFIA experiments for optimization and clinical studies.

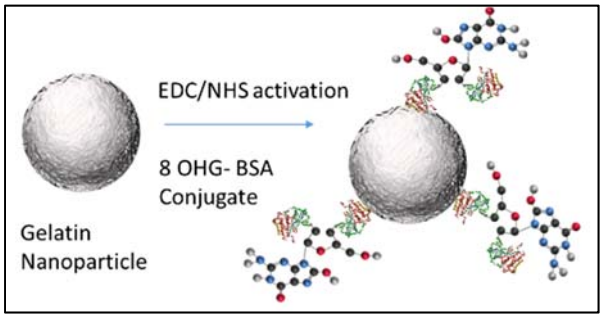

Figure 60 Schematic of synthesis Gelatin-BSA-OHG conjugate using EDC/NHS conjugation

We conducted optimization studies with the Gel-BS-OHG conjugates and AuNp nanoparticles for ELISA and LFIA assays. We also analyzed urine samples from 80 patients with and without

DR. We analyzed the samples using Competitive ELISA and Lateral Flow Immunoassay and found that both the assay results correlated well with the Fundus Results.

3.2 Materials and Methods

3.2.1 Materials

$HAuCl_4$ (Hydrogen Tetraaurochlorate) was purchased from Acros Organics. Bovine Serum Albumin (BSA), Sodium Periodate, 1-Ethyl-3-(3-dimethylaminopropyl) carbodiimide(EDC) and Bicinchonic assay kit were purchased from Sigma Aldrich. Gelatin, Sodium citrate trihydrate, Hydroxy sulfo succinimide (Sulfo-NHS) were purchased from Thermo Fisher Scientific. OHG and 8-OHdG were purchased from Cayman Chemicals. Anti-8-OHdG [15A3] antibody was purchased from AbCam. Anti-Mouse IgG-HRP was purchased from Jackson Laboratories. Polyethylene Glycol-NHS (PEG-NHS) and succinimidyl PEG-NHS were purchased from Nanocs. TMB substrate was purchased from BioRad. The Nitocellulose membrane, the sample pad and the conjugate pad were purchased from Millipore. Artificial Urine was purchased from QuikFix.

3.2.2 Instruments

Core nanoparticle size measurements were performed using Joel TEM. Hydrodynamic size and zeta potential was measured using a Malvern Zetasaizer Nano-ZS. Centrifugation was performed on a 5424 Eppendorf and refrigerated RC 6+ Sorvall centrifuge. pH was measured using a Seven Compact Mettler Toledo pH meter equipped with an InLab Micro electrode. Fluorescence imaging, fluorescence assays and UV-vis absorption assays were performed on a Cytation 5 Cell imaging multi-mode reader. Gel electrophoresis was performed on a Biorad Mini-Protean Tetra system and blots were transferred using a Genscript e-blot transfer system.

Western blot imaging and acquisition was performed using Image Lab ver 5.2.1 software on a ChemiDoc XRS system from Biorad. Band densitometry analysis was performed on Image Studio ver 5.2. Solvent extraction was performed on a Büchi Rotovapor R-124 attached to a water bath and watercoo led distillation column. SQUID measurements were performed on a Quantum Design MPMS 3 Magnetometer. The antibodies and substrate were coated on the paper strip using a Camag Linomat 5 automated dispenser.

3.2.3 Synthesis of Fluorescent Gold nanoparticles

Fluorescent Gold nanoparticles were synthesized based on a previously published protocol with a few modifications(Xie et al., 2009). BSA (250mg) was dissolved in 5ml DI water followed by addition of 5ml $HAuCl_4$ solution (10mM) and heated to 37ºC by stirring continuously. When the solution reached 37ºC, the pH was adjusted to 12.0 by adding 1M NaOH and stirred overnight at 37ºC to get a dark red color. The Au-BSA nanoclusters thus formed are fluorescent and can be checked for fluorescence under portable UV light. The Au-BSA nanoparticles were functionalized with PEG-NHS (MW 2000) to block the amine groups in the BSA to prevent crosslinking. Briefly, 2ml of washed Au-BSA nanoparticles were taken in a vial. The pH of the solution was adjusted to 7.5 with MES buffer. 50mg of PEG-NHS was added to the pH adjusted solution and stirred overnight at room temperature. The PEGylated Au-BSA nanoclusters were purified by passing them through 100kDa centrifugal filters three times. The PEGylated Au-BSA nanoclusters were conjugated with Anti-8-OHdG antibody using EDC-NHS conjugation. 2mg of EDC and 3 mg NHS in 40ul MES buffer was added to 200µl PEGylated Au-BSA nanoclusters (pH 4.5) followed by activation at RT for 4 hours. The activated nanoparticles were passed through 100kDA filter at 6000g to remove excess EDC and NHS. 10µl of 1mg/ml Anti-8-OHdG antibody was added to the

particles and the pH of the solution was increased to 7 by adding 0.1M followed by overnight mixing at RT in a thermomixer. The antibody conjugated Au-BSA nanoclusters were passed through 100kDa filter at 6000g to remove any excess antibody.

3.2.4 Synthesis of BSA-OHG Conjugate

BSA-OHG conjugate was synthesized based on a previous publication with some modifications (Xuena Zhu et al., 2013). BSA solution was prepared dissolving 12.5mg BSA in 1 ml of 50mg/ml K_2Co_3. 8-OHG (0.5 mg) was dissolved in 100 µl of periodate and mixed in dark conditions for 1 hour in a thermomixer at RT. 200µl of the prepared BSA solution was added to OHG solution and mixing was continued for 1 hour in dark followed by addition of 200ul of $NaBH_4$ (24mg/ml). The solution mixed overnight at 4^oC and passed through 10kDa filter.

3.2.5 Synthesis of Gelatin nanoparticles

Gelatin nanoparticles were synthesized using a two-step desolvation process (Coester et al, 2000) (Srikar et al., 2016). Gelatin type A (500 mg) was dissolved in 10 ml Deionized water (DIW) at 50^oC. 20 ml of acetone was added rapidly to initiate the first de-solvation process. The gelatin particles were precipitated and dissolved in 10ml DIW (pH 2.75) followed by second de-solvation by rapid addition of acetone (3ml/min) to form a milky solution. The nanoparticles were cross-linked by adding 200µl 25% glutaraldehyde and stirring the solution overnight at 50^oC. The gelatin nanoparticles were washed with DIW at 20,000g for 45 minutes for 5 times.

3.2.6 Synthesis of Gel-BSA-OHG conjugate

BSA-OHG was covalently conjugated with gelatin nanoparticles using EDS/NHS activation method (Ref). 1 ml Gelatin nanoparticles (6mg/ml) were centrifuged at 15,000g for 12 minutes. The supernatant was discarded and to the pellet 2.4 mg EDC in 3.6 mg of NHS were added in

40µl. The volume of the solution was made to 1ml and incubated in thermomixer at 24ºC for 4 hours. The activated nanoparticles were washed once to remove excess EDC and NHS. 36 µl of BSA-OHG in 1 ml 1X PBS was added to the nanoparticles and mixed overnight. The BSA-OHG conjugated nanoparticles were washed twice with 1X PBS. The final pellet was dissolved in 1X PBS.

3.2.7 Competitive ELISA

Competitive ELISA was used to test the specificity of the BSA-OHG conjugates. In this procedure the BSA-OHG conjugates were coated on a 96 well plate overnight at 4ºC. The wells were washed and blocked with blocking buffer (2% milk). The primary antibody against 8-OHdG was added to the 8-OHdG solution (antigen) and incubated for 15 minutes prior to adding to the wells. The antibody-antigen solution was incubated with the BSA-OHG conjugate for 2 hours at 37ºC. The wells were washed and incubated with the secondary antibody IgG-HRP conjugate for 30 minutes at 37ºC followed by washing and addition of the TMB substrate. The wells were read at 450nm.

3.2.8 Comparison of the BSA-OHG and Gel-BSA-OHG conjugates

The 96 well plates were each coated with OHG, BSA-OHG and Gel-BSA-OHG conjugate overnight at 4ºC. The wells were washed and blocked with blocking buffer (2% milk). The primary antibody against 8-OHdG was added to the OHdG solution (antigen) and incubated for 15 minutes prior to adding to the wells. The antibody-antigen solution was incubated with the BSA-OHG conjugate for 2 hours at 37ºC. The wells were washed and incubated with the secondary antibody IgG-HRP conjugate for 30 minutes at 37ºC followed by washing and addition of the TMB substrate. The wells were read at 450nm. The experiment was repeated with Fluorescent gold nanocluster (fAuNC)-Antibody conjugates. The 96 well plates were each coated with OHG, BSA-

OHG and Gel-BSA-OHG conjugate overnight at 4ºC. The wells were washed and blocked with blocking buffer (2% milk).fAuNC-Antibody was added to the 8-OHdG solution (antigen) and incubated for 15 minutes prior to adding to the wells. The antibody-antigen solution was incubated with the BSA-OhG conjugate for 2 hours at 37ºC. The wells were washed and incubated with the secondary antibody IgG-HRP conjugate for 30 minutes at 37ºC followed by washing and addition of the TMB substrate. The wells were read at 450nm.

3.2.9 Interference studies with Gel-BSA-OHG

Interference studies were conducted to test whether the other components of the urine had any effect on the outcome of the 8-OHdG analysis assay. Commercially available artificial urine made by the company called Quikfix was used for the purposes. 100µl Gel-BSA-OHG was coated on a 96 well plate and incubated overnight at 4ºC. ELISA was performed using artificial urine. OHdG was dissolved in artificial urine instead of DIW and 50µl of different concentrations of artificial urine solution mixed with OHdG were added along with 50µl of anti-OHdG antibody solutions and the plates were read at 450nm using a Cytation 3.

3.2.10 Monolayer vs Multilayer coating of Gel-BSA-OHG

100µl of Gel-BSA-OHG was coated on the wells of a 96 well plate. In another well 60µl of gel-BSA-OHG was coated. Due to the dimension of the well the 100µl coating will form multiple layers on the well while the 60µl coating will form a single or monolayer on the well. Competitive ELISA was performed to test the specificity of monolayer and multilayer coating.

3.2.11 Synthesis of Gold Nanoparticles (AuNPs) for Lateral Flow Immunoassay

The AuNPs were synthesized by a modified citrate reduction method (Afrasiabi et al., 2010) Briefly, 50 ml of 0.01% $HAuCl_4$ solution was heated to a boil followed by a rapid addition of trisodium citrate solution (1 mL, 1%) under vigorous stirring. After the color changed from yellow to red, the solution was continued to boil for another 10 min, then stirred without heating till the solution reached the room temperature.

3.2.12 Synthesis of AuNP-Anti (8-OHdG) conjugate

The AuNPs solution was concentrated 10X using a 70KD membrane filter. The pH of the AuNPs solution was adjusted to 8.5 ~ 9.0 with K_2CO_3 (0.1 M). The optimum concentration of antibody necessary for conjugating the AuNPs to stability is determined by a salt based aggregation test. The electrostatically stabilized AuNPs aggregate in the presence of salt till the surface is stabilized by enough protein. Briefly, 50µl of antibody of decreasing concentrations (1, 0.5, 0.25, 0.125, 0.0625, 0.03125 mg/ml) were taken in separate tubes. They are incubated with 750 µl of 10X AuNPs for 20 mins followed by the addition of 0.5 ml of 10% NaCl to all of them. We observed that the color of AuNP turned blackish blue and the LSPR peak underwent blue shift to all the concentrations below 0.5 mg/ml. Thus, 0.5mg/ml is the optimum concentration of the antibody. To ensure maximum loading of the antibody, the 10X AuNPs (900 µl) were incubated with 50 µl of 1mg/ml purified anti-8-OHdG Ab at 750 rpm, RT for 1 hour. The conjugate was then incubated with BSA (10%) in sodium borate (20 mM) for a final concentration of 1% for another 20 min. Then the mixture was centrifuged for 15 min at 7000 rcf. The faint pink supernatant of unbound antibodies was discarded, and the pellet was resuspended in BSA/PBS (900 µl,1%) to further wash

away any unbound antibodies. Following the same centrifugation step, the supernatant was removed, and the soft sediment of conjugates was resuspended in conjugate pad buffer (900 µl).

3.2.13 Lateral Flow Assay (Paper Strip Assay)

The conjugate pad, sample pad and absorbent pad were assembled with 1-2 mm overlap on a 6 cm x 30.1 cm laminated cards with Hi-Flow Plus lateral flow membrane with a 0.19mm backing adhered to the surface of the card (HF180MC100 Millipore). Once assembled, Gel-BSA-8OHG (1mg/ml) and goat anti-mouse IgG (1mg/ml) were dispensed on the nitrocellulose membrane (2µl/cm) using a Linomat 5 dispenser as test line and control line respectively. The assembly was then dried for 1 hour at 37 °C, cut into 4mm wide strips using a strip cutter and the strips were stored in the desiccator at RT. The 4mm wide strips were immersed in 80 ml of standards or urine samples in transparent plastic vials. The development of color was seen within 10 min. To maximize the color intensity and to maintain uniformity, the photographs of the strips were taken 90 min after their dip in the standards/samples. The intensity of the color was quantified using ImageJ software.

3.2.14 Analysis of 8-OHdG using LFIA

80ul of 8-OHdG solutions of varying concentrations (0, 5, 10, 20, 40, 50 60, 70 ng/ml) were added to a quartz cuvette and the paper strip was dipped in the solutions. The color development on the test line was observed for the strips within 5 minutes and the test and control lines images were captured using a camera. The images were analyzed using ImageJ software and a standard curve was obtained by plotting the ratio of the intensity of test line/ nitrocellulose membrane against concentration (ng/ml) of 8-OHDG.

3.2.15 Interference studies with LFIA

Interference studies were conducted to test whether the other components of the urine had any effect on the outcome of the 8-OHdG analysis assay. Commercially available Artificial Urine made by the company called Quikfix was used for the experiments. 8-OHdG was dissolved in artificial urine at various concentrations (0, 5,15,10,20 ng/ml) and 80µl of the solution was added to quartz cuvette. The paper strip was dipped in the solution and the color development at the test and control lines was captured by a smartphone camera after 1 hour.

3.2.16 Collection of clinical samples

The IRB for the study was approved by the review board in University of Missouri, Columbia (IRB No 2004053). Urine samples were collected from patients above the age of 18, who visited the Mason Eye Institute at the University of Missouri, Columbia with their consent. The patients had no known history of cancer. The urine samples were collected once from each patient and was stored at -20 C immediately till they were analyzed. Samples were collected from patients who were diagnosed with NPDR as well as from patients without DR. The urine samples were centrifuged at 3000g before analysis. Creatinine values were analyzed using a commercially available Creatinine assay kit by the MU Biorepository. 8-OHdG values were analyzed using Competitive ELISA as well as Lateral Flow Immunoassay.

3.2.17 8-OHdG Analysis of clinical samples

The urine samples were analyzed by both Competitive ELISA and LFIA procedures.

For the competitive ELISA procedure, 60 Gel-BSA-OHG was coated on 96 well overnight at 4^{o}C. The wells were washed and blocked with blocking buffer (2% milk). The primary antibody against 8-OHdG was added to the 8-OHdG solution (antigen) and incubated for 15 minutes prior to adding

to the wells. The antibody-antigen solution was incubated with the BSA-OHG conjugate for 2 hours at 37^{o}C. The wells were washed and incubated with the secondary antibody IgG-HRP conjugate for 30 minutes at 37^{o}C followed by washing and addition of the TMB substrate. The wells were read at 450nm.

For LFIA, urine samples were centrifuged at 3000g. 80µl of the samples were added to a quartz cuvette. The color development at the test and control line was captured using a smartphone after 1 hour. The intensity of the test line of the urine samples was analyzed using ImageJ and the 8-OHdG values were calculated based on the standard curve of known 8-OHdG values.

3.3 Results and Discussion

3.3.1 Synthesis and Characterization of BSA-OHG conjugate

The conjugation of BSA to OHG was ascertained by UV-Vis absorption of the BSA-OHG conjugate. The UV-vis absorption spectrum of the BSA-OHG was broader compared to that of the unconjugated BSA (Ref). The amount of OHG conjugated to BSA was estimated using UV-Vis absorption. The conjugation efficiency of the OHG to BSA was estimated to be around 33%.

3.3.2 Synthesis and Characterization of Gelatin nanoparticles

Gelatin nanoparticles were synthesized by two step de-solvation process. The hydrodynamic and core size of the nanoparticles was determined by Dynamic light scattering method (DLS) and Transmission Electron Microscopy (TEM) respectively. The TEM images confirmed formation of uniform nanoparticles with a size of 220nm (Figure 61). The zeta potential of the nanoparticles was 18 mV as recorded by the Zeta sizer. The results corroborated with the literature values (Srikar et al, 2015)

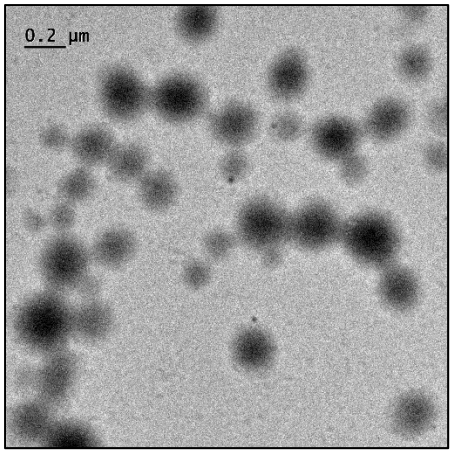

Figure 61 TEM of Gelatin nanoparticles

Gelatin nanoparticles were conjugated to BSA-OHG with EDC/NHS activation reaction (Ref). The conjugation of the BSA-OHG to Gelatin nanoparticles was confirmed using zeta potential measurement and hydrodynamic size. The conjugation efficiency was estimated to be around 35% using Bradford and BCA assay and UV-vis absorbance technique. The hydrodynamic size and zeta potential of the nanoparticles are listed in Table 3

Construct Name	Hydrodynamic size (d.nm)	Zeta (mV)
Gelatin	220	18
Gelatin-BSA-OHG	250	10

Table 3: Hydrodynamic size and Zeta Potential of Gelatin and Gel-BSA-OHG nanoparticles

3.3.3 Synthesis and characterization of Gold Nanoparticle conjugates

The gold nanoclusters were formed in situ at pH 12 and were stabilized by the BSA molecules. The fluorescent nanoclusters emitted a bright red fluorescence under UV light and exhibited excitation and emission peaks at 480nm and 640 nm respectively (Figure 62 a). TEM of the gold nanoclusters revealed that the core size was around 25 nm (Xie et al., 2009)(Figure 62 b). The gold nanoclusters were functionalized with poly ethylene glycol polymer (PEG-NHS 2000) to

introduce carboxyl groups to the nanocluster which would be utilized for antibody conjugation. The PEGylating of the nanocluster was confirmed by monitoring the changes in zeta potential and hydrodynamic size compared to starting material. The functionalized Gold NCs were conjugated with anti-OHDG antibody by activating the carboxyl groups with EDC/NHs reaction followed by conjugation with amine group in the antibody thereby forming a carbodiimide bond. The antibody conjugation was confirmed using UV-vis spectrum and zeta potential measurements. The zeta potential values decreased on addition conjugation of anti 8-OHdG antibody.

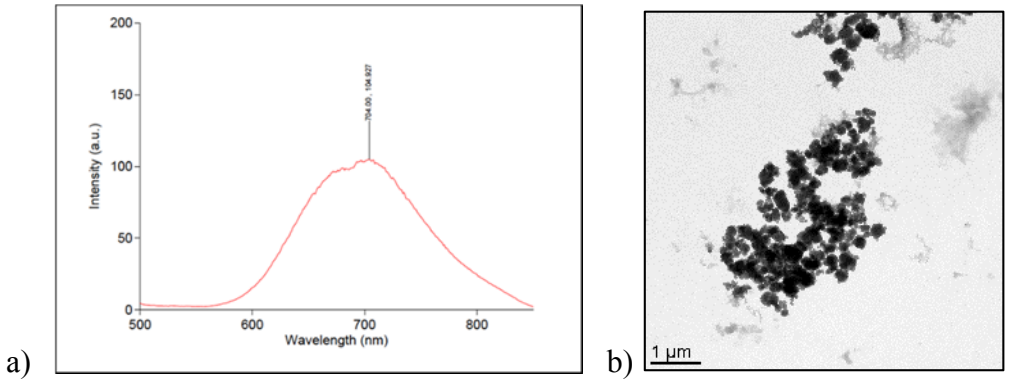

Figure 62 a) Fluorescence of Gold Nanocluster b) TEM images of Gold nanocluster

Gold nanoparticles were synthesized by reduction of gold ions using sodium citrate as a reducing as well as stabilizing agent. UV-vis absorbance was recorded to confirm the formation of gold nanoparticles which exhibit an absorbance peak at 520 nm (Afrasiabi et al., 2010) (Figure 63 a). Size and zeta potential analysis established a hydrodynamic size of 20 nm and zeta potential of -19 mV and correlated well with reported values (Afrasiabi et al, 2010) . TEM Images of gold nanoparticles revealed the core size of 20 nm (Figure 63 b).

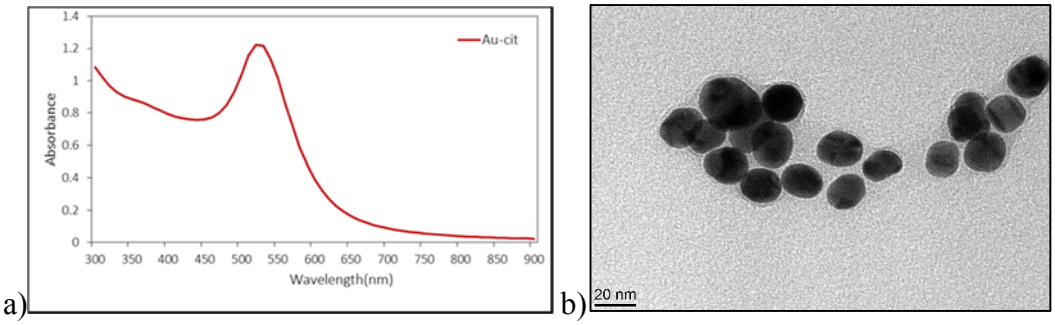

Figure 63 a) UV-Vis absorbance of Gold Nanoparticle b) TEM Image of Gold nanoparticle

In order to conjugate anti-OHDG antibody to the Gold NPs, they were concentrated to 10X and the pH adjusted to 8. The antibodies were bound to the negatively charged gold nanoparticles via electrostatic binding. The conjugation was followed by blocking with BSA buffer to block the free surfaces of the gold antibody conjugate. The amount of antibody required for conjugation was determined by NaCl precipitation method (Figure 64).

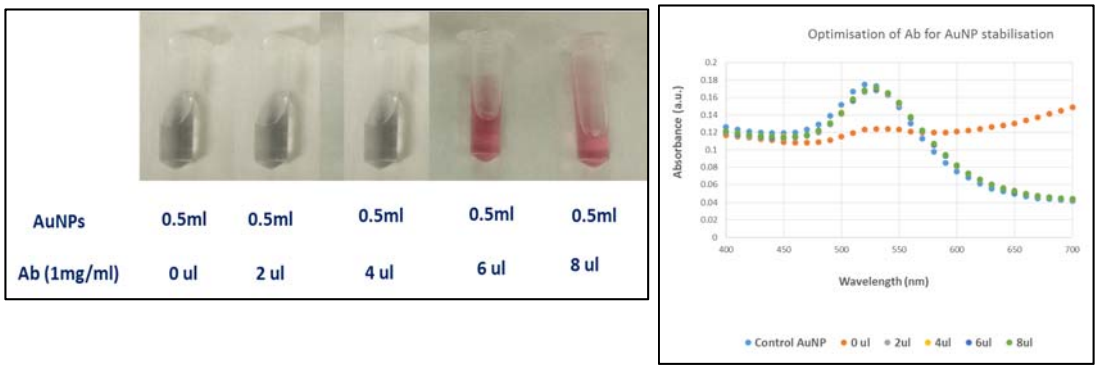

Figure 64 Optimization of antibody concentration. No change in color when antibody is saturated.

3.3.4 Evaluation of BSA-OHG and Gel-BSA-OHG Substrate

The binding affinity of BSA-OHG or Gel-BSA-OHG to antibody of OHG (anti-OHG) was investigated by ELISA using appropriate controls. The binding affinity was monitored using a secondary antibody anti-mouse-IgG-HRP. We hypothesized that conjugation of OHG to BSA or

Gel-NPs should not alter the binding affinity towards anti-OHG. Only if the binding affinity is retained, these constructs could be used as a substrate in the sensor components. BSA-OHG and Gel-BSA-OHG show serial decrease in absorption. The absorbance values for Gel-NPs, physical mixture of BSA and OHG, BSA and PBS that contain no OHG are negligible. The results validate that (i) OHG is bound to both BSA and gelatin nanoparticles (Gel-NPs) (ii) the binding affinity towards anti-OHG is retained (iii) one of these constructs can be used as substrates to mimic OHG for lateral flow (Figure 65). Upon observing the absorbance changes, it is very clear that Gel-BSA-OHG shows incremental and proportional changes compared to BSA-OHG and OHG. Therefore, Gel-BSA-OHG appears to be an ideal candidate and can be utilized as immobilization substrate for OHG.

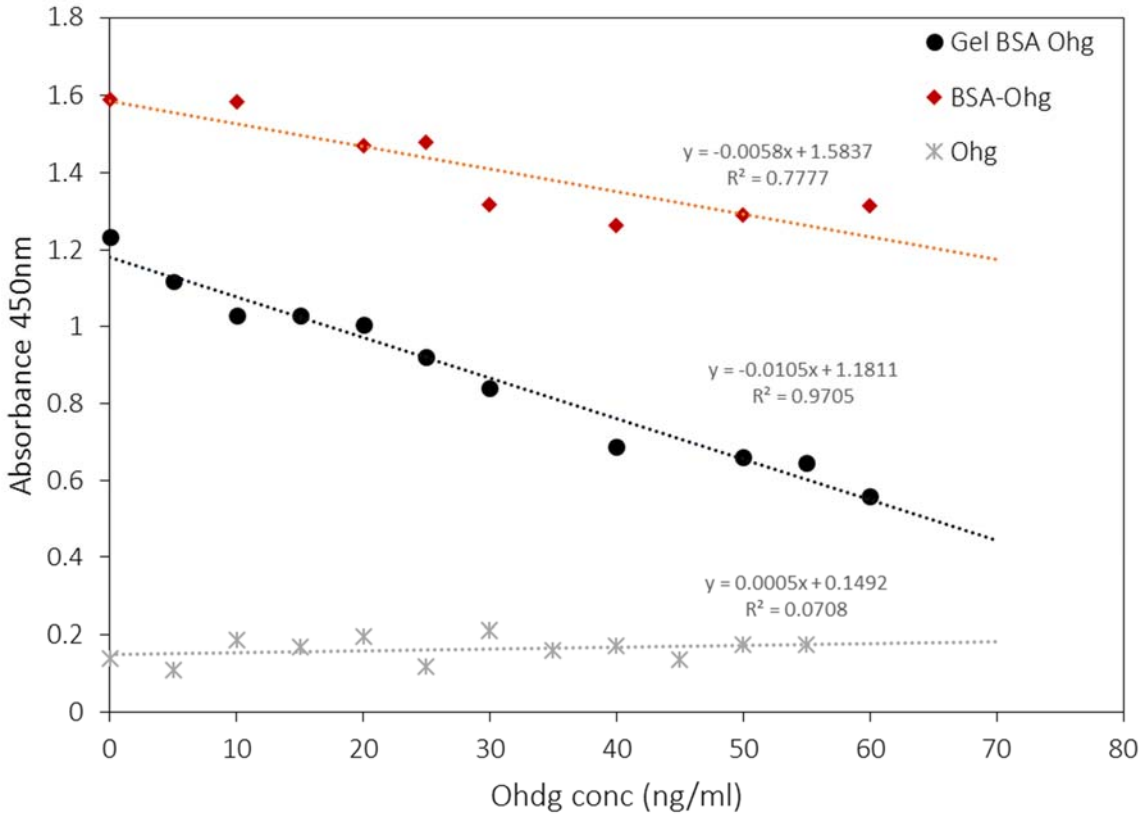

Figure 65 Standard curve of competitive ELISA with Gel-BSA-OHG, BSA-OHG and OHG

3.3.5 Detection of 8-OHdG using Gel-BSA-OHG

Competitive ELISA was performed to evaluate the efficiency of Gel-BSA-OHG to detect OHDG in varying concentrations. Two different ELISA experiments were performed. For the first experiment, anti 8-OHdG conjugated with gold nanocluster(fAuNC-Antibody) was used for testing while in the second experiment 1 μg/ml anti-8-OHdG antibody was used for testing. Gel-BSA-OHG was coated on the plate with varying concentrations on a 96 well plate followed by incubation with fAuNC-Antibody with varying concentrations of OHDG. Addition of Secondary IgG with HRP enzyme and its subsequent reaction with the TMB substrate established the varying color intensity of the wells depending on the concentration of the Gel-BSA-OHG and 8-OHdG (Figure 66). The experiment was repeated with 1 μg/ml anti-8-OHdG antibody (Figure 67) at different concentrations. The experiments suggested that fAuNC-Antibody has a high affinity towards 8-OHdG in the solution and is comparable to the binding affinity of anti-8-OHdG antibody. The signal intensity for fAuNC-Antibody increased with decreasing 8-OHdG concentration

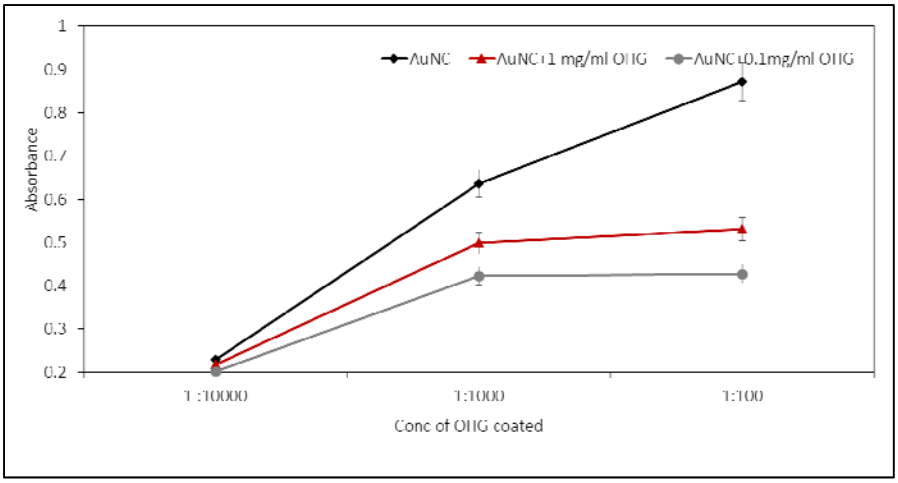

Figure 66 Competitive ELISA with Fluorescent gold nanoclusters and 8-OHdG solution in varying concentrations

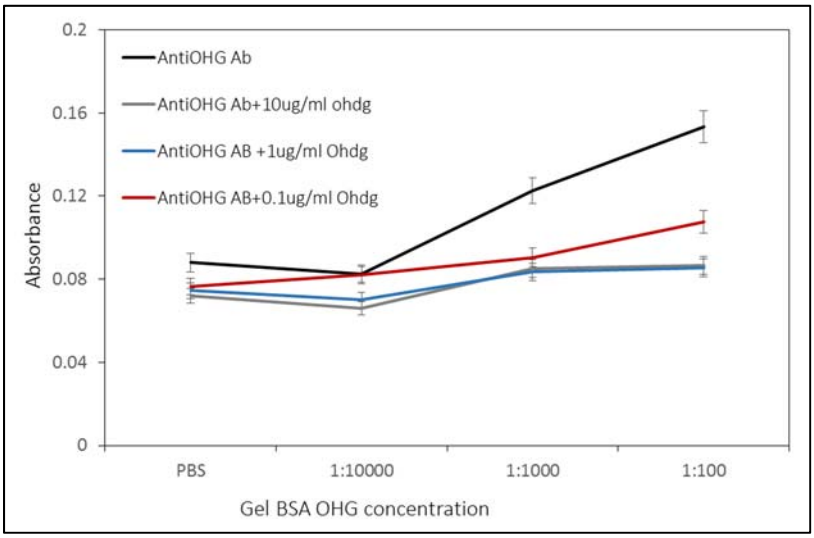

Figure 67 Competitive ELISA graphs with anti-8-OHdG antibody with varying 8-OHdg concentrations

From the above graphs we established that Gel-BSA-OHG can be used as a substrate for the detection of OHdG with a detection limit of 0.001mg/ml of 8-OHdG.

3.3.6 Monolayer vs Multilayer coating

The concentration and volume of Gel-BSA-OHG plays a crucial role in the efficient detection of 8-OHdG. Two different experiments were conducted to determine the concentration and volume of the Gel-BSA-OHG for the maximum efficiency of 8-OHdG detection. In one experiment a monolayer coating of Gel-BSA–OHDG (60µl) was added for the competitive ELISA experiment while in the second experiment a multilayer coating (100µl) of Gel-BSA-OHG was used and 8-OHdG was detected (Figure 68). From the ELISA plot, it is clear that monolayer coating of Gel-BSA-OHG results in a more uniform standard curve compared to multilayer and is suitable for 8-OHdG detection. ELISA experiments were repeated with a 1µg/ml concentration of the Gel-BSA-OHG , and compared with a standard ELISA kit with BSA-OHG substrate which is commercially available. The standard curves of the Gel-BSA-OHG substrate had a more linear trend as compared to the commercially available JAICA kit. We concluded that GEL-BSA-OHG at a concentration of 1 µg/ml could be used a robust substrate for the competitive ELISA.

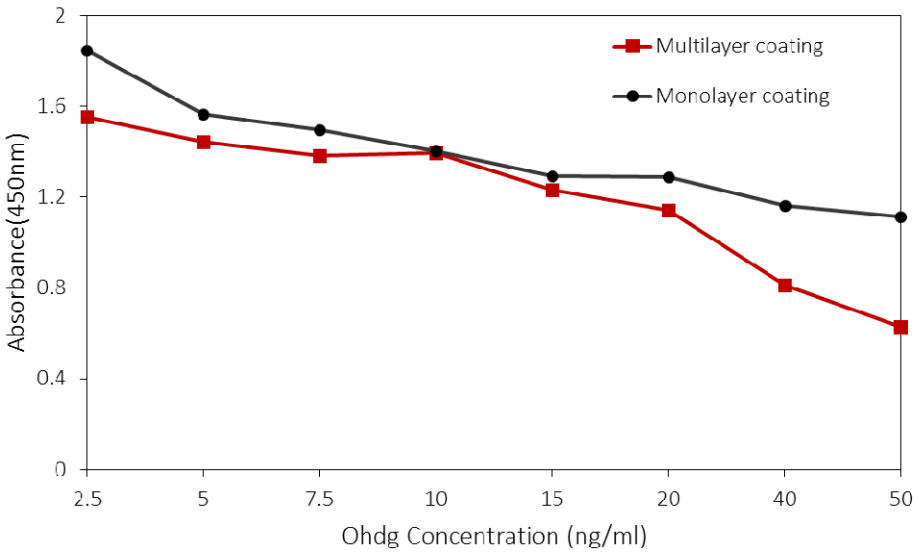

Figure 68 Competitive ELISA graphs of Multilayer vs. Monolayer coating of Gel-BSA-OHG with anti-8-OHdG antibody

3.3.7 Interference Studies

The human urine is composed of several components like urea, sodium, potassium, creatinine and other dissolved ions. The Gel-BSA-OHG and Au-anti-8-OHdG conjugate should not have any interference with the other components of the urine and should be able to detect only the amount of 8-OHdG present in the sample. Competitive ELISA was performed on a 96 well plate with Gel-BSA-OHG as the substrate and varying concentrations of 8-OHdG was added to the artificial urine sample. ELISA results demonstrated that the colorimetric intensity decreased with increasing 8-OHdG concentrations, validating the utility of the substrate (Figure 69 a, 69 b).

a) 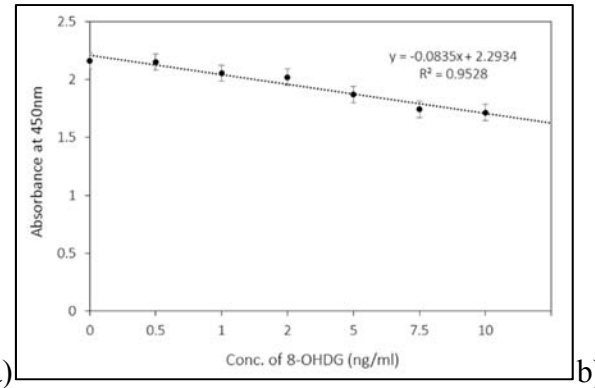

b) 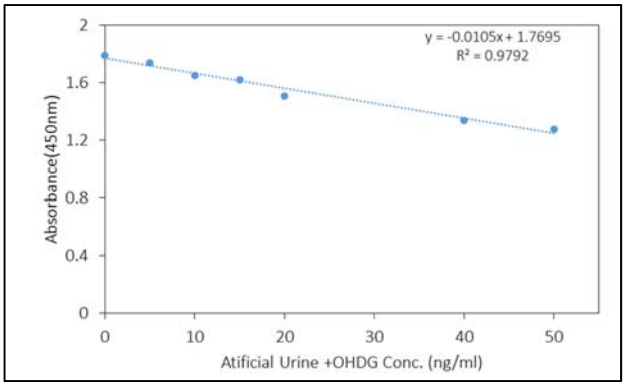

Figure 69 a) ELISA with 8-OHdG in PBS b) ELISA with 8-OHdG in Artificial Urine

3.3.8 Paper strip assay (LFIA)

The paper strip assay was assembled on a nitrocellulose membrane. The conjugate pad was coated with Au-antiOHdG. The test pad was coated with Gel-BSA-OHG substrate and the control pad was coated with Anti mouse IgG (secondary antibody). The paper strip which was 3 mm wide and 6 cm long was used as a dip sensor. The paper strip was dipped in OHDG solution of varying concentrations and the colorimetric intensity of the test line was captured using a smartphone(X. Zhu et al., 2014). The images obtained were analyzed using ImageJ software. The intensity of the test line decreased with increasing concentration of the 8-OHdG concentrations. The intensity of the test lines was normalized with the background intensity of the nitrocellulose membrane for all the images. The color of the test line started to appear within 1 hour of the initiation of the experiment (Figure 70). A test was conducted to confirm that the strip does not react with other components of the human urine. The strips were dipped in artificial urine added with varying concentration of 8-OHdG and the intensity of the test line was captured through a smartphone camera and the images were analyzed through ImageJ software. The strips did not seem to interfere with any of the other components of the artificial urine and exhibited a decreasing intensity with increasing 8-OHdG concentrations. There was 99% correlation between ELISA studies with PBS and artificial urine (Figure 71).

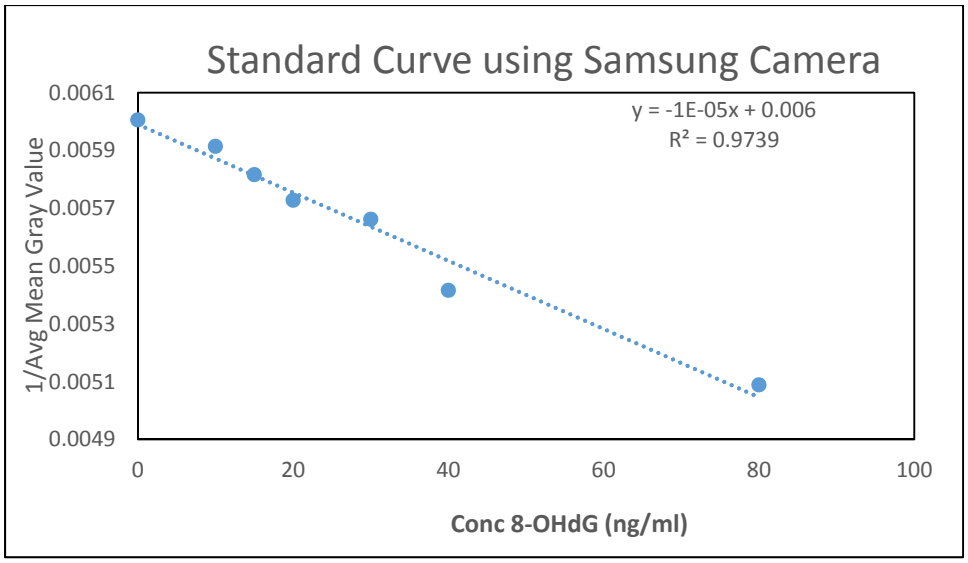

Figure 70 8-OHdG analysis with LFIA (Standard curve)

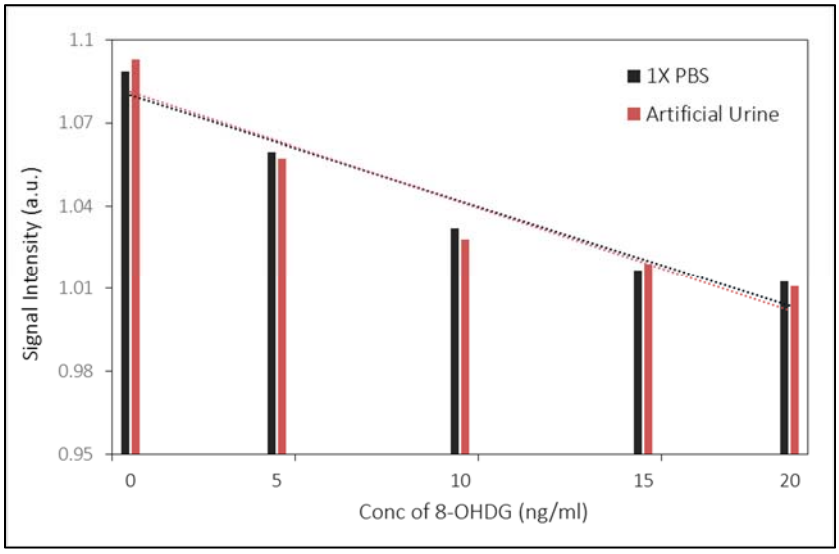

Figure 71 Interference studies with Artificial Urine for LFIA based paper assay

3.3.9 Analysis of Clinical Urine samples

Urine samples were collected from patients with known history of diabetes from the Mason Eye Institute at the University of Missouri, Columbia. Samples were collected with patients who were diagnosed with DR with Fundus examination and from patients who did not DR. The urine

samples were collected during the day and were stored in -20ºC till they were analyzed. The 8-OHdG level in the urine samples was analyzed using 96 well competitive ELISA as well as lateral flow based paper strip assay. Standard curves with known 8-OHdG concentrations were used as control. The values of the 8-OHdG were normalized with creatinine levels in the urine. The 8-OHdG (ng/ml) values and creatinine (mg/dl) values of the patients were correlated with the Fundus result of the patient. The distribution of the 8-OHdG values of the patients showed around 65% correlation with the Fundus results (Figure 72 a). However, there was negligible correlation (20%) with creatinine values of patients with the DR status of the patients (Figure 72 b).The 8-OHdG/creatinine values as obtained by competitive ELISA were correlated with the fundus results. A student t-test was performed to compare the differences between the values of 8-OHDG of patients with and without DR and the average p value was found to be $p<0.01$ indicating good correlation. The average values of 8-OHdG in patients with DR was higher than that in the patients with no DR with a correlation with the Fundus results of about 80% (Figure 73). The urine samples were also analyzed using LFIA paper sensor. The distribution of 8-OHdG/creatinine values was higher in patients with DR as compared to patients with no DR (Figure 74). The 8-OHdG/creatinine values were correlated with the Fundus results as well as with the ELISA results. There was around 85% correlation of the LFIA results with the Fundus results, while there was around 80% correlation of the LFIA results with the ELISA results. The individual Fundus images of the patients with and without DR were matched with the 8-OHdG values for some patients (Figure 75). Around 6 outliers were observed. Thus, based on our studies, the cut off value for 8-OHdG/ creatinine values for the onset of DR is approximately 35-45 ng/ml which corroborates with the clinical study performed in Asian population.(Hinokio et al., 2002) This is a combined cut off value for both men and women.

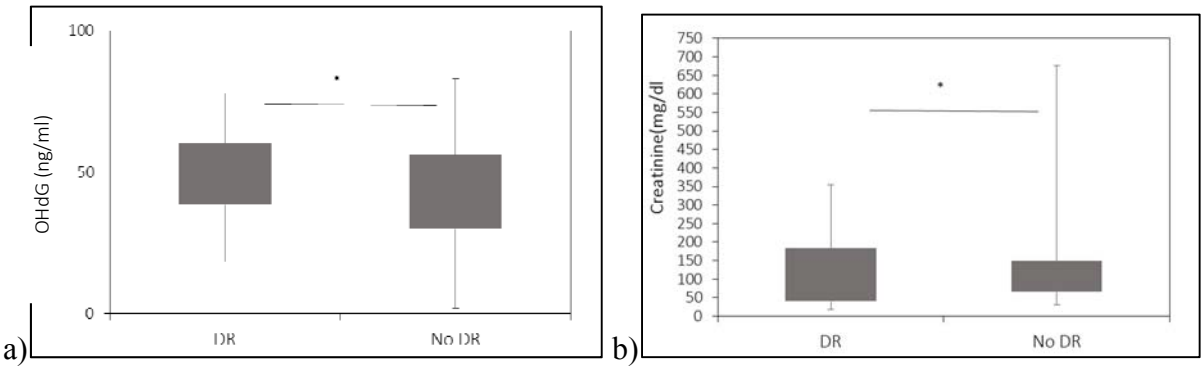

Figure 72 Distribution of a) 8-OHdG (ng/ml) values for Patients with and without DR b) Creatinine (mg/dl) values for patients with and without DR

Figure 73 Distribution of 8-OHdG/creatinine values of patients with and without DR as analyzed by competitive ELISA assay

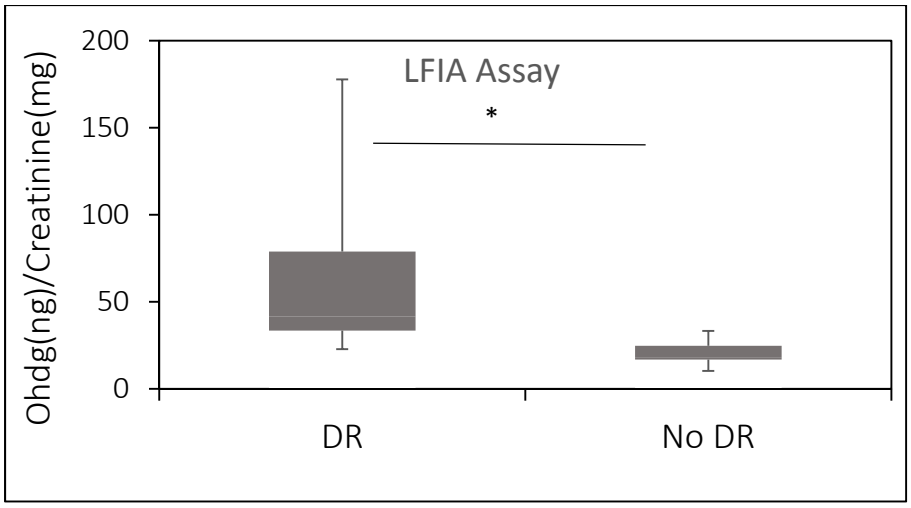

Figure 74 Distribution of 8-OHdG/Creatinine values in patients with and without DR as measured by LFIA

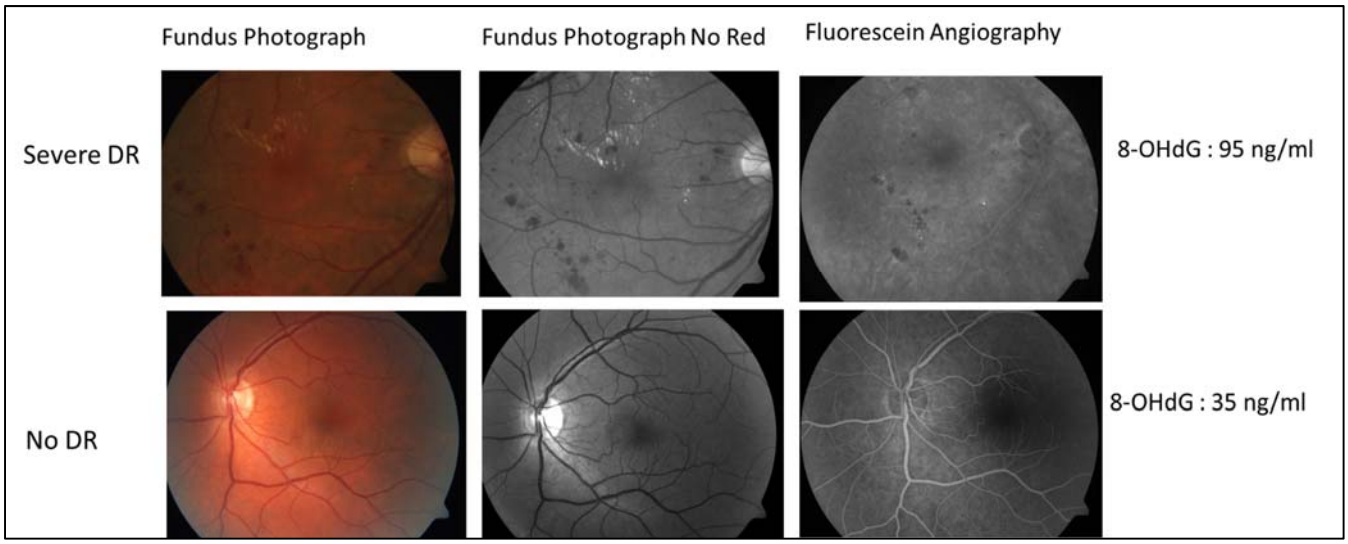

Figure 75 Fundus Images of patients with and without DR

3.4 Conclusion

Diabetic Retinopathy is a microvascular complication of DM which affects the retina and is the leading cause of blindness among adults worldwide. DR is an asymptomatic disease, and the symptoms of the disease appear only after the disease has reached advanced stages. The current

method of diagnosing DR is Fundus photography or Fluorescein angiography. However, the symptoms indicate that the retinal damage has been developing over several years. The incidence and severity of DR can be controlled if there is regular screening of the patients. It is thus crucial to identify a biomarker that can be correlated with the onset of DR. Hyperglycemia causes the activation of several metabolic pathways in the retinal cells which leads to production of Reactive oxygen species (ROS) that leads to oxidative stress. The ROS produced in the cells enters the mitochondria and causes mitochondrial dysfunction which causes the guanine base pair in the mitochondrial DNA to oxidize to hydroxyl groups (8-OHdG). The cells remove the DNA lesion which is then secreted to the blood and finally to urine. Thus, urinary 8-OHdG is marker of the extent of DNA damage in the body. Since, retina is the region of highest metabolic activity, it is considered that the amount of 8-OHdG in the urine will be indicative of the extent of damage in the retina in a patient with DR. We hypothesized that the amount of urinary 8-OHdG will be higher in patients with DR than with patients with no DR. To prove our hypothesis we conducted a two tiered study. First we developed a Gelatin-BSA-OHG substrate and Au-antiOHdG against 8-OHdG substrate for competitive ELISA and LFIA. We then tested the specificity and detection limit of the 8-OHdG for each of the sensors. Interference and proof of principle studies were conducted with artificial urine and varying concentrations of 8-OHdG. We collected urine samples from patients with or without DR from the Mason Eye Institute at University of Missouri (n=80) and performed these assays. 8-OHdG levels were quantified with competitive ELISA and LFIA methods. The DR status of the patients was confirmed. The results suggest that 8-OHdG levels are higher in patients with DR than with no DR and 8-OHdG can be explored as screening biomarker for the onset of DR

References

Afrasiabi, Z., Shukla, R., Chanda, N., Bhaskaran, S., Upendran, A., Zambre, A., . . . Kannan, R. (2010). Nanoscale Sensor Design via <I>In Situ</I> Labeling of Gold Nanoparticles onto Protein Scaffolds. *Journal of Nanoscience and Nanotechnology, 10*(2), 719-725. doi:10.1166/jnn.2010.1906

Chiou, C.-C., Chang, P.-Y., Chan, E.-C., Wu, T.-L., Tsao, K.-C., & Wu, J. T. (2003). Urinary 8-hydroxydeoxyguanosine and its analogs as DNA marker of oxidative stress: development of an ELISA and measurement in both bladder and prostate cancers. *Clinica Chimica Acta, 334*(1-2), 87-94. doi:10.1016/s0009-8981(03)00191-8

Coester, C. J., Langer, K., van Briesen, H., & Kreuter, J. (2000). Gelatin nanoparticles by two step desolvation--a new preparation method, surface modifications and cell uptake. *J Microencapsul, 17*(2), 187-193. doi:10.1080/026520400288427

Cunha-Vaz, J. G., & World, S. (2011). *Diabetic retinopathy*. Singapore; Hackensack, N.J: World Scientific Pub. Co.

Eshaq, R. S., Aldalati, A. M. Z., Alexander, J. S., & Harris, N. R. (2017). Diabetic retinopathy: Breaking the barrier. *Pathophysiology, 24*(4), 229-241. doi:10.1016/j.pathophys.2017.07.001

Forrester, J. V. (2002). *The eye : basic sciences in practice*. Edinburgh: W.B. Saunders.

Hinokio, Y., Suzuki, S., Hirai, M., Suzuki, C., Suzuki, M., & Toyota, T. (2002). Urinary excretion of 8-oxo-7, 8-dihydro-2'-deoxyguanosine as a predictor of the development of diabetic nephropathy. *Diabetologia, 45*(6), 877-882. doi:10.1007/s00125-002-0831-8

Kowluru, R. A., Kowluru, A., Mishra, M., & Kumar, B. (2015). Oxidative stress and epigenetic modifications in the pathogenesis of diabetic retinopathy. *Prog Retin Eye Res, 48*, 40-61. doi:10.1016/j.preteyeres.2015.05.001

Kowluru, R. A., & Mishra, M. (2015). Oxidative stress, mitochondrial damage and diabetic retinopathy. *Biochimica et Biophysica Acta (BBA) - Molecular Basis of Disease, 1852*(11), 2474-2483. doi:10.1016/j.bbadis.2015.08.001

Lechner, J., O'Leary, O. E., & Stitt, A. W. (2017). The pathology associated with diabetic retinopathy. *Vision Res*. doi:10.1016/j.visres.2017.04.003

Madsen-Bouterse, S. A., & Kowluru, R. A. (2008). Oxidative stress and diabetic retinopathy: pathophysiological mechanisms and treatment perspectives. *Rev Endocr Metab Disord, 9*(4), 315-327. doi:10.1007/s11154-008-9090-4

Naidu, B. V. K., & Paulson, A. T. (2011). A new method for the preparation of gelatin nanoparticles: Encapsulation and drug release characteristics. *Journal of Applied Polymer Science, 121*(6), 3495-3500. doi:10.1002/app.34171

Pickup, J. C., & Williams, G. (1994). *Chronic complications of diabetes*. Oxford; Boston: Blackwell Scientific Publications.

Safi, S. Z., Qvist, R., Kumar, S., Batumalaie, K., & Ismail, I. S. (2014). Molecular mechanisms of diabetic retinopathy, general preventive strategies, and novel therapeutic targets. *Biomed Res Int, 2014*, 801269. doi:10.1155/2014/801269

Santella, R. M. (1999). Immunological methods for detection of carcinogen-DNA damage in humans. *Cancer Epidemiol Biomarkers Prev, 8*(9), 733-739.

Shang, L., Dong, S., & Nienhaus, G. U. (2011). Ultra-small fluorescent metal nanoclusters: Synthesis and biological applications. *Nano Today, 6*(4), 401-418. doi:10.1016/j.nantod.2011.06.004

Srikar, R., Suresh, D., Zambre, A., Taylor, K., Chapman, S., Leevy, M., . . . Kannan, R. (2016). Targeted nanoconjugate co-delivering siRNA and tyrosine kinase inhibitor to KRAS mutant NSCLC dissociates GAB1-SHP2 post oncogene knockdown. *Scientific Reports, 6*(1). doi:10.1038/srep30245

Wu, L. L., Chiou, C. C., Chang, P. Y., & Wu, J. T. (2004). Urinary 8-OHdG: a marker of oxidative stress to DNA and a risk factor for cancer, atherosclerosis and diabetics. *Clin Chim Acta, 339*(1-2), 1-9.

Xie, J., Zheng, Y., & Ying, J. Y. (2009). Protein-Directed Synthesis of Highly Fluorescent Gold Nanoclusters. *Journal of the American Chemical Society, 131*(3), 888-889. doi:10.1021/ja806804u

Zhu, X., Hondroulis, E., Liu, W., & Li, C.-z. (2013). Biosensing Approaches for Rapid Genotoxicity and Cytotoxicity Assays upon Nanomaterial Exposure. *Small, 9*(9-10), 1821-1830. doi:10.1002/smll.201201593

Zhu, X., Shah, P., Stoff, S., Liu, H., & Li, C. Z. (2014). A paper electrode integrated lateral flow immunosensor for quantitative analysis of oxidative stress induced DNA damage. *Analyst, 139*(11), 2850-2857. doi:10.1039/c4an00313f

APPENDIX

PART 2: NANOPARTICLES FOR THERAPEUTICS AND DRUG DELIVERY

CHAPTER 4

TARGETED DRUG DELIVERY FOR BREAST CANCER CELLS

4.1 Introduction

4.1.1 Breast Cancer

Breast cancer is one of the major cancers affecting women worldwide. It was reported that there were around 246,660 new cases of breast cancer in 2016 (Breast cancer facts and figures, ACA, 2016). It is the primary cause of death amongst women with cancer (Eccles et al, 2013). Breast cancer has currently become a global health concern. In the past few decades, several treatment procedures and chemotherapy drugs have been developed to combat the malignancy of the disease. As a result there has been a significant improvement in the cancer survival rate among patients (Weigel et al, 2010). The most commonly used chemotherapy drugs are Methotrexate, Doxorubicin, Paclitaxel, 5-fluorouracil and Gemcitabine (Singh et al, 2017). However, in spite of advances in drug therapy, 14% of the all the cancer deaths in the USA in the year 2016 were attributed to breast cancer (Singh et al, 2017). The main causes of death due to breast cancer are drug resistance, metastasis and toxic side effects of the chemotherapy drugs. The major limitations of the cytotoxic chemotherapy are high toxicity, rapid elimination from the circulatory system and accumulation in non-targeted tissues or organs. (Kumari et al, 2015)) Target specificity of cancer drugs is thus essential for effective cancer treatment. To this effect, different drug carrier and delivery systems have been studied to improve the drug delivery

efficiency. Nanoparticles and Nano-scaled can potentially improve delivery of drugs into the cells through the EPR (Enhanced permeability and retention) effect and protect the therapeutic agents from being degraded in the biological system (Singh et al, 2017)

4.1.2 Drug Delivery Systems in Chemotherapy

Conventional chemotherapy drugs have poor aqueous solubility and have large pharmacokinetic volume of distribution. In addition, they have lower retention rates in the system and lack specificity of targeting. Some of the issues of conventional chemotherapy drugs can be circumvented by using nanoparticles or Nano scaled drug carriers (Kumari et al, 2015). The nano scale size of these carriers renders them with larger surface to volume ratios which increases surface functionalization efficiency and also plays a crucial role in bio distribution in vivo. The most commonly used drug carriers are categorized as protein based, organometallic, nucleic acid and liposome based (Bahrami et al, 2017). The protein based carriers generally include albumin, gelatin, and other polymeric nanoparticles. The organometallic carriers primarily comprise gold and magnetic nanoparticles. The nanoparticles offer several advantages over conventional chemotherapy systems. They enhance the therapeutic index of the chemotherapeutic agents and improve drug efficacy by extending the half-life of the drug and increasing the time of circulation in the system. They also enable controlled release of the drugs and can be conjugated with a molecule that can specifically bind to certain receptors, thereby increasing target specific drug delivery in the cells and reducing non-specific drug toxicity (Kumari et al, 2015). In addition, metallic nanoparticles have certain optical, physical and electromagnetic properties which enable them to be imaged in vivo without the need of any fluorescent labels. The magnetic nanoparticles have unique magnetic nanoparticles which enable

them to be imaged using MRI (Magnetic resonance imaging) and gold nanoparticles can be imaged using PET (Position emitted tomography) scan (Choi et al,2004).

4.1.3 Hypothesis and Proposed Drug Delivery system

There are several chemotherapy drugs that are currently being used for breast cancer. Methotrexate is a common drug that was initially used to treat rheumatoid arthritis (Hall et al,2017). However, in the recent years Methotrexate has also been widely used to treat breast cancer, head and neck carcinoma and certain types of leukemia (Sanyog, 2012), It is an anti-metabolite i.e. it affects or blocks the de novo synthesis cycle of the cells which produces pyrimidine and purines essential for cell growth and proliferation. Conventionally, methotrexate is administered orally or intramuscularly. The uptake of methotrexate in the cells is mediated by a saturable transporter called RFC 1 (Reduced Folate carrier) (Ceonstein, 2007). Methotrexate has been reported to accumulate in the extravascular pool. Methotrexate has a short half-life of around 6-8 hours and does not have any detectable traces in the serum after 24 hours. Part of the methotrexate absorbed by the cells is converted to 7-hydroxymethotrexate, which in turn are converted to Methotrexate polyglutamates (MTX_{Glu}). $MTX_{Glu\ are}$ stored in liver tissues and erythrocytes. The efficacy of the drug is dependent on the concentration of MTX_{Glu} in the tissues (Ceonstein, 2007).

4.1.3.1 Mechanism of action of Methotrexate

Methotrexate is a folic acid antagonist. It inhibits several key enzymes like dihydrofolate reductase (DHFR) that are responsible for the synthesis of purine and pyrimidines (8). Blocking of the DHFR results in decrease in tetrahydrofolate (THF) levels which leads to reduced DNA methylation, inhibition of Thymidylate Synthase (TS) and disrupts DNA synthesis in the cells.

Mtx also blocks the 5-aminoimidazole-4-carboxamideri ribonucleotide (AICAR) tranformylase which inhibits the de novo purine synthesis (Wilson et al, 2014).

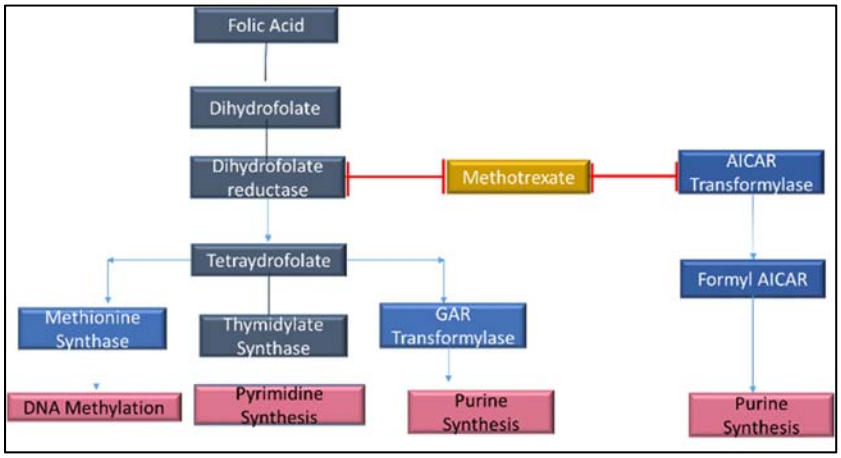

Figure 1 Schematic of mechanism of purine/pyrimidine blocking pathway of Methotrexate

Methotrexate blocks the purine and pyrimidine synthesis of DNA in cells. It arrests the cell development in the S phase of the cell cycle and induces apoptosis of the cells. In addition to blocking the purine/pyrimidine synthesis, few reports have shown that methotrexate downregulates the JAK/STAT pathway in certain melanoma cells. JAK/STAT is a cell proliferation promoting pathway which is upregulated in a cancer cell. When methotrexate is uptaken by the cell, it is hypothesized that it down regulates the JAK/STAT pathway and in the process starts a cascade of pathways which also induce apoptosis (Thomas et al, 2015).

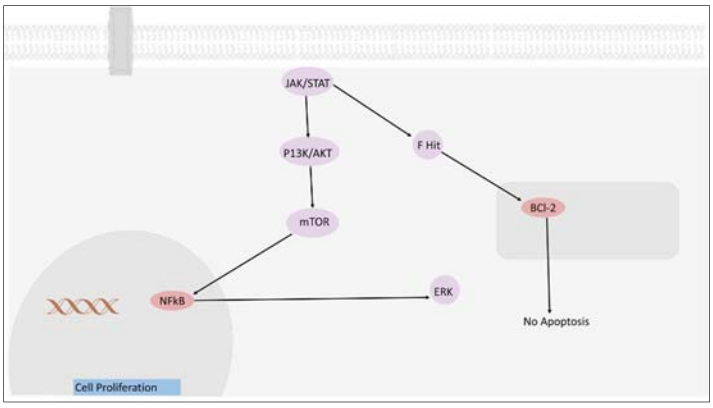

Figure 2 Molecular pathways in a cancerous cell line before methotrexate treatment

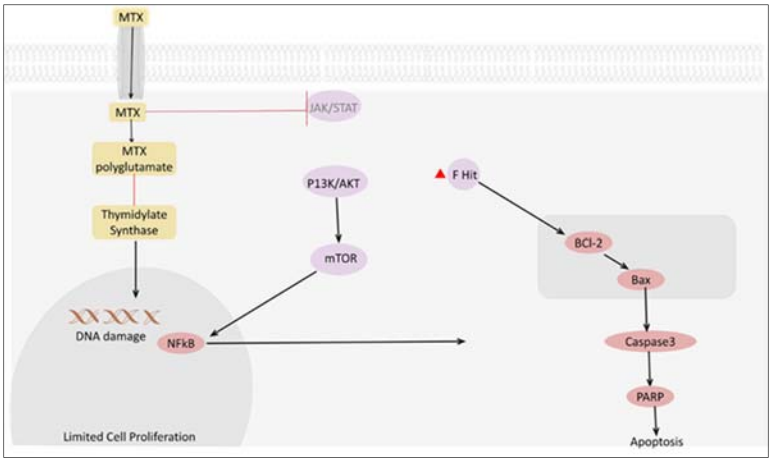

Figure 3 Molecular mechanisms in cancer cells after methotrexate treatment

Methotrexate suffers from certain limitations which include the short half-life of the drug, rapid diffusion through the body and harmful side effects due to uniform tissue distribution (Bostik, 1988).

It has been reported clinically that the side effects of the methotrexate can be alleviated by administering folic acid which competes with methotrexate for the same transporter (RFC1). Folic acid is also used as a targeting agent for Folate receptor α expressing cells. Folate receptor α is a glycophosphytidylinositol-anchored, folate binding protein which is overexpressed in some cancerous cells (Ceonstein, 2007) (Jain et al, 2011). It captures the folate or folic acid which captured the folate to enhance cell proliferation in cancerous cells. Thus, folic acid conjugated with methotrexate can be used as a targeting agent to specifically target cells expressing folate receptor α (cancerous cells) to block their proliferative cycle and induce apoptosis. However, due to short half-life of the methotrexate in the system, the effects would not be very significant. The half-life of methotrexate can be increased by conjugating with human serum albumin which has a half-life of about 19 days. Studies have shown that conjugating methotrexate with HSA has increased efficacy and sensitivity (Ulbrich et al, 2011) (Bures, 2011). Thus, a methotrexate HSA conjugate with a folic acid as a targeting agent can be an effective tool for drug delivery. However, it will be difficult to track the path of the drug in the system and to know whether the drug is being delivered to the target tissue or being accumulated in the liver. An imaging modality attached to the drug conjugate will enable real time imaging and tracking of the drug conjugate.

4.1.4 Magnetic nanoparticle based drug delivery system

Magnetic nanoparticles have been reported to have important biomedical applications such as magnetic cell separation, targeted drug delivery, contrast agents for Magnetic Resonance

Imaging (MRI) (Choi et al, 2004). The versatility of the magnetic nanoparticles can be enhanced by coating a metallic shell with different optical and surface properties, on the magnetic nanoparticle. Core-shell magnetic NPs consist of a magnetic core and a metallic shell that provides a hydrophilic layer to the NPS and provides a platform for surface functionalization (Qunito et al, 2015). Gold salts can be reduced on the magnetic core to form a gold shell iron oxide core nanoparticle, which can further be functionalized with thiolated molecules. The core shell magnetic gold nanoparticles have unique physical and surface properties which make them attractive tools for drug delivery in vivo. Due to their large surface to volume ratio, the nanoparticles can be conjugated with drugs and targeting moieties simultaneously. Their optical and magnetic properties enable them to be used for different imaging modalities in vivo, e.g. Magnetic Resonance Imaging, PET scan and Surface Enhanced Raman scattering (SERS) imaging (Blasiak et al, 2013).

Under, normal biological conditions magnetic nanoparticles do not exhibit magnetic properties towards each other. In an MRI scanner, when an external magnetic field is applied, the magnetic particles attain magnetic saturation, creating a dipolar field which leads to a significant reduction of proton relaxation (T_2 relaxation) resulting in a much darker image of the target area over the biological background. These properties of the nanoparticle can thus be utilized to for imaging and following the path of the drug delivery tool (Figure 4) (Frey et al, 2009).

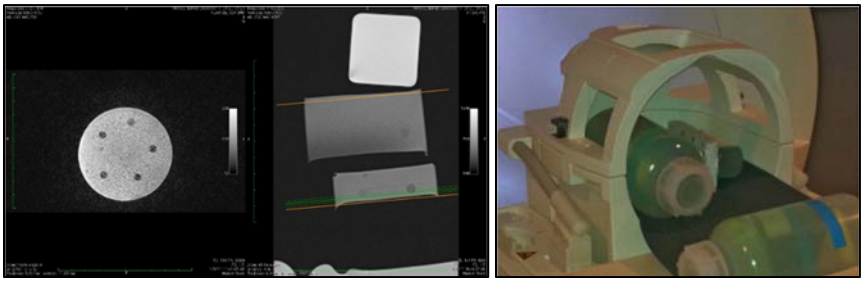

Figure 4 Setup of an MRI scanner in the University of Missouri, School of Veterinary Medicine

Gold nanoparticles exhibit light induced surface plasmon resonance on their surface. As a result of this there are electric field hot spots created on the curves and troughs on the surface of the nanoparticles. Molecules which are near these electric field hot spots will experience enhanced excitation field and emit amplified Raman intensities (Shuming Nie, 2008). Studies have shown that a 10^3 fold enhancement is attainable through SERS. Because of its unique advantages, SERS has become a promising tool in medical application especially for imaging in vivo. SERS can be used for real time imaging of drug delivery in vivo. To further enhance the SERS signals, the nanoparticles are tagged with a dye that emits enhanced signals under certain excitation wavelengths (Kho et al, 2005).

We have conjugated methotrexate to human serum albumin and attached it to folic acid. The methotrexate human serum albumin and folic acid conjugate is attached to gold coated iron oxide nanoparticles to enable monitoring the path of the drug moiety to its target with MRI. The amount of methotrexate released can be monitored using SERS imaging by the dye attached to the gold conjugated iron oxide nanoparticle. Characterization experiments were conducted on the nanoparticle conjugates. SERS and MRI imaging was done on the Au@Fe nanoparticles in vitro. Cytotoxicity and cellular uptake studies were conducted to test the efficacy of the nanoparticle conjugate in breast cancer cell lines.

4.2 Materials and Methods

4.2.1Materials

$FeCl_3.6H_2O$, FeCl2.4H2O, Human Serum Albumin (HSA), Folic Acid (FA), Hydroxysuccinimide (NHS) were purchased from Sigma Aldrich. Tetramethylammonium hydroxide (TMOH) and Tri sodium citrate were purchased from Acros Organics. Hydrochloric acid (HCl), Nitric Acid (HNO_3) and Sodium Hydroxide (NaOH) were purchased from Fisher Scientific. Methotrexate was purchased from ToCris. 1-Ethyl-3dimethylaminopropyl) carbodiimide (EDC) was purchased from Fluka Analytical. DI water was used in all experiments.

4.2.2 Instrumentation

UV Vis absorbance of Au@Fe nanoparticles was measured with Varian CaryUV Spectrophotomer. The UV Vis absorbance of MTX HSA FAwas measured with BioTek Epoch microplate reader and Cytation 3. Zeta Potential and hydrodynamic radius was measured using Malvern Zeta sizer. TEM Images were taken with Jeol 1400 Biological TEM. XRD studies were conducted using FEI Tecnai F30 G2 Twin Microscope. The images were analyzed using ImageJ analysis software. 1D and 2D NMR studies were conducted by Dr. Raj Bhaskaran's group.

4.2.3Synthesis of Fe_3O_4 and γFe_2O_3

The Fe_3O_4 nanoparticles were synthesized in nitrogen atmosphere following previously reported procedure(Deng et al, 2003) . Briefly, 5.2 g of $FeCl_3$ and 2 g of $FeCl_2$ were dissolved in 25ml of

DI water. 0.85ml of 12.1N HCl was added to the solution and stirred vigorously until the Fe salts were dissolved. 250 ml of 1.5M NaOH was added drop wise into the mixture with vigorous stirring, resulting in an initial pale yellow solution which changed to brown and finally to black. The black precipitate was washed twice with H_2O and once with 0.1M TMOH (Tetramethylammonium hydroxide) with magnetic separation. To obtain $\gamma Fe_2 0_3$ nanoparticles, Fe_3O_4 nanoparticles were washed with 0.01M HNO_3 and then dissolved in 0.01M HNO_3 at 90°C with magnetic stirring until complete dissolution. The Fe_3O_4 nanoparticles were separated through magnet and re-suspended in 0.1M TMOH at pH 11 after washing with water.

4.2.4 Synthesis of Au@Fe

Iron oxide nanoparticles were coated with reduced gold nanoparticles (Pham et al, 2008). Sodium citrate was used as the reducing and stabilizing agent. The gold coated iron oxide nanoparticles were prepared according to a previously published procedure with slight modifications. Briefly 1 ml of TMOH stabilized γFe_2O_3 solution was magnetically separated and the pellet was dissolved in 1 ml DI water. The solution was added to 50ml 0.01M sodium citrate solution and stirred for 30 minutes. This is referred to in the paper as the working solution. 5ml of the working solution was added to 40 ml 0.01M sodium citrate solution followed by sonication for 15 minutes. The solution was heated till boiling and 0.01M $HAuCl_4$ was added. The solution was stirred at that temperature for 15 minutes. The color changed to deep red. After 15 minutes the solution was removed from heat and stirring was continued for another 15 minutes till the temperature of the solution reached room temperature. The solution was purified by magnetic separation. HSA was conjugated to Au@Fe NP and the binding has been confirmed. 5 mg of Human Serum Albumin (HSA) in DI water was added to 2 mL of Au@Fe nanoparticle and allowed to stir overnight. Excess HSA was removed from the solution via magnetic separation. The excess HSA in the supernatant and the

pellet were separated and used for Enzyme-linked Immunosorbent Assay (ELISA) to detect the presence of HSA in nanoconjugate. The purified HSA-Au@Fe pellet was characterized by UV-Vis and Zeta potential measurements.

4.2.5 Synthesis of MTX HSA FA Conjugates

10 mg MTX and 10mg Folic Acid was dissolved in 1ml 0.1M NaOH (pH~12) (Stehle G, 1997). 14mg EDC and 50mg NHS was added and the solution was activated by stirring at room temperature for 3 hours. Following MTX and Folic acid activation, 15mg/ml HSA was added and stirred for 1 hour at room temperature. The solution was purified by centrifugation with 10kDa filter at 5000 g for 8 minutes. 10 mg MTX was dissolved in 1ml 0.1M NaOH (pH~12). 7mg EDC and 25 mg NHS was added and the solution was activated in a shaker at 37C for 3 hours. Following MTX and Folic acid activation, 15mg/ml HSA was added and stirred for 1 hour at room temperature. The solution was purified by centrifugation with 10kDa filter at 5000 g for 8 minutes. HSA FA was prepared according to previously published procedure. Briefly Folic acid was dissolved in 1ml 0.1M NaOH solution. 800 µl of the FA solution was taken and 200µl of 11.22mg/ml EDC solution was added. The solution was kept in a thermomixer at 20^{o}C and shaken at 1000rpm for 15 minutes. 15mg/ml HSA solution was added and the mixing was continued for one hour. The solution was passed through 10kDa filter and centrifuged at 5000g for 8 minutes. This purification step was repeated three times.

4.2.6 Conjugation of MTX HAS FA to Au@Fe

MTX-HSA-FA was conjugated to Au@Fe-PEG nanoparticles using EDC-NHS conjugation. 1ml of Au@Fe-PEG was centrifuged at 15,000g and the pellet was dissolved in 200ul of MES buffer. 4mg EDC and 5 mg NHS was

4.2.7 Tryptic digestion of MT HSA FA and peptide mapping

An aliquot (60ug – 4ul) was removed from the original submission and diluted with 16uL 6M urea, 100mM HEPES, pH 8.0 and then digested with trypsin according to our standard protocol. Following digest, the samples were acidified to 1% using formic acid, and 25uL transferred to autosampler vials. The vials were placed in a thermostatted (7C) autosampler. An aliquot (full loop, 18uL) of the sample was loaded onto a C8 trap column (Pepmap100 C8 trap column Dionex/Thermo Scientific). Bound peptides were eluted from this trap column onto a 25cm x 150μm inner-diameter pulled-needle analytical column packed with HxSIL C18 reversed phase resin (Hamilton Co). Peptides were separated and eluted from the analytical column with a continuous gradient of acetonitrile at 400nL/min. The Proxeon Easy nLC system is attached to an LTQ Orbitrap XL mass spectrometer. Initial conditions during trap loading were 5%B (A: 0.1% formic acid in water, B: 99.9% acetonitrile, 0.1% formic acid), followed by 2min at 5%B during trap loading, gradient of 5-20%B over 20min, gradient of 20-30%B over 35min, gradient 30-90%B over 5 min, hold at 90%B for 22min, ramp back to (1min) and hold at initial conditions for 5min. Total run time was 90min. FTMS data were collected (30,000 resolution, 1 microscan, 300-1800m/z, profile) and then each cycle (approximately 3 seconds) the 9-most-abundant peptides (ignore +1 ions, >1000 counts) were selected for MSMS (2m/z mass window, 35% normalized collision energy, centroid). Raw data were copied to the Sorcerer2 IDA (SageN Research) and peak lists prepared using ReAdW. The NCBInr database limited to Human (last

update 2/6/2013, 693,522 entries) was searched with trypsin as enzyme, 2 missed cleavages allowed; carbamidomethyl cysteine as a fixed modification; oxidized methionine, methotrexate, and folic acid as variable modifications; 50ppm mass tolerance.

All search data were examined using Scaffold V3.4.8. All data were filtered based on the following criteria: 5 peptide minimum, 95% confidence on peptide ID, mass error limit of <10ppm, 99.0% confidence on protein ID. Manual analysis of putative modified peptides was conducted to validate modification

4.2.8 MRI Phantom images and solution Images

Transverse relaxation (T2 decay) of Au@Fe-MTX HAS FA, Au@Fe-HSA and Au@Fe was utilized to generate a dark MR image in this study. Upon accumulation in agar matrix Au@Fe typically acts as T2 contrast agent to provide a dark image and the contrast enhancement is proportional to the concentration of Fe in the construct. The samples are inducted in agar balls and placed in decreasing order of concentration clockwise. It is a spin echo sequence that has an 180^{o} inverse pulse applied prior to the SE.

4.2.9 Cell Studies

MDA MB 231 which is a folate receptor α positive cell line and also a TNBC was used as a positive control. MCF7 which has been reported to have low folate receptor α expression was used as negative control. NIH 3T3 was used as a non-cancerous cell line. Cells were grown in RPMI media (ATCC) with Fetal Bovine Serum (Sigma Aldrich) and Gentamycine. The cells were grown in CO_2 incubator with 5% CO_2 and $37^{o}C$

4.2.10 Cytotoxicity Studies (MTT assay)

MDA MB 231, MCF7 cells were sub cultured till they reached 70% confluence. 100µl of the cultured cells was added to each 96 well plates and seeded for 24 hours. After 24 hours, varying concentrations (5µg/ml, 10µg/ml, 25µg/ml and 50µg/ml) of Au@Fe MTX HSA FA, Au@Fe MTX HSA and Au@Fe HSA FA were added to the cell culture and incubated for 24 hours following which 10µl of MTT dye was added. The dye was allowed to incubate for 4 hours or till needle like crystal structures were visible under the microscope. The medium was removed and the crystals were dissolved in DMSO and the absorbance was recorded in a BioTek Epoch Microplate reader and Cytation3 at 570 nm. The absorbance data was collected by Gen5 software and analyzed with MS excel. Experiments were conducted in triplicate for statistically significant results. Similar study was repeated with NIH 3T3 cell lines in custom RPMI media.

4.2.11 Cellular uptake studies

Glass cover slips were added to 6 well plates. 1ml Poly L lysine solution was added directly to the cover slip and was kept at RT for 2 hours. After 2 hours Poly L lysine was removed and the coverslips were dried at RT. MDA MB 231 and MCF7 cells were subcultured and 500µl of the cells were seeded in the wells. The cells were seeded for 24 hours. Au@Fe HSA, Au@Fe MTX HSA FA nanoparticles were incubated for 2 hours and 5 hours in separate experiments. Following nanoparticle incubation, the cover slips were washed with PBS several times. Tween 20 was added to the cover slips for 5 minutes to remove nonspecific binding. Following tween washing the cells were washed with PBS again and fixed with PFA before transferring the cover slips to glass slides for imaging. The slides were stained DAPI nucleus staining dye. To study the receptor specificity

of the nanoparticles, the cells were fixed with PFA and then nanoparticles were incubated for 2 hours and 5 hours. The washing and slide mounting procedure was same as that for live cells.

Cellular uptake studies by blocking folate mediated endocytosis pathway:The cell lines were preincubated with Folic acid and then same process as the cellular uptake studies for live and fixed cells was followed to study the uptake pathway of the nanoparticles.

4.2.12Western Blot

MDA MB 231 cells were seeded in a 6 well plate and treated with Au@Fe-MFH, Au@Fe and Methotrexate for 24 hours. Whole cell lysates were prepared using Triton X 100 lysis buffer with MS-Safe protease and phosphatase cocktail inhibitor (Sigma Aldrich) and protein concentration was equalized with Bicinchoninic acid assay (Sigma Aldrich). Proteins were separated by 4-15% native PAGE (Bio-Rad) and were transferred onto nitrocellulose membranes (Gen Script). The membranes were incubated with Primary antibody overnight at 4^{o}C. The primary antibodies used for this experiment are Jak2, Stat5, Akt, ERK, BCl2, Bax, PARP and nFkB . The antibodies were washed and then incubated with secondary anti Mouse IgG HRP or anti rabbit IgG-HRP and incubated for 2 hours at 37^{o}C. The membranes were washed and imaged on Chemidoc Biorad imaging system. Actin protein levels were used as a control for adequacy of equal protein loading. Protein expression levels were analyzed by densitometry analysis.

4.3 Results and Discussion

4.3.1 Characterization of MTX HSA FA Conjugates

Human Serum Albumin was conjugated to Folic Acid. Methotrexate was also conjugated to Human Serum Albumin by NHS activation separately. Finally Human Serum Albumin was conjugated to Methotrexate and Folic acid through the carboxyl group by EDC and NHS

activation. The MTX HSA FA, MTX HSA and FA HAS conjugates were characterized by measuring the absorbance in UV Vis range, zeta potential and hydrodynamic radius measurements, NMR spectroscopy, Mass spectrometry and Trypsin digestion of the proteins followed by peptide mapping.HSA, Methotrexate (in sodium bicarbonate buffer) and Folic acid (in NaOH solution) show absorbance at 270 nm, 370nm and at around 360nm respectively. The UV Vis graph of HSA FA, MTX HSA and MTX HSA FA showed an absorbance at 270 nm and at 370nm(Figure 5). From the UV Vis graph we could confirm the presence of HSA and FA in HSA FA conjugates. Similarly, we could confirm the presence of Methotrexate and HSA in MTX HSA conjugate. However, since the UV Vis graph of MTX HSA FA also showed a peak at 270nm and 370 nm, we were not able to confirm the presence of both FA and MTX in the MTX HSA FA conjugate.

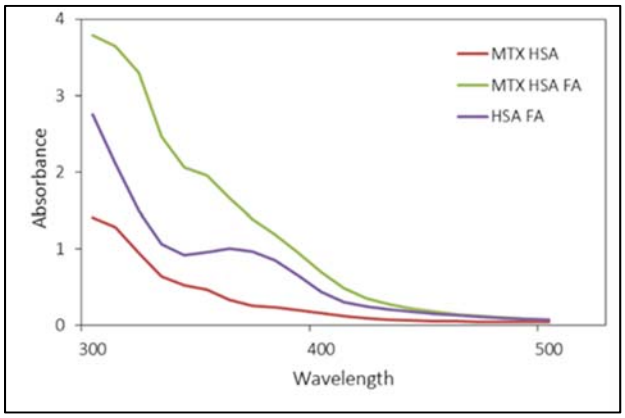

Figure 5 UV-Vis absorbance graph of MTX-HSA-FA conjugates

4.3.2 Trypsin Digestion and Peptide Mapping

To further corroborate the conjugation of MTX and FA to the HSA, Trypsin digestion and peptide mapping experiments were conducted by the DNA core in University of Missouri. The sequence mapping data demonstrated one published MTX site and two unpublished MTX sites. Seven published HSA sites in HSA-FA were found to be modified by FA. In MTX-HSA-FA, two published sites were modified by FA and one was modified by MTX. There were other sites of MTX and both MTX and FA were observed. Hence, from the peptide sequence mapping data, we concluded that both MTX and FA were conjugated to HAS (Figure 6).

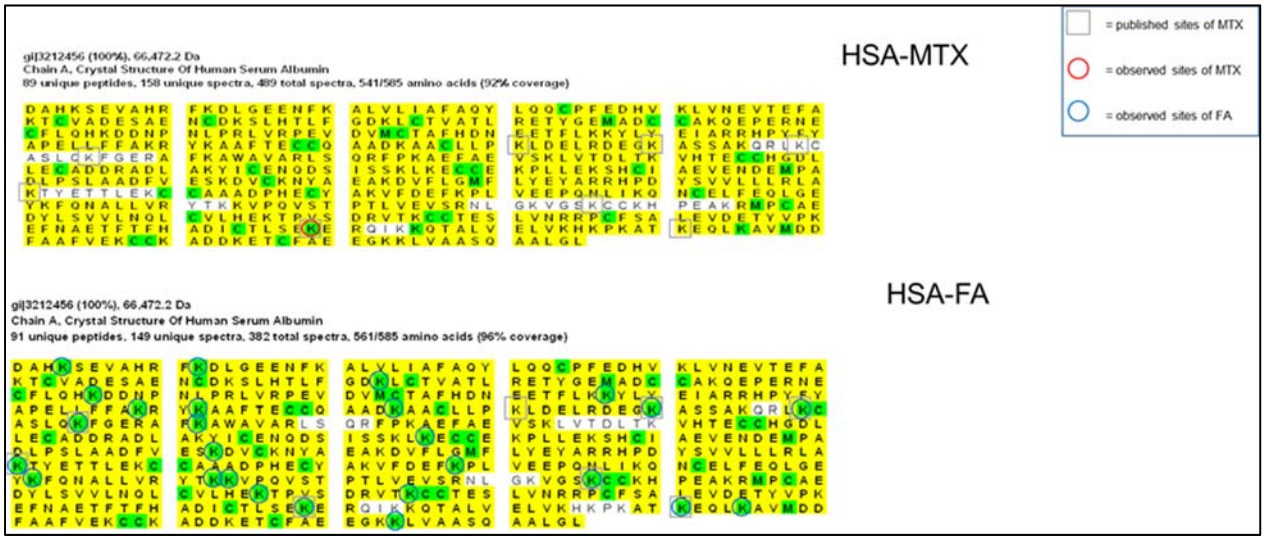

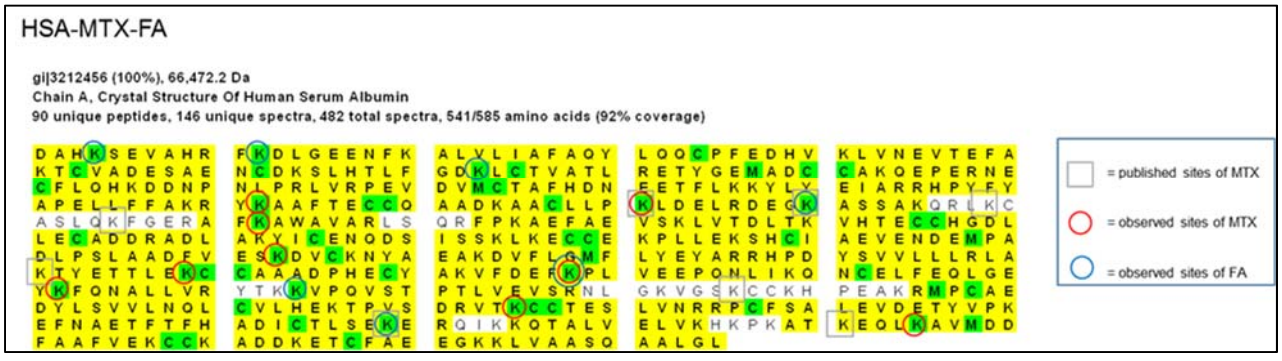

Figure 6 Trypsin digestion and peptide mapping data for published and observed sites of MTX and FA in MTX-HSA, FA-HSA and MTX-HSA-FA conjugates

4.3.3 Characterization of Au@Fe and Au@Fe-MTX-HSA-FA conjugates

Gold conjugated Iron oxide nanoparticles were synthesized using previously published method using sodium citrate as a reducing and stabilizing agent with some modifications. The gold conjugated iron oxide nanoparticles showed a broad peak at 540nm. This result was in agreement with previously published values. The citrate stabilized gold nanoparticles show an absorbance peak at 520 nm. The red shift is because of the increased hydrodynamic radius of the Au@Fe conjugate. The UV Vis graph for Au@Fe MTX HSA FA conjugates showed a broad peak at 540nm along with peaks at 370nm and 270 nm (Figure 7).

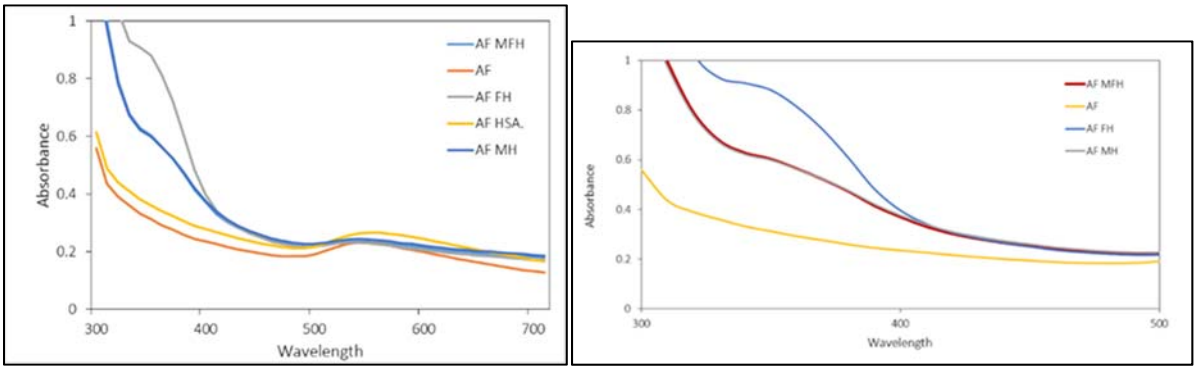

Figure 7 UV absorbance graph of Au@Fe and Au@Fe-MTX-HSA-FA

To determine the stability of the nanoparticles, zeta potential was measured with DTS Nano Zetasizer. Dynamic Light scattering was used to measure the Hydrodynamic radius of the gold conjugated iron oxide nanoparticle. Size and shape of the nanoparticles were confirmed by the images taken by Transmission Electron Microscopy. From the TEM images, we observed the gold particles were layered on the iron oxide nanoparticles forming a sheet like structure. The average diameter of the nanoparticles was 30±5nm (Figure 8) .

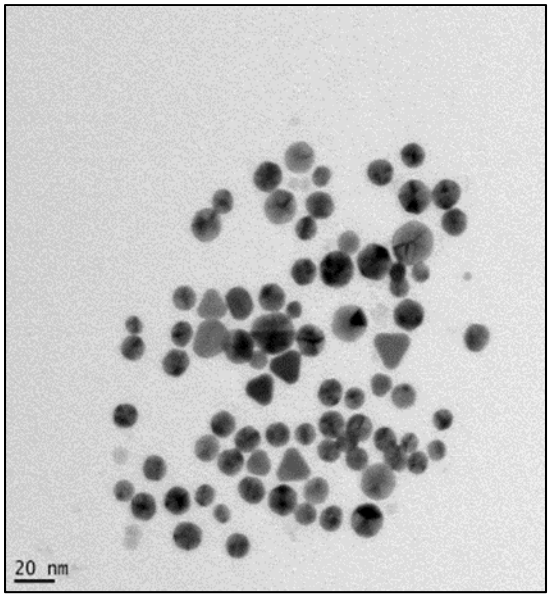

Figure 8 TEM Image of Au@Fe-MTX-HSA-FA conjugate

Atomic absorption spectrometer was used to measure the concentration of gold in the Au@Fe nanoparticle solution. 200 µl of the Au@Fe solution was digested in HCL and HNO_3 solution and the volume was made up to 10ml with DI water. The diluted Au@Fe solution was analyzed under Atomic Absorption Spectroscopy. We estimated the gold concentration to be 20µg/ml of Au@Fe solution.

SERS Imaging:The Au@Fe nanoparticles were functionalized with Thiol -PEG-750 and then coated with Rhodamine B isothiocyanate (SERS reporter dye). The Au@Fe-Peg-Rhodamine B isothiocyanate conjugate was diluted in DIW. The samples were coated on a 76 GA grating. The gratings were analyzed by Reninshaw InVia Raman Microscope. The Au@Fe-Rhodamine conjugate displayed a higher Raman Signal as compared to Au@Fe-Peg nanoparticle.

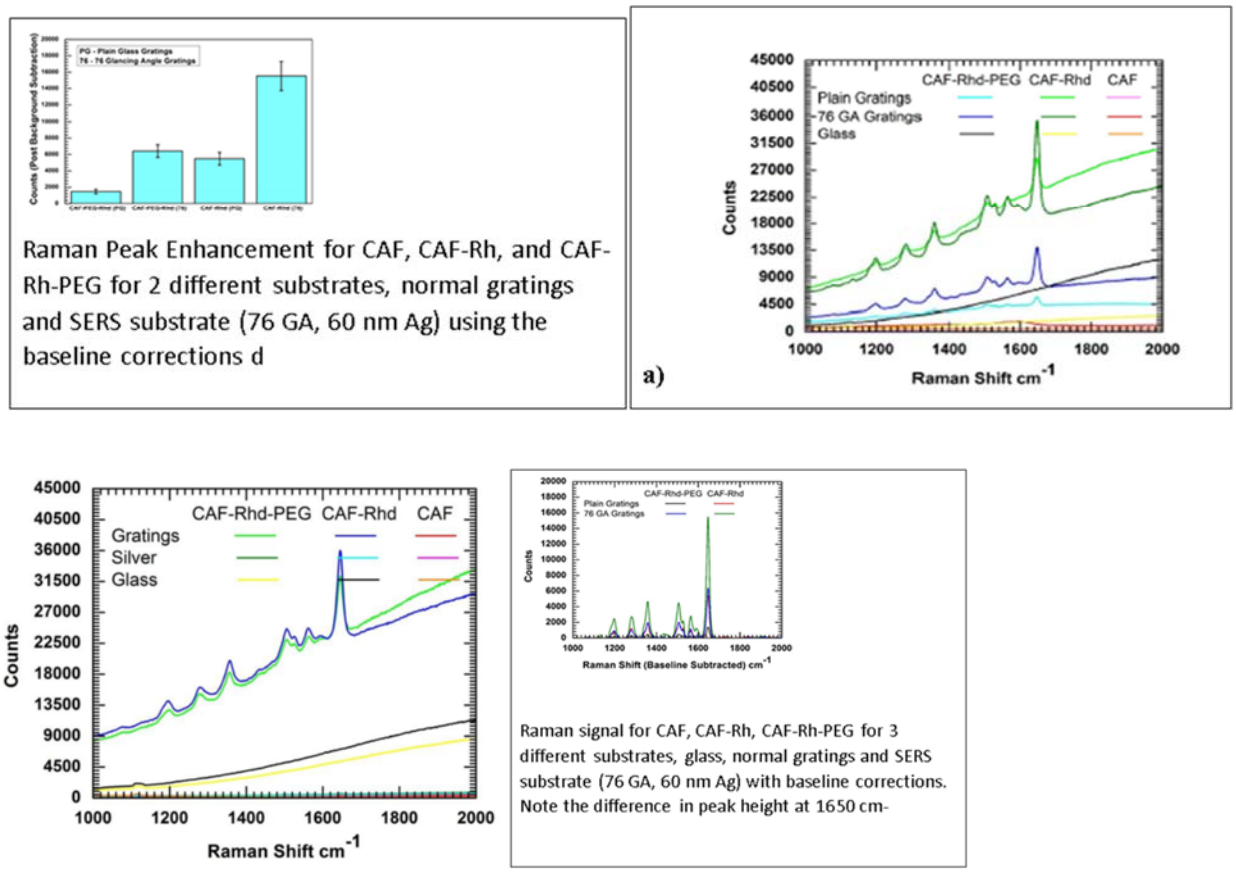

Figure 9 Raman signal for Au@Fe and Au@Fe-Rhodamine B isothiocyanate coated on a glass, silver and 76 GA grating

4.3.4 MRI Imaging

T2 relaxation Images were recorded on MRI scanner. Solutions of Au@Fe at varying concentrations were used for the experiment. The intensity of the images was directly proportional to the concentration of the solution (Figure 10). Phantom Images of the Au@Fe at different concentrations also demonstrate increasing intensity with increasing concentrations. Thus, the Au@Fe nanoparticles can be used as MRI contrast agents even when they are functionalized with surface modification agents.

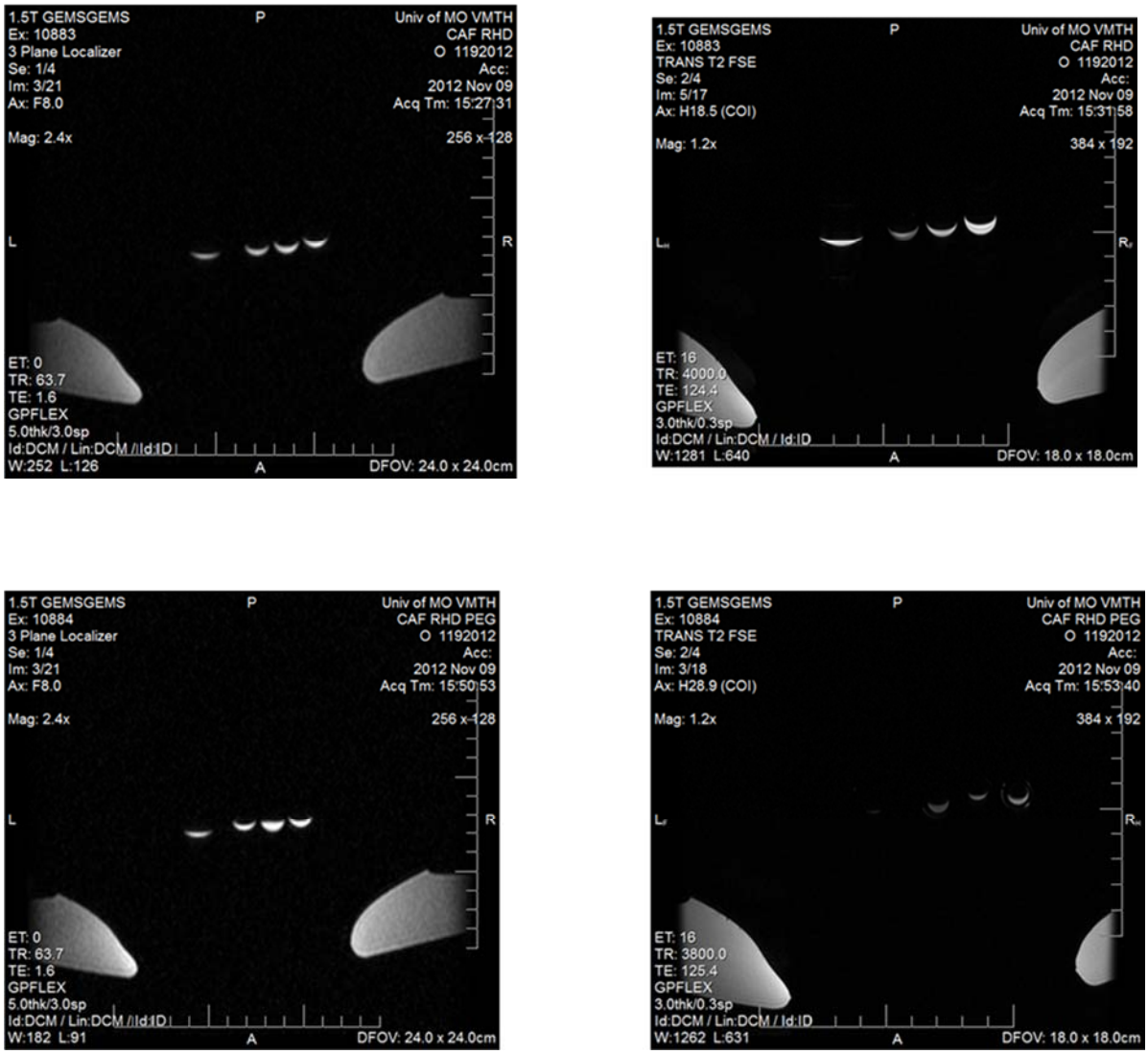

Figure 10 MRI Images of Au@Fe solutions at different concentrations

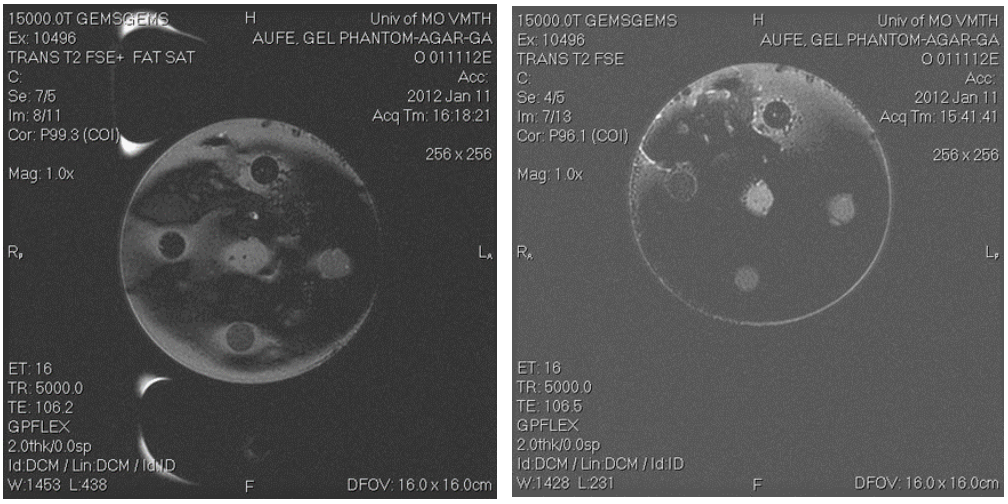

Figure 11 MRI Images of Au@Fe Phantom Gels at different concentrations

4.3.5 Cytotoxicity Assay (MTT Assay)

Cell viability studies were conducted using 4, 5-dimethylthiazol-2-yl)-2, 5-diphenyltetrazolium bromide (MTT) dye. We tested the cytotoxic effects of MTX, Au@Fe MTX-HSA FA, Au@Fe MTX-HSA and Au@Fe on two different cell lines. The IC 50 values for MTX in MCF7 cell line was around 6.25ug/ml while for the AF-MFH conjugate it was 3.125ug/ml. The cell viability decreased consistently with increasing concentration of the drug conjugate. For the MDA MB 231 cell lines, the IC 50 of the cell lines decreased from 6.25ug/ml with the drug to 3.125ug/ml with the Au@Fe-MTX-HSA-FA conjugates.

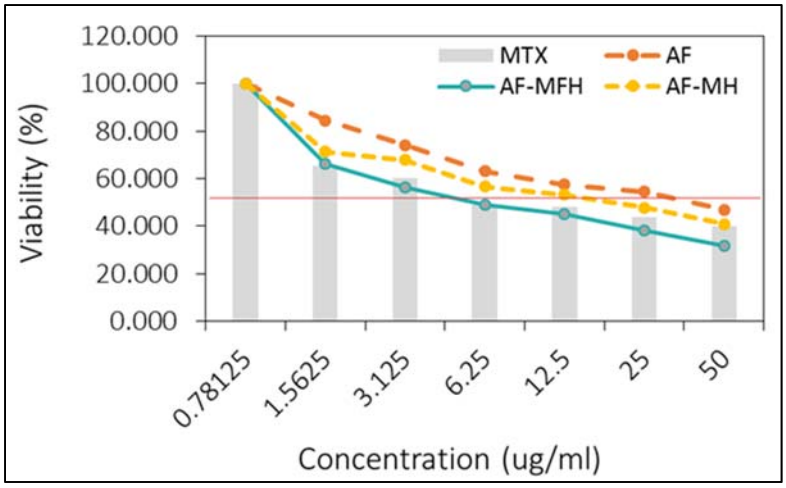

Figure 12 Cytotoxicity assay result of AF-MFH, AF-MH, AF, MTX in MCF7 cell line

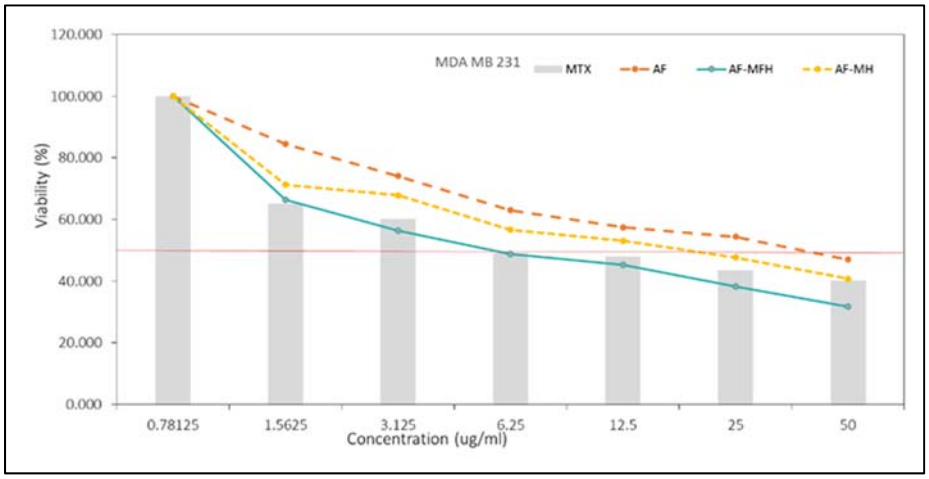

Figure 13 Cytotoxicity assay result of AF-MFH, AF-MH, AF, MTX in MDA MB 231 cell line

4.3.6 Cellular uptake studies (Cytoviva Imaging)

To study the uptake of the nanoparticles in cells, we seeded the cells on a cover slip and incubated the cells with nanoparticles for about 5 hours. The cover slips were stained with DAPI Dye and the slides were observed under a Cytoviva microscope. We noticed increased uptake of

Au@Fe MTX HSA FA and Au@Fe MTX HSA in MCF7 cell line. Not much significant uptake was noticed for Au@Fe HSA nanoparticles.

Au@Fe-MFH

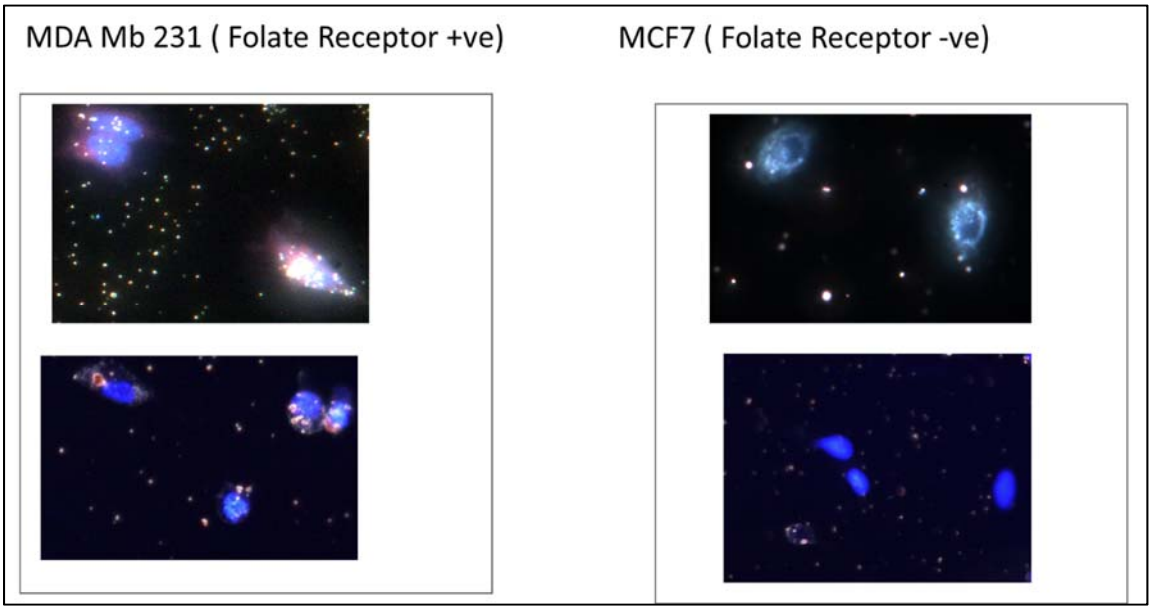

Figure 14 Cellular uptake of AF-MFH in MCF7 and MDA MB 231 cell lines

Au@Fe-MH

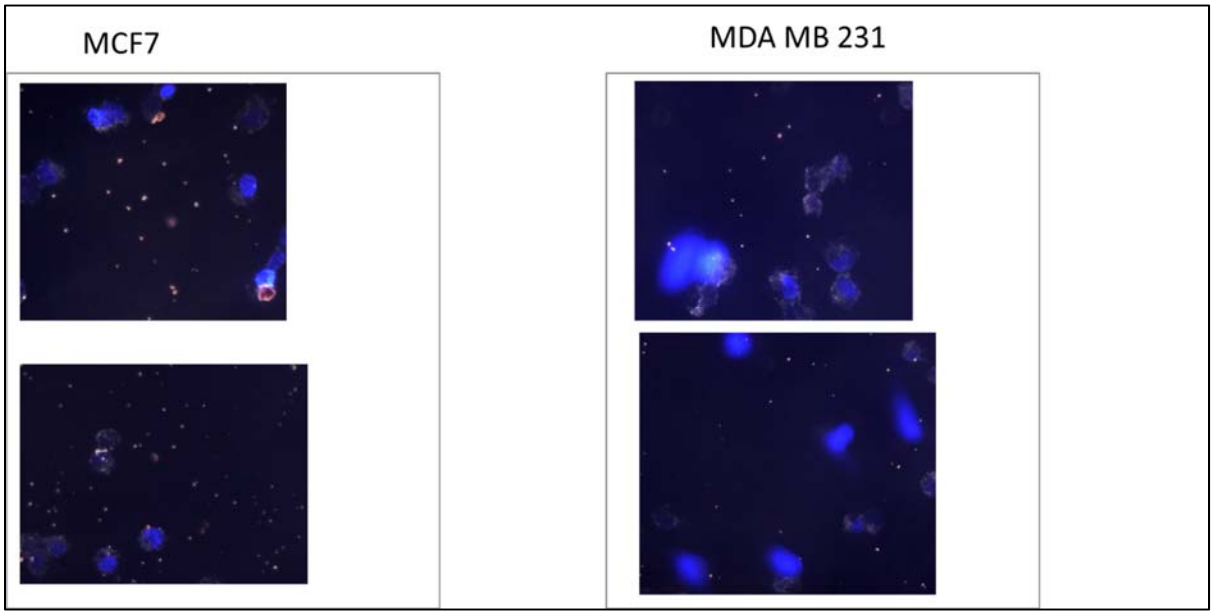

Figure 15 Cellular uptake of AF-MH in MCF7 and MDA MB 231 cell lines

Au@Fe

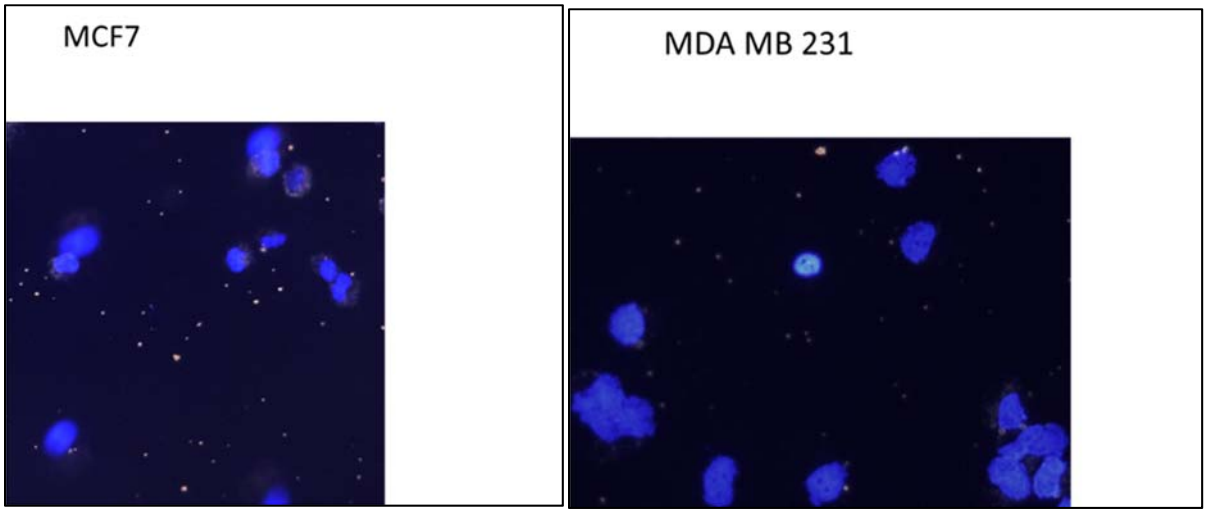

Figure 16 Cellular uptake of AF in MCF7 and MDA MB 231 cell lines

4.3.7 Western Blot

The expression of Jak2 ans Stat5 proteins were analyzed using Western blot. We observed that Jak2 and Stat5 were down regulated in Au@Fe-MFH conjugate. The apoptotic marker proteins Caspase3, Cleaved PARP and Bcl2 were upregulated in the drug treated cells. The results corroborated with the published literature.

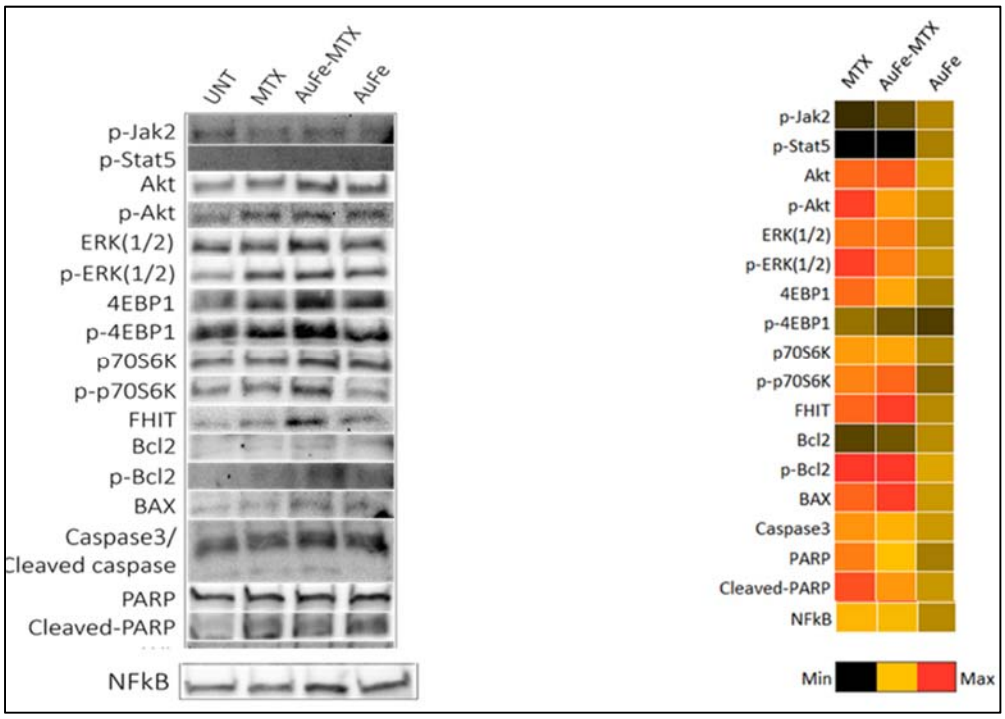

Figure 17 Western Blot images and analysis of protein expression in MDA MB 231 cell lines after MTX, AF-MHF and AF treatment

4.4 Conclusion

We conjugated Methotrexate to HSA and then conjugated it to FA as a targeting moiety. Characterization studies with MTX-HSA-FA (MHF) demonstrated that both FA and MTX were competitively binding to HSA. The MHF conjugated was conjugated to Au@Fe to enable drug delivery into the cells and for imaging. Cell cytotoxicity assays were conducted on MCF7 and

MDA MB 231 cell lines to assess the efficacy of the drug conjugate in comparison with methotrexate. The drug conjugate lowered the IC 50 of the cell lines and cellular uptake studies demonstrated that the target receptor mediated endocytosis took place. Blocking of the FA demonstrated that there was limited uptake with folic acid drug conjugate. Western blot studies were conducted to establish the molecular pathways that are triggered in the cell lines. We observed that the Jak/Stat pathway is downregulated when the cells are treated with drug conjugate. The apoptosis initiation proteins like caspase3, Bcl2 and cleaved PARP were upregulated in the cells. Thus, we demonstrated that MTX-HSA-FA conjugated to Au@Fe is an efficient drug delivery tool for targeting folate receptor expressing breast cancer cells.

Addendum to Chapter 1

Design of Microfluidic chip with small pits

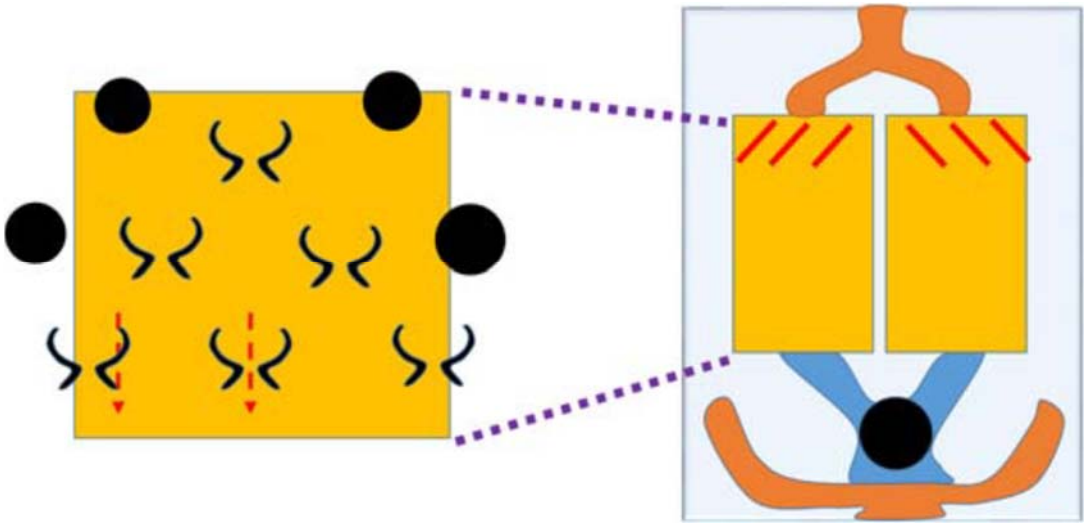

Figure 18 Microfluidic chip design for filtering and capturing small cells based on size

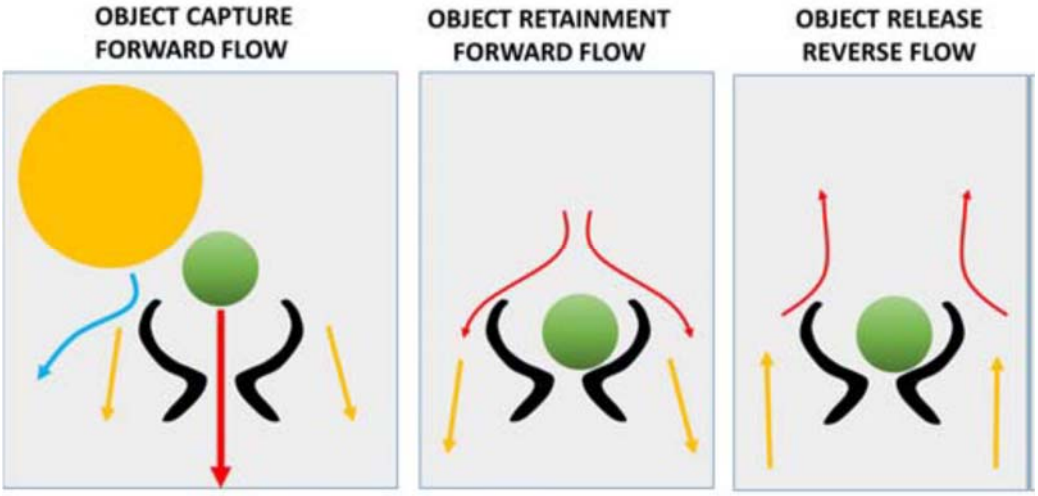

Figure 19 Conceptual microfluidic pit design for capturing small cells and filtering larger particles under aunidirectional flow and reverse flow lift-off

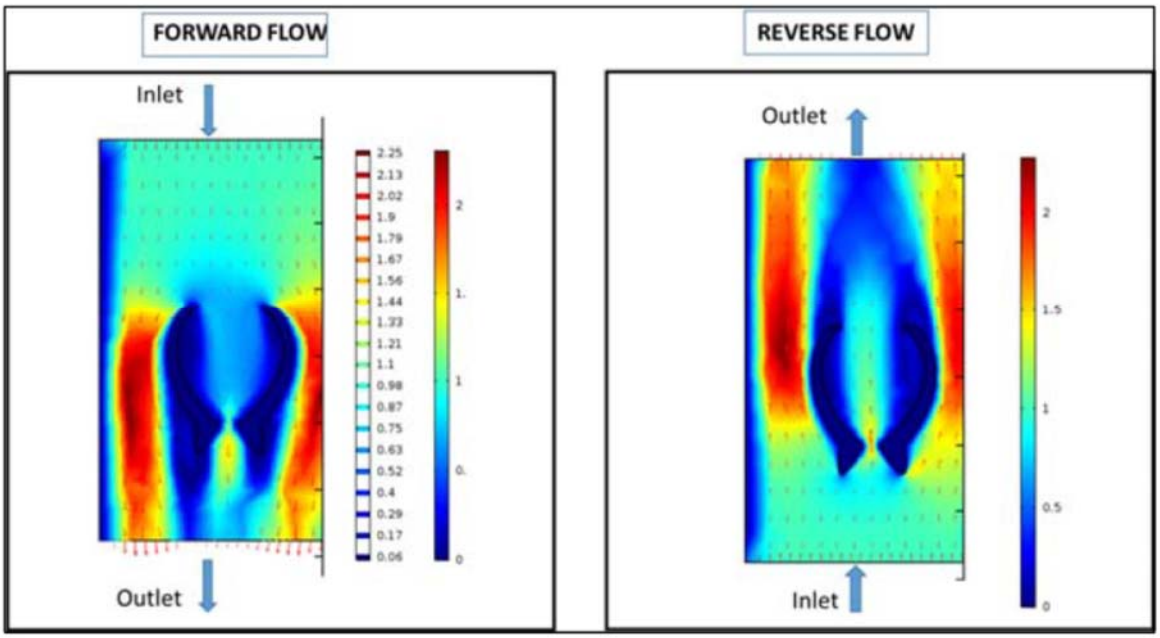

Figure 20 Comsol Simulation of fluid flow along the small pits

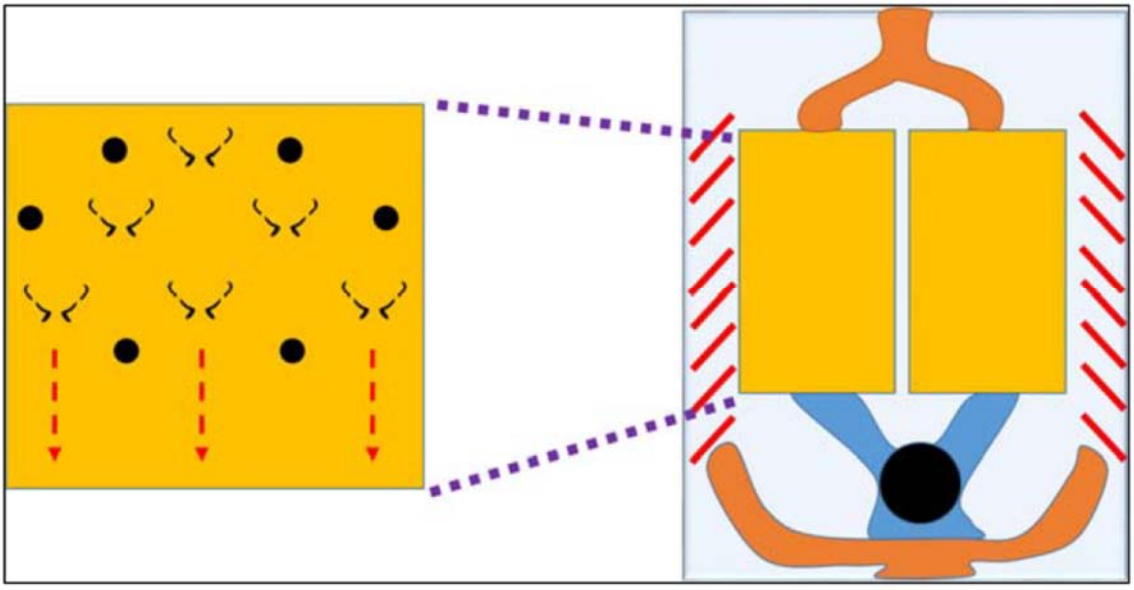

Figure 21 Microfluidic chip design for filtering and capturing larger cells based on size

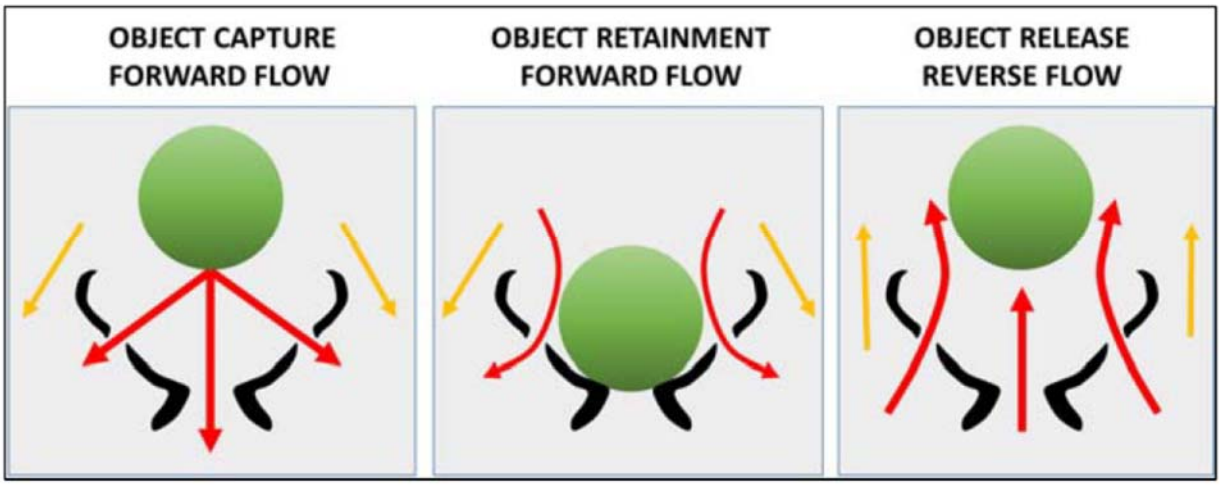

Figure 22 Conceptual microfluidic pit design for capturing large cells and filtering smaller particles under aunidirectional flow and reverse flow lift-off

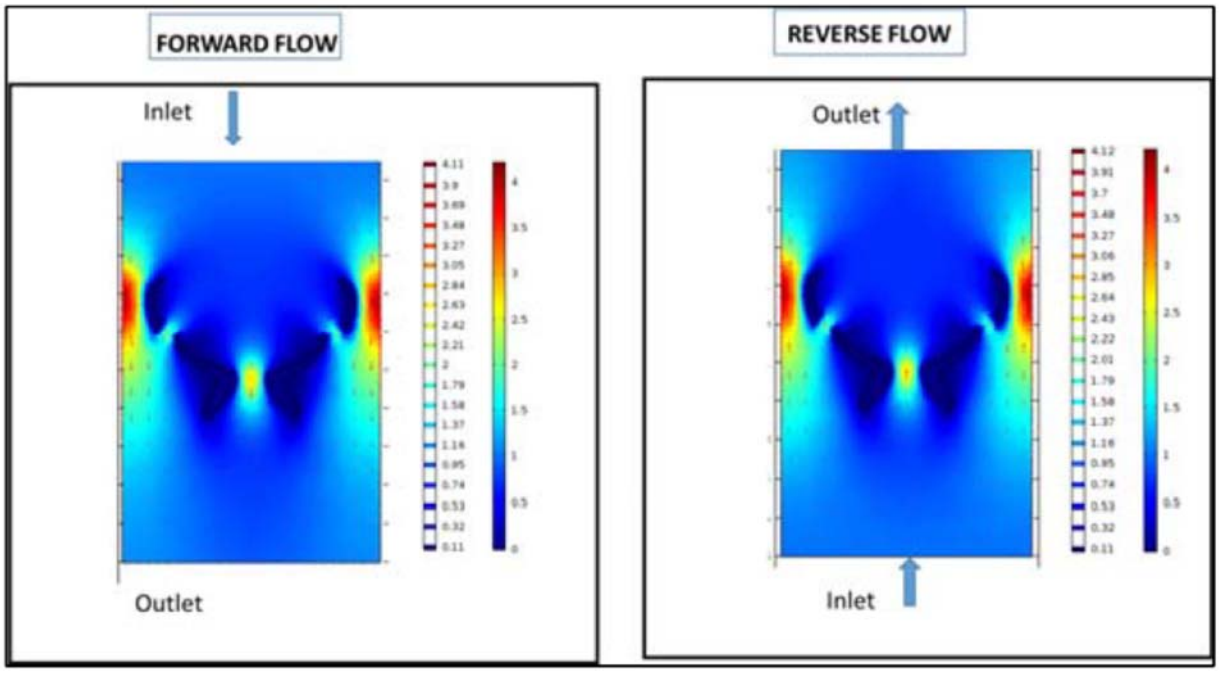

Figure 23 Comsol simulation of fluid flow across a large pit

References

Afrasiabi, Z., Shukla, R., Chanda, N., Bhaskaran, S., Upendran, A., Zambre, A., . . . Kannan, R. (2010). Nanoscale Sensor Design via <I>In Situ</I> Labeling of Gold Nanoparticles onto Protein Scaffolds. *Journal of Nanoscience and Nanotechnology, 10*(2), 719-725. doi:10.1166/jnn.2010.1906

Apps, R., Gardner, L., & Moffett, A. (2008). A critical look at HLA-G. *Trends in Immunology, 29*(7), 313-321. doi:10.1016/j.it.2008.02.012

Asano, M. K., & Dray, P. B. (2014). Retinopathy of prematurity. *Dis Mon, 60*(6), 282-291. doi:10.1016/j.disamonth.2014.03.009

Ates, O., Alp, H. H., Caner, I., Yildirim, A., Tastekin, A., Kocer, I., & Baykal, O. (2009). Oxidative DNA damage in retinopathy of prematurity. *Eur J Ophthalmol, 19*(1), 80-85.

Bolnick, J. M., Kilburn, B. A., Bajpayee, S., Reddy, N., Jeelani, R., Crone, B., . . . Armant, D. R. (2014). Trophoblast retrieval and isolation from the cervix (TRIC) for noninvasive prenatal screening at 5 to 20 weeks of gestation. *Fertility and Sterility, 102*(1), 135-142.e136. doi:10.1016/j.fertnstert.2014.04.008

Chen, J., & Smith, L. E. H. (2007). Retinopathy of prematurity. *Angiogenesis, 10*(2), 133-140. doi:10.1007/s10456-007-9066-0

Chen, J., Stahl, A., Hellstrom, A., & Smith, L. E. (2011). Current update on retinopathy of prematurity: screening and treatment. *Current Opinion in Pediatrics, 23*(2), 173-178. doi:10.1097/MOP.0b013e3283423f35

Chiou, C.-C., Chang, P.-Y., Chan, E.-C., Wu, T.-L., Tsao, K.-C., & Wu, J. T. (2003). Urinary 8-hydroxydeoxyguanosine and its analogs as DNA marker of oxidative stress: development

of an ELISA and measurement in both bladder and prostate cancers. *Clinica Chimica Acta, 334*(1-2), 87-94. doi:10.1016/s0009-8981(03)00191-8

Coester, C. J., Langer, K., van Briesen, H., & Kreuter, J. (2000). Gelatin nanoparticles by two step desolvation--a new preparation method, surface modifications and cell uptake. *J Microencapsul, 17*(2), 187-193. doi:10.1080/026520400288427

Cunha-Vaz, J. G., & World, S. (2011). *Diabetic retinopathy*. Singapore; Hackensack, N.J: World Scientific Pub. Co.

Douglas, G. C., & King, B. F. (1989). Isolation of pure villous cytotrophoblast from term human placenta using immunomagnetic microspheres. *J Immunol Methods, 119*(2), 259-268.

Eshaq, R. S., Aldalati, A. M. Z., Alexander, J. S., & Harris, N. R. (2017). Diabetic retinopathy: Breaking the barrier. *Pathophysiology, 24*(4), 229-241. doi:10.1016/j.pathophys.2017.07.001

Forrester, J. V. (2002). *The eye : basic sciences in practice*. Edinburgh: W.B. Saunders.

Frey, N. A., Peng, S., Cheng, K., & Sun, S. (2009). Magnetic nanoparticles: synthesis, functionalization, and applications in bioimaging and magnetic energy storage. *Chemical Society Reviews, 38*(9), 2532. doi:10.1039/b815548h

Fritz, R., Kohan-Ghadr, H. R., Sacher, A., Bolnick, A. D., Kilburn, B. A., Bolnick, J. M., . . . Armant, D. R. (2015). Trophoblast retrieval and isolation from the cervix (TRIC) is unaffected by early gestational age or maternal obesity. *Prenatal Diagnosis, 35*(12), 1218-1222. doi:10.1002/pd.4681

Georgiou, C. D., & Papapostolou, I. (2006). Assay for the quantification of intact/fragmented genomic DNA. *Analytical Biochemistry, 358*(2), 247-256. doi:10.1016/j.ab.2006.07.035

Heng, Y. J., Liong, S., Permezel, M., Rice, G. E., Di Quinzio, M. K. W., & Georgiou, H. M. (2015). Human cervicovaginal fluid biomarkers to predict term and preterm labor. *Frontiers in Physiology, 6*. doi:10.3389/fphys.2015.00151

Hinokio, Y., Suzuki, S., Hirai, M., Suzuki, C., Suzuki, M., & Toyota, T. (2002). Urinary excretion of 8-oxo-7, 8-dihydro-2'-deoxyguanosine as a predictor of the development of diabetic nephropathy. *Diabetologia, 45*(6), 877-882. doi:10.1007/s00125-002-0831-8

Hui, P. (2012). *Gestational trophoblastic disease : diagnostic and molecular genetic pathology*. New York: Humana Press.

Imudia, A. N., Kumar, S., Diamond, M. P., DeCherney, A. H., & Armant, D. R. (2010). Transcervical retrieval of fetal cells in the practice of modern medicine: a review of the current literature and future direction. *Fertility and Sterility, 93*(6), 1725-1730. doi:10.1016/j.fertnstert.2009.11.022

Imudia, A. N., Suzuki, Y., Kilburn, B. A., Yelian, F. D., Diamond, M. P., Romero, R., & Armant, D. R. (2009). Retrieval of trophoblast cells from the cervical canal for prediction of abnormal pregnancy: a pilot study. *Hum Reprod, 24*(9), 2086-2092. doi:10.1093/humrep/dep206

Jain, C. V., Kadam, L., van Dijk, M., Kohan-Ghadr, H. R., Kilburn, B. A., Hartman, C., . . . Drewlo, S. (2016). Fetal genome profiling at 5 weeks of gestation after noninvasive isolation of trophoblast cells from the endocervical canal. *Science Translational Medicine, 8*(363), 363re364-363re364. doi:10.1126/scitranslmed.aah4661

Ji, L., Brkic, J., Liu, M., Fu, G., Peng, C., & Wang, Y. L. (2013). Placental trophoblast cell differentiation: physiological regulation and pathological relevance to preeclampsia. *Mol Aspects Med, 34*(5), 981-1023. doi:10.1016/j.mam.2012.12.008

Kavanagh, D. M., Kersaudy-Kerhoas, M., Dhariwal, R. S., & Desmulliez, M. P. (2010). Current and emerging techniques of fetal cell separation from maternal blood. *J Chromatogr B Analyt Technol Biomed Life Sci, 878*(22), 1905-1911. doi:10.1016/j.jchromb.2010.05.007

Kowluru, R. A., Kowluru, A., Mishra, M., & Kumar, B. (2015). Oxidative stress and epigenetic modifications in the pathogenesis of diabetic retinopathy. *Prog Retin Eye Res, 48*, 40-61. doi:10.1016/j.preteyeres.2015.05.001

Kowluru, R. A., & Mishra, M. (2015). Oxidative stress, mitochondrial damage and diabetic retinopathy. *Biochimica et Biophysica Acta (BBA) - Molecular Basis of Disease, 1852*(11), 2474-2483. doi:10.1016/j.bbadis.2015.08.001

Lechner, J., O'Leary, O. E., & Stitt, A. W. (2017). The pathology associated with diabetic retinopathy. *Vision Res*. doi:10.1016/j.visres.2017.04.003

Li, L., & Schust, D. J. (2015). Isolation, purification and in vitro differentiation of cytotrophoblast cells from human term placenta. *Reproductive Biology and Endocrinology, 13*(1). doi:10.1186/s12958-015-0070-8

Madsen-Bouterse, S. A., & Kowluru, R. A. (2008). Oxidative stress and diabetic retinopathy: pathophysiological mechanisms and treatment perspectives. *Rev Endocr Metab Disord, 9*(4), 315-327. doi:10.1007/s11154-008-9090-4

Naidu, B. V. K., & Paulson, A. T. (2011). A new method for the preparation of gelatin nanoparticles: Encapsulation and drug release characteristics. *Journal of Applied Polymer Science, 121*(6), 3495-3500. doi:10.1002/app.34171

Nakajima, N., & Ikada, Y. (1995). Mechanism of amide formation by carbodiimide for bioconjugation in aqueous media. *Bioconjug Chem, 6*(1), 123-130.

Nelson, P. N., Reynolds, G. M., Waldron, E. E., Ward, E., Giannopoulos, K., & Murray, P. G. (2000). Monoclonal antibodies. *Mol Pathol, 53*(3), 111-117.

Pankhurst, Q. A., Connolly, J., Jones, S. K., & Dobson, J. (2003). Applications of magnetic nanoparticles in biomedicine. *Journal of Physics D: Applied Physics, 36*(13), R167.

Park, J., An, K., Hwang, Y., Park, J. G., Noh, H. J., Kim, J. Y., . . . Hyeon, T. (2004). Ultra-large-scale syntheses of monodisperse nanocrystals. *Nat Mater, 3*(12), 891-895. doi:10.1038/nmat1251

Pickup, J. C., & Williams, G. (1994). *Chronic complications of diabetes*. Oxford; Boston: Blackwell Scientific Publications.

Red-Horse, K., Zhou, Y., Genbacev, O., Prakobphol, A., Foulk, R., McMaster, M., & Fisher, S. J. (2004). Trophoblast differentiation during embryo implantation and formation of the maternal-fetal interface. *Journal of Clinical Investigation, 114*(6), 744-754. doi:10.1172/jci200422991

Robinson, I., Tung le, D., Maenosono, S., Walti, C., & Thanh, N. T. (2010). Synthesis of core-shell gold coated magnetic nanoparticles and their interaction with thiolated DNA. *Nanoscale, 2*(12), 2624-2630. doi:10.1039/c0nr00621a

Safi, S. Z., Qvist, R., Kumar, S., Batumalaie, K., & Ismail, I. S. (2014). Molecular mechanisms of diabetic retinopathy, general preventive strategies, and novel therapeutic targets. *Biomed Res Int, 2014*, 801269. doi:10.1155/2014/801269

Santella, R. M. (1999). Immunological methods for detection of carcinogen-DNA damage in humans. *Cancer Epidemiol Biomarkers Prev, 8*(9), 733-739.

Shang, L., Dong, S., & Nienhaus, G. U. (2011). Ultra-small fluorescent metal nanoclusters: Synthesis and biological applications. *Nano Today, 6*(4), 401-418. doi:10.1016/j.nantod.2011.06.004

Srikar, R., Suresh, D., Zambre, A., Taylor, K., Chapman, S., Leevy, M., . . . Kannan, R. (2016). Targeted nanoconjugate co-delivering siRNA and tyrosine kinase inhibitor to KRAS mutant NSCLC dissociates GAB1-SHP2 post oncogene knockdown. *Scientific Reports, 6*(1). doi:10.1038/srep30245

Tarrade, A., Lai Kuen, R., Malassine, A., Tricottet, V., Blain, P., Vidaud, M., & Evain-Brion, D. (2001). Characterization of human villous and extravillous trophoblasts isolated from first trimester placenta. *Lab Invest, 81*(9), 1199-1211.

Teng, X., & Yang, H. (2004). Effects of surfactants and synthetic conditions on the sizes and self-assembly of monodisperse iron oxide nanoparticlesElectronic supplementary information (ESI) available: XRD data of iron oxide nanoparticles, Fig. S1 and S2. See http://www.rsc.org/suppdata/jm/b3/b311610g. *Journal of Materials Chemistry, 14*(4), 774. doi:10.1039/b311610g

Wu, L., Pu, W., Liu, Y., Zhao, H., & Shu, W. (2015). Visual detection of 8-OHdG based on the aggregation of gold nanoparticles capped with the anti-8-OHdG antibody. *Analytical Methods, 7*(19), 8360-8365. doi:10.1039/c5ay01774b

Wu, L. L., Chiou, C. C., Chang, P. Y., & Wu, J. T. (2004). Urinary 8-OHdG: a marker of oxidative stress to DNA and a risk factor for cancer, atherosclerosis and diabetics. *Clin Chim Acta, 339*(1-2), 1-9.

Xie, J., Zheng, Y., & Ying, J. Y. (2009). Protein-Directed Synthesis of Highly Fluorescent Gold Nanoclusters. *Journal of the American Chemical Society, 131*(3), 888-889. doi:10.1021/ja806804u

Xu, C., & Sun, S. (2009). Superparamagnetic nanoparticles as targeted probes for diagnostic and therapeutic applications. *Dalton Transactions*(29), 5583. doi:10.1039/b900272n

Zhang, S., Gong, M., Zhang, D., Yang, H., Gao, F., & Zou, L. (2014). Thiol-PEG-carboxyl-stabilized Fe 2 O 3 /Au nanoparticles targeted to CD105: Synthesis, characterization and application in MR imaging of tumor angiogenesis. *European Journal of Radiology, 83*(7), 1190-1198. doi:10.1016/j.ejrad.2014.03.034

Zhen, G., Muir, B. W., Moffat, B. A., Harbour, P., Murray, K. S., Moubaraki, B., . . . Hartley, P. G. (2011). Comparative Study of the Magnetic Behavior of Spherical and Cubic Superparamagnetic Iron Oxide Nanoparticles. *The Journal of Physical Chemistry C, 115*(2), 327-334. doi:10.1021/jp104953z

Zhu, X., Han, T., Yin, G., Wang, X., & Yao, Y. (2011). Expression of Human Leukocyte Antigen-G during Normal Placentation and in Preeclamptic Pregnancies. *Hypertension in Pregnancy, 31*(2), 252-260. doi:10.3109/10641955.2011.638955

Zhu, X., Hondroulis, E., Liu, W., & Li, C.-z. (2013). Biosensing Approaches for Rapid Genotoxicity and Cytotoxicity Assays upon Nanomaterial Exposure. *Small, 9*(9-10), 1821-1830. doi:10.1002/smll.201201593

Zhu, X., Shah, P., Stoff, S., Liu, H., & Li, C. Z. (2014). A paper electrode integrated lateral flow immunosensor for quantitative analysis of oxidative stress induced DNA damage. *Analyst, 139*(11), 2850-2857. doi:10.1039/c4an00313f

Vita

Shreya Ghoshdastidar was born on 15th May, 1988 India to Dr. P S Ghoshdastidar and Ms.Sumita Ghoshdastidar. She comleted her high school in Kanpur, India and received her bachelor's degree from West Bengal University of Technology in Biotechnology in 2009. She proceeded to pursue her graduate studies from University of Missouri, Columbia in The department of Bioengineering. During her term as a graduate student she served as the General Secretary and President of the Graduate Society of Bioengineer and also volunteered in several activities organized by the International Center in University of Missouri. Her PhD thesis was on Clinical Translation of Nanomaterials for Early Detection of Genetic Abnormalities in Fetus and Retinopathy in Neonates and Adults. Her focus was in synthesis of nanomaterials and their application in developing diagnostic assays followed by their validation in clinical samples